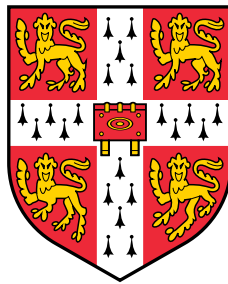# Interacting Fermi Gases

A Thesis in two Parts by

Thomas Michael Whitehead

This dissertation is submitted for the degree of
Doctor of Philosophy

Jesus College   March 2018

Preface

The first Chapter of this Thesis comprises an introduction to the topic of interacting Fermi gases, and in particular their experimental realisation in ultracold atomic gases, and also an overview of the theoretical methods relevant for the rest of the Thesis. The remainder of the Thesis contains original research that has been published, or submitted for peer review, elsewhere, as follows:

Chapter 2: T.M. Whitehead and G.J. Conduit, *Pseudopotentials for an ultracold dipolar gas*, Physical Review A **93**, 022706 (2016).

Chapter 3: T.M. Whitehead, L.M. Schonenberg, N. Kongsuwan, R.J. Needs, and G.J. Conduit, *Pseudopotential for the two-dimensional contact interaction*, Physical Review A **93**, 042702 (2016).

Chapter 4: T.M. Whitehead, M.H. Michael, and G.J. Conduit, *Jastrow correlation factor for periodic systems*, Physical Review B **94**, 035157 (2016).

Chapter 5: T.M. Whitehead and G.J. Conduit, *Multiparticle instability in a spin-imbalanced Fermi gas*, Physical Review B **97**, 014502 (2018).

Chapter 6: T.M. Whitehead and G.J. Conduit, *Multi-particle theory of superconductivity*, in preparation.

This Thesis is the result of my own work and includes nothing which is the outcome of work done in collaboration except as declared in this Preface and specified in the text. In Chapter 3 my contribution to the collaborative work was the physical analysis underlying every Section except Section 3.5, whilst in Chapter 4 my contribution consisted of the full derivation and testing once the underlying idea had been suggested. In all other Chapters I carried out the full scope of work presented, with

the guidance of my supervisor. This Thesis is not substantially the same as any that I have submitted, or is being concurrently submitted for a degree or diploma or other qualification at the University of Cambridge or any other University or similar institution. I further state that no substantial part of this Thesis has already been submitted, or is being concurrently submitted, for any such degree, diploma or other qualification at the University of Cambridge or any other University or similar institution. This Thesis does not exceed 60,000 words.

Acknowledgements

Abstract

Interacting Fermi gases are one of the chief paradigms of condensed matter physics. They have been studied since the beginning of the development of quantum mechanics, but continue to produce surprises today. Recent experimental developments in the field of ultracold atomic gases, as well as conventional solid state materials, have produced new and exotic forms of Fermi gases, the theoretical understanding of which is still in its infancy. This Thesis aims to provide updated tools and additional insights into some of these systems, through the application of both numerical and analytical techniques.

The first Part of this Thesis is concerned with the development of improved numerical tools for the study of interacting Fermi gases. These tools take the form of accurate model potentials for the dipolar and contact interactions, as found in various ultracold atomic gas experiments, and a new form of Jastrow correlation factor that interpolates between the radial symmetry of the inter-electron Coulomb potential at short inter-particle distances, and the symmetry of the numerical simulation cell at large separation. These methods are designed primarily for use in quantum Monte Carlo numerical calculations, and provide high accuracy along with considerable acceleration of simulations.

The second Part shifts focus to an analytical analysis of spin-imbalanced Fermi gases with an attractive contact interaction. The spin-imbalanced Fermi gas is shown to be unstable to the formation of multi-particle instabilities, generalisations of a Cooper pair containing more than two fermions, and then a theory of superconductivity is built from these instabilities. This multi-particle superconductivity is shown to be energetically favourable over conventional superconducting phases in spin-imbalanced Fermi gases, and its unusual experimental consequences are discussed.

Contents

List of Figures

Chapter 1

Introduction

1.1 Condensed matter physics

Condensed matter physics is the study of the universe in microcosm. Through the scrutiny of materials and model systems, both experimentally and theoretically, we gain insights that extend far beyond the laboratory walls.

These investigations teach us about our world, in the most direct (simulations of materials at the centre of the earth [1]) or the most circuitous (study of lattice spin models to describe material phase transitions [2]) ways. They can teach us about the physical laws underpinning our world, from the macroscopic principles of thermodynamics to the counterintuitive results of quantum mechanics.

Condensed matter physics also provides the foundations for much of material science. Almost the entirety of our modern information age is built upon an understanding of, and control over, the physical properties of silicon, which have been achieved through decades of research. Solar cell and battery technology continue to develop thanks to the efforts of armies of researchers, in academia and industry.

But most of all, condensed matter physics is a playground of ideas, a setting for the exploration and advancement of theories and concepts. Many, perhaps, will form but the lowest rungs on a ladder of progress in their field, destined to be forgotten once their limited contribution has been absorbed into the mainstream. Others, though, shine brightly from a distance of half a century or more, ideas that continue to inspire and suggest new avenues of investigation, and will continue to do so for decades to come, motivating future generations of physicists.

The particular ideas outlined in this Thesis build upon a wide variety of previous work in condensed matter physics, experimental and theoretical. This background is briefly discussed in the remainder of this Chapter, covering both the physical and experimental systems that inspired the research in this Thesis, and also the theoretical techniques, analytical and numerical, used to carry it out.

1.2   Interacting Fermi gases

The unifying setting of all the systems examined in this Thesis is a Fermi gas at zero temperature, an idealised expanse populated only by spin-$1/2$ fermions. The distinguishing feature of the systems explored here is the interaction between particles, for interactions create elaborate and exotic phases where otherwise there would be only a featureless degenerate gas. The overarching theme throughout this Thesis is that interactions in Fermi gases drive new physics, which may be analysed and understood through the careful application of theory.

The two Parts of this Thesis have different but complementary aims with regard to this study of the interacting Fermi gas. In Part I, the aim is to take an existing set of numerical methods for studying Fermi gases, and use knowledge about such systems to improve the simulations. In Part II, on the other hand, the aim is to develop an analytical method to study a new type of superconducting phase identified in a well-known type of Fermi gas (a spin-imbalanced Fermi gas). Both Parts are unified in their aims of progressing scientific knowledge about interacting Fermi gases, developing tools and techniques that others can (and have) carry forwards to investigate new systems and carry out new analyses, with a concluding Chapter at the end that ties the themes together.

The subject matter of this Thesis is exclusively theoretical in nature, but the Fermi gases it examines may, of course, be realised experimentally. The remainder of this Section discusses how interacting Fermi gases may be realised, examining the realisations applicable to each Chapter in turn. Section 1.3 then reviews the simplifications and approximations needed to model these Fermi gases theoretically, split into two broad themes corresponding to the Parts of this Thesis.

1.2.1   Part I

The interacting Fermi gases explored in Chapters 2 and 3 are not systems that would exist naturally, without the help of experimentalists. They are two-dimensional systems, where almost all naturally-occurring Fermi gases are three-dimensional, and include dipolar and contact interactions respectively, which are rare in nature. However, this does not mean that these systems are pure inventions of a theorist's mind.

Fermi gases like those examined in Chapters 2 and 3 do exist, and do satisfy practical needs. By constructing simplified and pure fermionic systems, experimentalists are able to reduce the influence of effects they are not interested in, and focus on the important properties they are concerned with, whether properties of particles themselves or the phases they form under the action of inter-particle and external potentials.

In Chapter 2, the abstracted Fermi gas considered is a two-dimensional system, with fermions interacting via a dipolar potential. This is a model of real experimental setups, where the fermionic particles are either atoms with large magnetic dipole moments [3–5] or molecules with large electric dipole moments [6–12]. These atoms, cooled down to quantum degeneracy, are held in a 'pancake' trap, which mimics a two-dimensional geometry [13]. More details on how these atoms and molecules are cooled, trapped, and manipulated are given in Section 1.2.3 below, but here the focus is on the rationale behind the creation of such systems.

These atomic and molecular systems are perfect examples of the use of condensed matter physics to study the universe in microcosm. The high degree of control these systems allow experimentalists makes them an ideal testbed for ideas in quantum information processing, with the end-goal of creating a workable quantum computer [14–16]. The strong repulsive dipolar interaction in two dimensions can also allow fine control over chemical reactions between the constituent particles [17], giving more insight into the underlying chemical and physical processes. More conceptually, the ultracold atomic and molecular systems may be used as quantum simulators [18], tools to model the novel phases and dynamics found in other quantum systems.

The Fermi gas examined in Chapter 3 is similar to that in Chapter 2, the only difference being the interaction between the fermions: a contact interaction instead

of a dipolar interaction. The contact interaction is, in some sense, the 'natural' interaction to consider for ultracold atomic gas systems: the fundamental method used to tune interactions between neutral atoms is known as the Feshbach resonance [19] (described in Section 1.2.3), which has many of the properties of a contact interaction, and is typically modelled as such [20–28].

The similarity between the physical, experimental systems examined in Chapters 2 and 3 means that they have many of the same uses. It also means that many of the theoretical tools used to model them are transferable. The focus of Chapters 2 and 3 is on accelerating those theoretical tools, which are described in Section 1.3.1. One of the chief constraints on modelling the interacting Fermi gases numerically is the behaviour of the inter-particle potential: both the dipolar and contact interactions diverge at particle coalescence, causing sampling problems. Chapters 2 and 3 therefore focus on remedying this problem, by noting that all the macroscopic physics of the systems depends on the scattering properties of the inter-particle potentials, and so the divergent physical potentials may be replaced by more numerically tractable 'pseudopotentials', providing the pseudopotential exhibits accurate enough scattering properties. Pseudopotentials are developed in Chapters 2 and 3 for the dipolar and contact interactions respectively.

Unlike the systems examined in Chapters 2 and 3, which are constructed by experimentalists to answer particular questions, the interacting Fermi gases (namely electron gases) that are relevant for Chapter 4 exist naturally, and take the form of common metals. Many properties of metals are easy to measure, which allows accurate comparisons between experiment and theory, and therefore necessitates very precise theoretical methods. An issue with many of the numerical methods commonly used to study strongly correlated electron gases and metals is that the correlations between electrons that are captured by the method are constrained by artificial symmetries imposed during the simulations. To make infinite Fermi gases amenable to numerical simulation they are usually split into finite simulation cells, which are tessellated, with periodic boundary conditions, to fill all of space. However, these simulation cells bring with them symmetries in the choice of cell used. The typical correlation functions used in simulations either encode this simulation cell symmetry, or the radial symmetry of the Coulomb interaction between electrons, but not both. This leads to inefficiencies in the construction of correlation functions, which is addressed in Chapter 4 through the creation of a correlation function that

interpolates between the simulation cell symmetry and the radial symmetry of the Coulomb interaction as a function of distance from an electron. One particular numerical method that benefits from the developments in Chapter 4 is described in Section 1.3.1 below.

1.2.2   Part II

The experimental realisation of the systems examined in Part II of this Thesis span both the ultracold atomic gas experiments relevant to Chapters 2 and 3, and the electronic systems relevant to Chapter 4. Part II is concerned with the ground state of a particular type of interacting Fermi gas, one with a spin-imbalance. Spin-$1/2$ fermions have two natural states, colloquially called spin-up ($\uparrow$) and spin-down ($\downarrow$). In almost all natural materials in the absence of a magnetic field, the spin-up and spin-down species are present in equal numbers, but this balance may be broken, either by the application of a magnetic field to electrons, or through a more exotic mechanism like spin-orbit coupling [29,30]. Ultracold atomic gas systems may also be used as quantum simulators to mimic this behaviour by using two different species with different pseudospins, with different numbers of fermions of the different species included in the experiment.

Chapter 5 is concerned with a few-particle limit of this spin-imbalanced Fermi gas, identifying an instability against the formation of multi-particle correlated states. The interaction between fermions that drives this instability is a contact interaction, similar to that discussed above, and in ultracold atomic gases could be realised in exactly the same way. In electron-based systems, the contact interaction is a useful approximation, as the real physical interactions between electrons (repulsive Coulomb interaction and attractive phonon-mediated interaction) are too complex to capture in a theory of the kind developed in this Thesis.

Chapter 6 extends the instability theory of Chapter 5 to a full many-body theory of superconductivity in spin-imbalanced Fermi gases, comparing the novel state formed from multi-particle instabilities favourably with the conventional theory of superconductivity in these systems. Background to the framework used to construct this theory of superconductivity is given below in Section 1.3.2.

As ultracold atomic gases may be used as quantum simulators for all the systems discussed in this Thesis, and, in the case of Chapters 2 and 3, are the main

experimental motivation, the following Subsection comprises a short introduction to the cooling, trapping, and manipulation of ultracold atoms.

1.2.3 Ultracold atomic gases

A defining feature of fermionic ultracold atomic gases is that their constituent particles are at such low temperatures that the effects of quantum degeneracy cannot be ignored. Cooling to this temperature is typically achieved by a combination of laser cooling, where a slightly red-detuned laser beam excites a moving atom, which then loses slightly more energy when it relaxes again [31], and evaporative cooling, where elastic collisions of particles rethermalise the gas after selective removal of the most energetic particles [32] (typically involving another 'sympathetic' atomic species or spin species, to circumvent the problem of identical fermions having no s-wave scattering cross-section [33]).

Once the fermions are cooled to quantum degeneracy, they need to be held in space in order to carry out experiments. In the experiments relevant for this Thesis, this is typically achieved by the use of an optical trap. Optical trapping involves the use of the dipole force that atoms experience in off-resonant light [34], attracting the atoms to the nodes (antinodes) of blue- (red-)detuned laser light. A spatially-varying laser-intensity field therefore creates a trapping potential.

Once trapped, experiments can then probe the properties of the quantum degenerate gas: the density profile can be found by a real-space imaging of the trap; the momentum distribution determined by a time-of-flight measurement [35]; and excitations and impurities identified by radio frequency spectroscopy [36], for example.

To observe the physics of interest in a trapped ultracold atomic gas, a method of accurately controlling inter-particle interactions is required. The chief tool used is the Feshbach resonance [19], which is very briefly discussed here.

Feshbach resonance

A Feshbach resonance is a particular resonant interaction between two particles in an ultracold atomic gas. A Feshbach resonance couples the open, scattering channel of two particles with a closed channel containing a bound state [19]. This is illustrated in Fig. 1.1, where one ultracold particle (with approximately zero energy) approaches another from large separation. If the closed channel of the two

Figure 1.1: Simplified model of a Feshbach resonance coupling an open, scattering channel (blue) with a closed channel (red). The closed channel contains a bound state with energy E_b. Resonant coupling occurs when E_b is tuned near to 0.
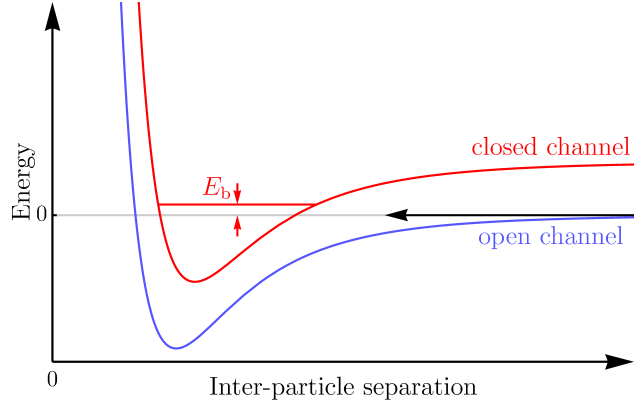
particles has a different magnetic moment to the open channel, the energies of the two channels may be moved relative to each other by the application of an external magnetic field. In particular, the bound state energy E_b of the closed channel may be tuned close to 0, which even for weak inter-channel coupling can lead to a strong resonance. This leads to very fine control over inter-particle interactions, with the scattering properties of two particles depending strongly on the applied magnetic field.

1.3   Theoretical tools

Although the interacting Fermi gases examined in this Thesis may be constructed and studied experimentally, the approach taken here is purely theoretical. Both analytical and numerical methods are employed to gain insight into the systems of interest, and to identify and develop improvements to the methods themselves. This Section discusses two of the main techniques used in this Thesis: in Section 1.3.1, the numerical technique of quantum Monte Carlo calculation that forms the backdrop of Part I, and in Section 1.3.2 the analytical theory of superconductivity that is extended in Chapter 6.

1.3.1   Quantum Monte Carlo

The interacting Fermi gases at zero temperature in this Thesis are, by their very nature, strongly-correlated quantum systems. The strong correlations mean that perturbative analyses are doomed to be insufficient, and so when exact solutions are

intractable (as is the case in Part I) numerical approaches are required. However, the probabilistic nature of quantum mechanics means that the number of possible states a computer needs to consider (the size of the Hilbert space) grows exponentially with the system size [18], ruling out direct methods like exact diagonalisation of the system Hamiltonian in all except the simplest cases.

A common method used to bypass this problem of exponentially large configuration spaces is to turn to probabilistic methods in the numerical approach itself. A leading example of this school of thought is the class of methods known as quantum Monte Carlo [37], which are variational methods for evaluating quantum mechanical expectation values in a way that scales only polynomially with the system size. The particular quantum Monte Carlo techniques used in this Thesis are the variational Monte Carlo (VMC) and diffusion Monte Carlo (DMC) methods.

Variational Monte Carlo is a conceptually simple method: the energy of a Hamiltonian $\hat{H}$ with a trial wavefunction $\Psi_{\mathrm{T}}(\mathbf{R})$, a function of the vector $\mathbf{R}$ of particle coordinates, can be expressed as

$$E_{\mathrm{V}} = \frac{\int \Psi_{\mathrm{T}}^{\dagger}(\mathbf{R})\hat{H}\Psi_{\mathrm{T}}(\mathbf{R})\mathrm{d}\mathbf{R}}{\int |\Psi_{\mathrm{T}}(\mathbf{R})|^2 \, \mathrm{d}\mathbf{R}}, \tag{1.1}$$

which is an upper bound on the ground state energy $E_0 < E_{\mathrm{V}}$ of $\hat{H}$, with equality only when $\Psi_{\mathrm{T}}(\mathbf{R})$ is the ground eigenstate of $\hat{H}$. Minimising the energy E_{V} with respect to the trial wavefunction $\Psi_{\mathrm{T}}(\mathbf{R})$ therefore provides an accurate approximation to the ground state energy, if the trial wavefunction $\Psi_{\mathrm{T}}(\mathbf{R})$ can be varied to approximate the ground state wavefunction.

However, Eq. (1.1) is a challenging integral to evaluate, being very high-dimensional in many-particle systems. The most efficient way to evaluate such an integral is by using a Monte Carlo method to randomly sample configuration space and find an approximation to the true integral value. Using M random samples leads to an uncertainty in the estimate which scales as $1/\sqrt{M}$, independently of the size of the configuration space [37]. It is convenient to express Eq. (1.1) as a weighted average over all configuration space of the local energy $E_{\mathrm{L}}(\mathbf{R}) = \Psi_{\mathrm{T}}^{-1}(\mathbf{R})\hat{H}\Psi_{\mathrm{T}}(\mathbf{R})$,

$$E_{\mathrm{V}} = \frac{\int |\Psi_{\mathrm{T}}(\mathbf{R})|^2 \, \Psi_{\mathrm{T}}^{-1}(\mathbf{R})\hat{H}\Psi_{\mathrm{T}}(\mathbf{R})\mathrm{d}\mathbf{R}}{\int |\Psi_{\mathrm{T}}(\mathbf{R})|^2 \, \mathrm{d}\mathbf{R}} = \frac{\int |\Psi_{\mathrm{T}}(\mathbf{R})|^2 \, E_{\mathrm{L}}(\mathbf{R})\mathrm{d}\mathbf{R}}{\int |\Psi_{\mathrm{T}}(\mathbf{R})|^2 \, \mathrm{d}\mathbf{R}}.$$

The last expression in this equation can be sampled efficiently using the Metropolis algorithm [38] and the variational energy then estimated using these M configurations $\mathbf{R}_i$ as

$$E_\text{V} \approx \frac{1}{M} \sum_{i=1}^{M} E_\text{L}(\mathbf{R}_i).$$

The proximity of the estimated energy E_V to the ground state energy E_0 depends on the choice $\Psi_\text{T}(\mathbf{R})$. A good choice will closely approximate the real ground state wavefunction: if $\Psi_\text{T}(\mathbf{R})$ were to be the exact ground state wavefunction then $E_\text{L}(\mathbf{R})$ would be a constant E_0 and every sample the Metropolis algorithm made would give this same energy, resulting in zero uncertainty in the estimate. However, a poor choice will lead to the Metropolis algorithm sampling unimportant areas of configuration space, predicting erroneously large kinetic energies, or otherwise over-estimating the ground state energy. Furthermore, an inaccurate trial wavefunction will give different local energies at different points of configuration space, and hence a significant uncertainty in the estimated energy.

In order to obtain accurate VMC results, the trial wavefunction $\Psi_\text{T}(\mathbf{R})$ is usually taken to depend on several variational parameters α_i. The trial wavefunction typically takes the form [39]

$$\Psi_\text{T}(\mathbf{R}) = \text{e}^{J(\mathbf{R},\alpha_1,\alpha_2,\dots)} D(\mathbf{R}),$$

where $D(\mathbf{R})$ is a Slater determinant of single-particle orbitals, capturing fermionic antisymmetry, and the Jastrow correlation factor $\text{e}^{J(\mathbf{R},\alpha_1,\alpha_2,\dots)}$ encodes inter-particle correlation. As long as $J(\mathbf{R},\alpha_1,\alpha_2,\dots)$ is a symmetric function of the particle positions, the Jastrow factor does not modify the fermionic antisymmetry of the Slater determinant. The wavefunction $\Psi_\text{T}(\mathbf{R})$, and hence the local energy, is optimised by minimising either the energy E_V or a related function with respect to the α_i. This then gives an approximation for both the wavefunction and the ground state energy.

The accuracy of the VMC estimate for the ground state energy is limited by the accuracy of the VMC trial wavefunction. Chapter 4 discusses a method for creating flexible and accurate Jastrow factors to ameliorate this problem, and in addition simplify the optimisation of the energy E_V.

The accuracy constraints of VMC are mostly averted by another quantum Monte

Carlo method, diffusion Monte Carlo (DMC). Instead of direct estimates of the energy expectation value using a trial wavefunction, DMC maps the Schrödinger equation onto a diffusion equation for so-called 'walkers', each of which is associated with a particular configuration of particles. The positions of these walkers in configuration space evolve following the diffusion equation, whose Green's function may, for small steps in imaginary time, be factorised into diffusion and branching parts [40].

The diffusion part simply encodes the random walk carried out by walkers under the free, non-interacting diffusion equation. The branching part, on the other hand, weights configuration space according to the potentials acting on the particles: in regions of low potential, an initial walker may be duplicated, giving more weight to the areas of configuration space of low potential, whilst in regions of high potential walkers may die out. This procedure will, after many timesteps, distribute the walkers according to the potential landscape they live in. The energy of the Hamiltonian may then be evaluated at each of the points in configuration space that the walkers represent, providing an estimate of the ground state energy.

This procedure is formally equivalent to using the full interacting Green's function to project out the ground state component of a starting estimate trial wavefunction. This trial wavefunction is typically chosen to be the optimised VMC wavefunction, and provided this wavefunction has some overlap with the true ground state wavefunction, DMC will in principle recover the exact ground state energy. In practice, fermion statistics complicate the DMC algorithm, as a multi-fermion wavefunction necessarily includes regions where the wavefunction changes sign. Although it is possible to assign signs to the DMC walkers, the signal-to-noise ratio decays exponentially [37], a consequence of the ubiquitous fermion sign problem. An inexact, but frequently used and in practice accurate, solution is the fixed-node DMC algorithm, where the nodes of the trial wavefunction are kept constant throughout the random walk through configuration space, with walkers prohibited from crossing the nodes. The fixed-node approximation means that DMC systematically overestimates the ground state energy, and this will typically be the largest source of error in DMC simulations, including those with pseudopotentials.

As well as setting the nodes of the wavefunction obtained from DMC, the trial wavefunction is also used as a guiding wavefunction in more efficient implementations of the DMC algorithm [41], and so contributes to the overall accuracy and efficiency

of the DMC calculation. It is therefore important to have access to accurate and efficient VMC wavefunctions. This is directly addressed in Chapter 4, where a new form for the trial wavefunction is proposed, but is also an extra benefit of the pseudopotential formalism developed in Chapters 2 and 3. Smooth and non-divergent inter-particle potentials allow the variational freedom of the VMC wavefunction to be focussed on correlation effects, rather than having to concentrate on capturing the correct divergent form for the wavefunction at particle coalescence.

1.3.2 BCS theory

Chapter 6 of this Thesis focusses on extending the canonical theory of superconductivity in spin-balanced Fermi gases to the spin-imbalanced case. This chief theory of superconductivity bears the name of its creators, Bardeen, Cooper, and Schrieffer (BCS) [42, 43], and since its inception has explained myriad features of the phenomenon of superconductivity. Part II of this Thesis extends BCS theory by generalising the instability underlying its superconducting behaviour. This Section serves as an introduction to Chapter 6 in particular, by introducing the analytical formalism of BCS theory. This is not the methodology used in the original exposition of BCS theory, but rather a form of quantum field theory that allows the identification of physically important properties of the superconducting state, without complication by extraneous details.

The fundamental object in this quantum field theory is the quantum partition function, a mathematical expression that encodes details about the system of interest by summing over all possible configurations of fermion fields, weighted by a measure of their 'likelihood' of occurring. The sum is represented by a 'path integral' $\int \mathcal{D}\psi$ over fields ψ, and the weighting is by $\exp(-S[\psi])$, where $S[\psi]$ is the action, as familiar from classical statistical mechanics. Here, and throughout this Thesis, natural units are employed, where $\hbar = 1$. Bringing these components together, the quantum partition function for a fermion field with two degrees of freedom ψ and $\bar{\psi}$, comparable roughly to the annihilation and creation operators of second-quantised quantum mechanics, is given by $\mathcal{Z} = \int \mathcal{D}(\psi, \bar{\psi}) \exp(-S[\psi, \bar{\psi}])$.

The particular action relevant for BCS theory takes the simple form

$$S[\psi, \bar{\psi}] = \sum_{\mathbf{k}, \sigma} \bar{\psi}_{\mathbf{k}, \sigma} (-i\omega + \xi_{\mathbf{k}, \sigma}) \psi_{\mathbf{k}, \sigma} - g \sum_{\mathbf{k}, \mathbf{k}', \mathbf{q}} \bar{\psi}_{\mathbf{k}, \uparrow} \bar{\psi}_{\mathbf{q}-\mathbf{k}, \downarrow} \psi_{\mathbf{k}', \downarrow} \psi_{\mathbf{q}-\mathbf{k}', \uparrow}, \qquad (1.2)$$

where the first term is a kinetic part, with dispersion $\xi_{\mathbf{k}, \sigma}$ depending on both the spatial part of the fermion momentum $\mathbf{k}$ and spin species $\sigma \in \{\uparrow, \downarrow\}$, and the second term is the interaction term between fermions, with a contact interaction (as also used in Chapters 3 and 5) of attractive strength $g > 0$. The Matsubara frequencies $\omega = \mathbf{k}^0$, the temporal part of the momenta $\mathbf{k}$ in a Euclidean spacetime, encode the temperature of the system. The momenta $\mathbf{q}$ allow interactions between fermions with momenta that are not opposites: this is relevant in spin-imbalanced systems, as considered in Chapter 6, but neglected in BCS theory, as discussed here, and so subsequently $\mathbf{q}$ shall be set to zero.

The action in Eq. (1.2) is difficult to handle, because it is quartic in the fields ψ and $\bar{\psi}$: actions quadratic in the fields allow their quantum partition functions to be evaluated exactly, through Gaussian integration, but quartic actions are not generally amenable to exact solutions. A method to circumvent this problem is the Hubbard-Stratonovich transformation [44, 45], an exact remapping using the quantum field theory version of the simple integral

$$e^{x^2} = \frac{1}{\sqrt{\pi}} \int_{\infty}^{\infty} dy \, e^{-2xy - y^2},$$

which gives the quantum partition function, involving a new complex (bosonic) field Δ that will go on to have a fundamental interpretation as the energy gap of the system, as $\mathcal{Z} = \int \mathcal{D}(\psi, \bar{\psi}) \mathcal{D}(\Delta, \Delta^*) \exp(-S[\psi, \bar{\psi}, \Delta, \Delta^*])$, where

$$S[\psi, \bar{\psi}, \Delta, \Delta^*] = \sum_{\omega, \mathbf{k}, \sigma} \bar{\psi}_{\mathbf{k}, \sigma} (-i\omega + \xi_{\mathbf{k}, \sigma}) \psi_{\mathbf{k}, \sigma} - \sum_{\omega, \mathbf{k}} \left(\Delta \bar{\psi}_{\mathbf{k}, \uparrow} \bar{\psi}_{-\mathbf{k}, \downarrow} + \Delta^* \psi_{-\mathbf{k}, \downarrow} \psi_{\mathbf{k}, \uparrow} \right)$$
$$+ \sum_{\omega} \frac{|\Delta|^2}{g},$$

and the momenta $\mathbf{k}$ are now taken to just include the spatial degrees of freedom, with the temporal component extracted in the form of ω. This action may be written

using a matrix formalism in terms of $\mathcal{G}_{\mathbf{k},\uparrow}^{-1} = -i\omega + \xi_{\mathbf{k},\uparrow}$ and $\mathcal{G}_{-\mathbf{k},\downarrow}^{-1} = -i\omega - \xi_{-\mathbf{k},\downarrow}$ as

$$S[\psi, \bar{\psi}, \Delta, \Delta^*] = \sum_{\omega,\mathbf{k}} \begin{pmatrix} \bar{\psi}_{\mathbf{k},\uparrow} \\ \psi_{-\mathbf{k},\downarrow} \end{pmatrix}^{\mathrm{T}} \begin{pmatrix} \mathcal{G}_{\mathbf{k},\uparrow}^{-1} & -\Delta \\ -\Delta^* & \mathcal{G}_{-\mathbf{k},\downarrow}^{-1} \end{pmatrix} \begin{pmatrix} \psi_{\mathbf{k},\uparrow} \\ \bar{\psi}_{-\mathbf{k},\downarrow} \end{pmatrix} + \sum_{\omega} \frac{|\Delta|^2}{g},$$

which makes the quadratic form in fermion fields of the transformed action explicit. The 2×2 nature of the matrix in this expression, coupling one down-spin fermion with one up-spin fermion, indicates that the structure underlying BCS superconductivity is the pairing of fermions. These pairs are known as Cooper pairs, fermions that are coupled to each other and no other fermions, with the pairs then correlating to form a superconductor. The chief result of Chapter 6 is that Cooper pairs may be generalised to include fermions which couple with more than one other fermion.

Although the transformations thus far were exact, further progress requires approximation. One typical approximation is the saddle-point approximation, where the path integral over the values of the field Δ is replaced by just the extremal value of Δ in the action, with this value to be determined self-consistently later. The Gaussian integral over the ψ fields may then be carried out analytically, giving the quantum partition function as

$$\mathcal{Z} = \exp\left[-\sum_{\omega,\mathbf{k}} \ln \det \begin{pmatrix} \mathcal{G}_{\mathbf{k},\uparrow}^{-1} & -\Delta \\ -\Delta^* & \mathcal{G}_{-\mathbf{k},\downarrow}^{-1} \end{pmatrix} - \sum_{\omega} \frac{|\Delta|^2}{g} \right],$$

and so, for a zero-frequency field Δ, the thermodynamic potential $\Omega = -T \ln \mathcal{Z}$ at temperature T takes the form

$$\Omega = T \sum_{\omega,\mathbf{k}} \ln \det \begin{pmatrix} \mathcal{G}_{\mathbf{k},\uparrow}^{-1} & -\Delta \\ -\Delta^* & \mathcal{G}_{-\mathbf{k},\downarrow}^{-1} \end{pmatrix} + \frac{|\Delta|^2}{g}. \tag{1.3}$$

It is easy to then carry out the sum over the Matsubara frequencies, and the ther-

modynamic potential, including regularisation, takes the form

$$
\Omega = \sum_{\mathbf{k}} \left(|\xi_{\mathbf{k},+} + \xi_{\mathbf{k},-}| - \sqrt{\xi_{\mathbf{k},+}^2 + |\Delta|^2} - \sum_{\varsigma \in \{+,-\}} T \ln \left[1 + \mathrm{e}^{-\frac{1}{T}\left(\sqrt{\xi_{\mathbf{k},+}^2 + |\Delta|^2} + \varsigma \xi_{\mathbf{k},-} \right)} \right] \right)
$$
$$
+ \frac{|\Delta|^2}{g},
$$

where $\xi_{\mathbf{k},\pm} = \frac{1}{2}(\xi_{\mathbf{k},\uparrow} \pm \xi_{-\mathbf{k},\downarrow})$. For a system of fermions of unit mass with a free dispersion, $\xi_{\mathbf{k},\sigma} = \frac{1}{2}|\mathbf{k}|^2 - \mu_\sigma$, where μ_σ is the chemical potential for species σ, $\xi_{\mathbf{k},+} = \frac{1}{2}|\mathbf{k}|^2 - \bar{\mu}$, where $\bar{\mu} = \frac{1}{2}(\mu_\uparrow + \mu_\downarrow)$, and $\xi_{\mathbf{k},-} = -\delta\mu$, where $\delta\mu = \frac{1}{2}(\mu_\uparrow - \mu_\downarrow)$. In this expression, the functional form $E_{\mathbf{k}} = \sqrt{\xi_{\mathbf{k},+}^2 + |\Delta|^2}$ of the modified dispersion lends meaning to the parameter $|\Delta|$, as the gap in the dispersion: $E_{\mathbf{k}}$ does not go smoothly to zero, but takes a minimum value of $|\Delta|$.

It is easiest to evaluate the sums over momentum $\mathbf{k}$ by going to the infinite system size limit, where the sums become integrals, and then changing variables from $|\mathbf{k}|$ to $\xi_{\mathbf{k},+}$. At zero temperature the thermodynamic potential evaluates to

$$
\Omega/\mathcal{N} = \omega_{\mathrm{D}}\left(\omega_{\mathrm{D}} - \sqrt{\omega_{\mathrm{D}}^2 + |\Delta|^2} \right) - |\Delta|^2 \mathrm{arcsinh}\frac{\omega_{\mathrm{D}}}{|\Delta|}
$$
$$
+ \delta\mu \left(\delta\mu - \sqrt{\delta\mu^2 - |\Delta|^2} \right) + |\Delta|^2 \mathrm{arccosh}\frac{\delta\mu}{|\Delta|} + \frac{|\Delta|^2}{g\mathcal{N}}, \qquad (1.4)
$$

where ω_{D} is the Debye frequency, an ultraviolet cut-off on the energy range of the interaction between fermions, $\mathcal{N}$ is the density of states in energy, and the expression is valid in the weak-coupling and weak spin-imbalance limit where $\omega_{\mathrm{D}} > \delta\mu > |\Delta| > 0$.

Although a closed, analytical form for the thermodynamic potential is obtainable in BCS theory, this is not possible for the spin-imbalanced superconductivity examined in Chapter 6. Instead, the evaluation of the thermodynamic potential itself must also be approximate, typically by expanding the thermodynamic potential in powers of $|\Delta|^2$. This procedure is also possible for BCS theory itself: the defining expression for the thermodynamic potential Eq. (1.3) may be written as

$$
\Omega = \alpha|\Delta|^2 + \frac{1}{2}\beta|\Delta|^4 + \dots,
$$

Figure 1.2: The BCS thermodynamic potential Ω evaluated both exactly (blue curve), using Eq. (1.4), and following the expansion method of Eq. (1.5) (red curve), indicating the accuracy of the expansion method at small $|\Delta|^2$.
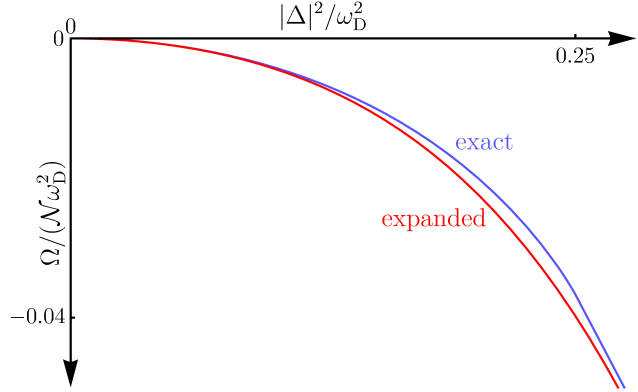
where

$$\alpha = \frac{1}{g} + T\sum_{\omega,\mathbf{k}} \mathcal{G}_{\mathbf{k},\uparrow}\mathcal{G}_{-\mathbf{k},\downarrow},$$

$$\beta = T\sum_{\omega,\mathbf{k}} \mathcal{G}^2_{\mathbf{k},\uparrow}\mathcal{G}^2_{-\mathbf{k},\downarrow},$$

etc. At zero temperature the expansion coefficients α and β may be evaluated similarly to the full expression for the thermodynamic potential above, giving

$$\Omega/\mathcal{N} = \left(\frac{1}{g\mathcal{N}} - \ln\frac{\omega_{\mathrm{D}}}{\delta\mu}\right)|\Delta|^2 - \frac{|\Delta|^4}{8\delta\mu^2} + \ldots, \tag{1.5}$$

the simplicity of whose terms may be contrasted with the equivalent terms in Chapter 6. Eq. (1.5) can also be obtained as a Taylor series of Eq. (1.4) around $|\Delta|^2 = 0$, confirming the self-consistency of this approximate method for evaluating the thermodynamic potential. The thermodynamic potentials from Eqs. (1.4) and (1.5) are compared in Fig. 1.2, again indicating that the expansion method provides an accurate approximation to the full thermodynamic potential at small $|\Delta|$ for BCS theory, which helps justify its use in the investigation of spin-imbalanced superconductivity in Chapter 6. In both curves the chemical potential difference $\delta\mu = \omega_{\mathrm{D}}/4$, the interaction strength $g = \omega_{\mathrm{D}}$, and the density of states in energy is taken as unity.

This Section has provided a summary of BCS theory, and an examination of the accuracy of the expansion method of evaluating the thermodynamic potential. In Chapter 6 the expansion method is used to investigate superconductivity in spin-

imbalanced systems, identifying unusual behaviour of the underlying Cooper pairs and commenting on its significance for experimental realisations of spin-imbalanced superconductivity.

Part I

Accelerating numerical simulations

Chapter 2

Pseudopotentials for an ultracold dipolar gas

A gas of ultracold molecules interacting via the long-range dipolar potential offers a highly controlled environment in which to study strongly correlated phases. However, at particle coalescence the divergent $1/r^3$ dipolar potential and associated pathological wavefunction hinder computational analysis. For a dipolar gas constrained to two dimensions we overcome these numerical difficulties by proposing a pseudopotential that is explicitly smooth at particle coalescence, resulting in a 2000-times speedup in diffusion Monte Carlo calculations. The pseudopotential delivers the scattering phase shifts of the dipolar interaction with an accuracy of 10^{-5} and predicts the energy of a dipolar gas to an accuracy of $10^{-4}E_{\mathrm{F}}$ in a diffusion Monte Carlo calculation.

19

2.1   Introduction

Ultracold atomic gases are an ideal testing ground for many-body quantum physics. Experiments now allow the condensation of particles that carry either an electric or magnetic dipole moment, and so interact through the long-ranged dipolar interaction in a highly controlled environment [3–12]. These systems present an ideal opportunity to study emergent strongly correlated phenomena driven by long-range interactions [46–56]. However, numerical studies of the dipolar interaction are complicated by the pathological behaviour of the wavefunction at particle coalescence. We propose a pseudopotential for the dipolar interaction that delivers almost identical scattering properties to the original dipolar interaction, but has a smooth profile that accelerates diffusion Monte Carlo calculations by a factor of ~ 2000.

In recent years there have been rapid developments in forming, trapping, and cooling ultracold atoms and molecules with dipole moments, as discussed in Chapter 1. For the sake of concreteness we consider a gas of fermionic dipolar particles [8, 9, 12]. A particularly appealing geometry is a single component gas of fermions trapped in two dimensions [7]. This configuration can suppress the chemical reaction rate of the molecules, thereby giving sufficient time to relax and study strongly correlated phases [13], and a strong external field can align the dipoles at an angle θ to the normal to the plane, which allows fine control over the interactions between the particles. The dipolar interaction between the particles is then $V(r,\phi) = d^2[1 - \frac{3}{2}\sin^2\theta(1 + \cos 2\phi)]/r^3$ where ϕ is the polar angle in the plane, measured from the projection of the electric field onto the plane, r is the interparticle distance, and d is the dipole moment. This interaction is shwon graphically in Section 2.6 below. We focus on the fully repulsive regime of the potential, with $\theta \leq \theta_{\rm c} = \arcsin(1/\sqrt{3})$, where there are no bound states. In the special case $\theta = 0$ the potential $V(r,\phi)$ reduces to the isotropic form $V(r) = d^2/r^3$.

Theoretical studies of the dipolar gas have provided a rich variety of surprises and insights. Remarkably, even at mean-field level the non-tilted ($\theta = 0$) system with an isotropic potential is predicted to display an inhomogeneous stripe phase [58,59] that is robust to the inclusion of perturbative quantum fluctuations [48]. To extend beyond the perturbative regime theorists have turned to diffusion Monte Carlo [60]: however, the divergent dipolar potential and associated pathological wavefunction make these simulations difficult to carry out, and they have not uncovered evidence

of the exotic inhomogeneous stripe phase.

The disagreement between analytical and numerical studies motivates us to focus our efforts on improving the modelling of the troublesome dipolar potential. Similar difficulties with divergent potentials arise in the study of the contact and Coulomb interactions, where it has been shown that pseudopotentials can accurately mimic the real interaction [61, 62]. We follow the same prescription to now construct a pseudopotential that delivers the same scattering physics as the dipolar interaction, but which is smooth at particle coalescence and so avoids the numerical difficulties arising from pathological behaviour near particle coalescence.

This smoothness will provide benefits in a variety of numerical techniques, including configuration interaction methods [63], coupled cluster theory [64], and diffusion Monte Carlo (DMC) [37]. Here we analyse the performance of the pseudopotential by carrying out DMC calculations on the dipolar gas to find the ground state energy of the system. We find that the proposed pseudopotential delivers ground state energies with an accuracy of order $10^{-4}E_{\mathrm{F}}$, whilst also offering a speedup by a factor of ~ 2000 relative to using the dipolar potential.

We start by studying the two-body scattering problem. In Section 2.2 we analytically solve the wavefunction of the non-tilted $\theta = 0$ system near to particle coalescence, which offers insights into the numerical difficulties. Building on the analytical solution, in Section 2.3 we numerically solve the two-body problem of scattering from the dipolar potential out to larger radii. This provides the scattering phase shift that we use to calibrate the scattering from the pseudopotential. Having proposed the pseudopotential, in Section 2.4 we test it on a second two-body system: two particles in a parabolic trap. In Section 2.5 we then demonstrate the use of the pseudopotential to study the ground state energy of the many-body fermionic gas, confirming both the accuracy of the pseudopotential and the computational speedup. In Section 2.6 we repeat the procedure with tilted dipoles, and in Section 2.7 discuss future applications of the pseudopotential.

2.2 Kato-like cusp conditions

To develop a pseudopotential for the dipolar interaction we need to properly understand scattering from the original dipole. Working with non-tilted dipoles, we focus on the small radius limit where we can solve for the wavefunction analytically.

This will allow us to demonstrate the pathological behaviour of the wavefunction and resultant numerical difficulties, and provide boundary conditions for the full numerical solution of the scattering properties. Moreover we will calculate a Kato-like cusp condition, a scheme to partially alleviate these numerical difficulties for the true dipolar potential.

To study the small radius behaviour we focus on the two-body problem: two identical same-spin fermions of mass m in their centre-of-mass frame with energy $E \geq 0$. The Hamiltonian in atomic units ($\hbar = m = 1$) is

$$\hat{H}\psi(r, \phi) = -\nabla^2\psi(r, \phi) + V(\hat{r})\psi(r, \phi) = E\psi(r, \phi), \qquad (2.1)$$

where $V(r) = d^2/r^3$ is the isotropic dipolar interaction for particle separation r and dipole strength d, with characteristic length scale $r_0 = d^2$.

A key quantity for Monte Carlo methods is the local energy, $E_{\mathrm{L}} = \psi^{-1}\hat{H}\psi$ [65]. For an eigenstate the local energy is constant, and equal to the eigenenergy, whilst for other wavefunctions the local energy varies in space. The foundation of the many-body trial wavefunction in our Monte Carlo calculations is a non-interacting wavefunction given by a Slater determinant of plane wave states. As two particles approach coalescence their contribution to the wavefunction in each angular momentum channel ℓ is $\psi_{\mathrm{non-int},\ell}(r, \phi) = r^\ell \cos(\ell\phi)$, which is an eigenstate of the two-body non-interacting system. The Slater determinant gives such a contribution in every odd angular momentum channel. In Fig. 2.1 we demonstrate that when this wavefunction is used with the dipolar potential the local energy diverges as r^{-3} in every angular momentum channel. This divergence is unwelcome as it will make the local energy difficult to sample in Monte Carlo calculations, and the variance of the samples will give rise to a large statistical uncertainty in the calculated energy.

To try to remedy this divergence in the local energy we examine the exact eigenstates of the two-body Hamiltonian given by Eq. (2.1), and then apply our findings to the many-body system. In the small separation limit where the potential $V(r)$ diverges the eigenstates of the Hamiltonian are

$$\psi_\ell(r, \phi) = K_{2\ell}(2\sqrt{r_0/r})\cos(\ell\phi),$$

where $K_n(x)$ is a modified Bessel function of the second kind and the quantum

Figure 2.1: (a) The local energy $E_{\mathrm{L}} = \psi^{-1}\hat{H}\psi$ as a function of radius in the $\ell = 1$ angular momentum channel, showing in orange the divergence as r^{-3} when the dipolar potential is used with the non-interacting wavefunction $\psi_{\mathrm{non-int},\ell=1}$. Also shown in magenta is the local energy divergence as $r^{-5/2}$ when the dipolar potential is used with a wavefunction with an exponential cusp correction $\psi_{\mathrm{exp},\ell=1}$, and in blue the exact solution in this channel, given by a Bessel function cusp correction $\psi_{K_2,\ell=1}$. In red and green are the local energies of Troullier–Martins and ultratransferable (UTP) pseudopotentials, respectively, with the non-interacting wavefunction, which outside of the radius r_{c} shown by a dashed grey line join smoothly onto the real dipolar potential. The inset shows the same curves on a logarithmic scale. (b) The local energy in the $\ell = 3$ channel, demonstrating that the Bessel function cusp correction $\psi_{K_2,\ell=3}$ is not accurate in other channels.
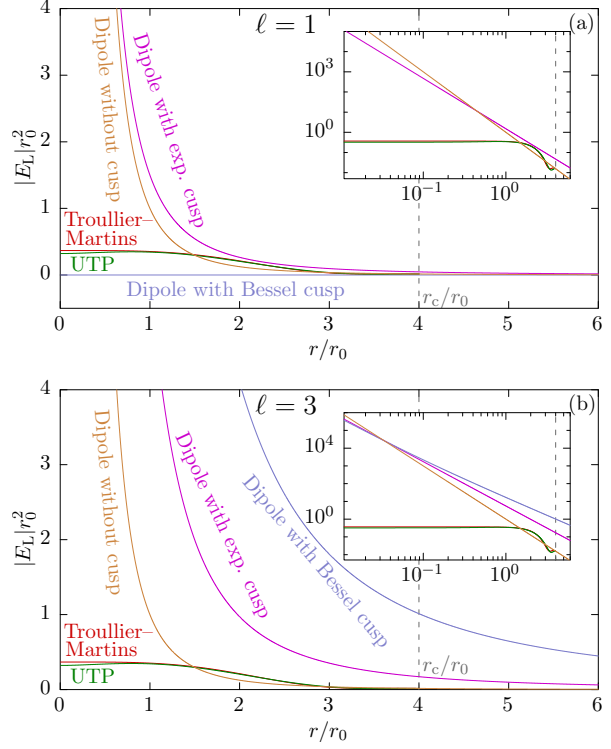
number ℓ denotes angular momentum in the 2D plane. In order to turn the leading-order $\ell = 1$ part of the non-interacting wavefunction given by the Slater determinant into an eigenstate of the Hamiltonian with the dipolar interaction we may multiply the Slater determinant by a factor $K_2(2\sqrt{r_0/r})/r$, which we refer to as a Bessel function cusp correction. This gives a wavefunction that is a zero-energy eigenstate of the Hamiltonian in the $\ell = 1$ channel, as shown in Fig. 2.1(a). Similar Bessel function cusp corrections have been used previously to study both fermionic and bosonic systems [49, 54, 60].

In Monte Carlo calculations we have to pre-multiply the entire Slater determinant, and so all angular momentum channels present in it, by a single cusp correction term, and it is not practical to adapt the cusp correction on the fly to the relative angular momentum of interacting particles. However, the Bessel function cusp correction applied to the two-body wavefunction,

$$\psi_{K_2,\ell}(r,\phi) = r^\ell \cos(\ell\phi) K_2(2\sqrt{r_0/r})/r,$$

is not an eigenstate in any angular momentum channel except $\ell = 1$. In other channels it gives a local energy that diverges as $r^{-5/2}$ in the $r \to 0$ limit, as shown in Fig. 2.1(b) for the $\ell = 3$ channel.

The improvement of the divergence in the local energy from r^{-3} to $r^{-5/2}$ is, in fact, due to the leading-order behaviour of the Bessel function cusp correction, which goes as $\exp(-2\sqrt{r_0/r})$, independent of angular momentum. Accepting that we will always be left with an $r^{-5/2}$ divergence of the local energy in many-body calculations, we may then just take this leading order term to give an exponential cusp correction, leading to a wavefunction

$$\psi_{\exp,\ell}(r,\phi) = r^\ell \cos(\ell\phi) \exp(-2\sqrt{r_0/r}).$$

The $r^{-5/2}$ divergence of the local energy with this wavefunction is shown in Fig. 2.1 for angular momentum channels $\ell = 1$ and $\ell = 3$.

The approach of inserting a small radius analytical solution into the many-body trial wavefunction is well established in electronic-structure calculations where the small radius behaviour of the wavefunction around the $1/r$ divergence in the Coulomb potential is fixed with the Kato cusp conditions [66, 67]. Following this

prescription we can premultiply a many-body non-interacting trial wavefunction by the exponential cusp correction $\prod_{i>j} \exp(-2\sqrt{r_0/r_{ij}})$ or Bessel function cusp correction $\prod_{i>j} K_{2\ell}(2\sqrt{r_0/r_{ij}})/r_{ij}^\ell$, where the product is over all dipoles labelled by i, j and r_{ij} is the dipole-dipole separation. Similarly to the two-body case both corrections leave an $r^{-5/2}$ divergence in the local energy, which will manifest itself as a major contribution to the uncertainty in the final prediction of the energy. We will revisit the question of cusp corrections in a many-body system in Fig. 2.5(b), where we show that the simple exponential cusp correction gives similar values for the variance in the local energy to a full Bessel function cusp correction.

In order to study the interacting-dipole system further we turn to the construction of pseudopotentials [61, 68] that capture the physics of the system whilst delivering the smooth and non-divergent local energy values shown in Fig. 2.1.

2.3 Derivation of the pseudopotentials

To construct a pseudopotential for the dipolar interaction we continue with the two-body scattering problem of two indistinguishable fermions in their centre-of-mass frame, studying the Schrödinger Eq. (2.1). We seek a pseudopotential that is smooth and non-divergent to accelerate numerical calculations. We also require it to reproduce the correct two-body scattering physics over the range of scattering energies present in a Fermi gas with Fermi energy E_{F}, which guarantees that the pseudopotential will properly capture two-body effects in the system. As we will be considering two-body processes we again work in the centre-of-mass frame, with the Hamiltonian given by Eq. (2.1).

We first turn to the Troullier–Martins [68] formalism that has been widely used and rigorously tested in the literature to construct attractive electron-ion pseudopotentials [69–74], but which may be adapted [61] to the current problem of two identical fermions as detailed in Appendix A. This method creates a pseudopotential with the exact dipolar potential outside of a cutoff radius r_{c} and a polynomial potential within it, constructed to be smooth up to second derivative at r_{c}. The Troullier–Martins method guarantees that the scattering properties of the pseudopotential will be exact at one particular calibration energy E_{c}. We choose the calibration energy to be the average scattering energy of two fermions in a non-interacting Fermi gas. In Appendix B we show that this calibration energy is $E_{\mathrm{c}} = E_{\mathrm{F}}/4$.

For the scattering of two indistinguishable fermions the Pauli principle guarantees that there will be no s-wave contribution to the scattering. We therefore construct the Troullier–Martins pseudopotential by focusing on a scattering wavefunction in the leading-order p-wave, $\ell = 1$, channel. The functional form of the pseudo-wavefunction in this channel is

$$\psi_{\ell=1}(r,\phi) = \begin{cases} \exp[p(r)]\, r\cos(\phi)\,, & r < r_{\mathrm{c}}\,, \\ \psi_{\mathrm{dipole},\ell=1}(r,\phi)\,, & r \geq r_{\mathrm{c}}\,, \end{cases} \tag{2.2}$$

where the polynomial $p(r) = \sum_{i=0}^{6} c_i r^{2i}$, and the wavefunction $\psi_{\mathrm{dipole},\ell=1}(r,\phi)$ is calculated by numerically solving Eq. (2.1) using the exact dipolar potential at the calibration energy E_{c}. As explained in Appendix A the coefficients c_i are calculated by requiring continuity of the pseudo-wavefunction and its first four derivatives at r_{c}, as well as matching the net density inside r_{c}, and requiring the pseudopotential to have zero gradient and curvature at the origin.

The choice of r_{c} is motivated by the physics we wish to study: a longer cutoff radius allows a smoother potential that gives efficient numerics, but being less similar to the real potential has less accurate phase shift errors. In many-body systems the longer cutoff radius will also increase the probability of having three or more particles within the cutoff radius, which the pseudopotential is not designed to be able to accurately model. For our two-body scattering system we take $k_{\mathrm{F}} r_{\mathrm{c}} = 2$, which ensures that, on average, only one other particle is within r_{c} of each scattering particle, and so avoids three-body interactions within the cutoff radius.

The exponentiated polynomial form of the pseudo-wavefunction in Eq. (2.2) means that the Schrödinger Eq. (2.1) may be analytically inverted to give the pseudopotential as

$$V_{\mathrm{T\text{-}M}}(r) = \begin{cases} E_{\mathrm{c}} + \frac{3}{r}p' + p'^2 + p''\,, & r < r_{\mathrm{c}}\,, \\ d^2/r^3\,, & r \geq r_{\mathrm{c}}, \end{cases} \tag{2.3}$$

where the primes denote differentiation with respect to r. This pseudopotential is shown in red in Fig. 2.2 for interaction strength $k_{\mathrm{F}} r_0 = 1/2$. It is non-divergent at particle coalescence and smooth where it joins onto the real dipolar potential at $r = r_{\mathrm{c}}$. This pseudopotential gives rise to the local energy E_{L} shown in Fig. 2.1.

Figure 2.2: The dipolar potential, and Troullier–Martins and UTP pseudopotentials. The grey vertical line indicates r_c, the pseudopotential cutoff radius.
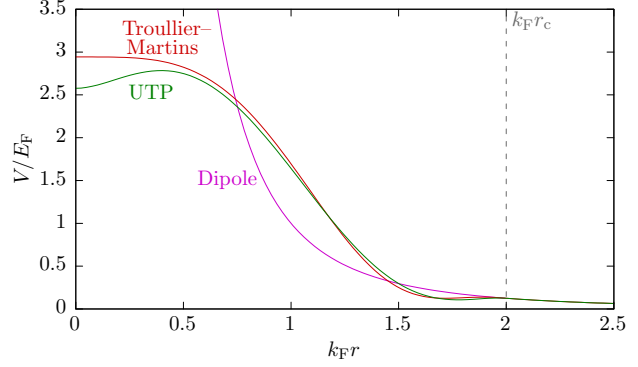
The smooth and finite local energy at $r < r_c$ is a dramatic improvement over the divergent local energy from our trial wavefunction with the dipolar potential, and this non-divergence should lead to improved statistics and efficiency in many-body simulations.

To measure the accuracy of our pseudopotentials we calculate the phase shift in the wavefunction

$$\delta_{\psi,\ell}(E) = \frac{1}{2\pi} \text{arccot}\left[\frac{1}{\sqrt{E}}\left(\frac{\psi'_\ell(r_c,\phi)}{\psi_\ell(r_c,\phi)} + \frac{2\ell+1}{2r_c}\right)\right] \tag{2.4}$$

imparted by a two-body scattering process, where $\delta_{\psi,\ell}$ is evaluated at the cutoff radius r_c because any difference in phase shift must be accumulated in the region $r < r_c$ where the potentials differ. The difference between the scattering phase shift for the Troullier–Martins pseudopotential and the exact phase shift from the dipolar interaction is shown in red in Fig. 2.3(a) as a function of scattering energy, evaluated at $k_F r_0 = 1/2$. The scattering phase shift of the Troullier–Martins pseudopotential is exact at the calibration energy, and accurate to order 10^{-5} over the range of scattering energies in a Fermi sea.

Although the Troullier–Martins pseudopotential captures the exact scattering properties at the calibration energy, it deviates at all other energies, with the leading order deviation around the calibration energy going as $(E - E_c)^2$ [61]. A natural extension to the Troullier–Martins formalism is to find a pseudopotential that minimises this deviation in the phase shift over all the possible relative energies of pairs of particles in a Fermi gas. We derive such a pseudopotential here, referring to it as an "ultratransferable pseudopotential" (UTP).

The UTP [61] is identical to the dipolar potential outside a cutoff radius r_c, but
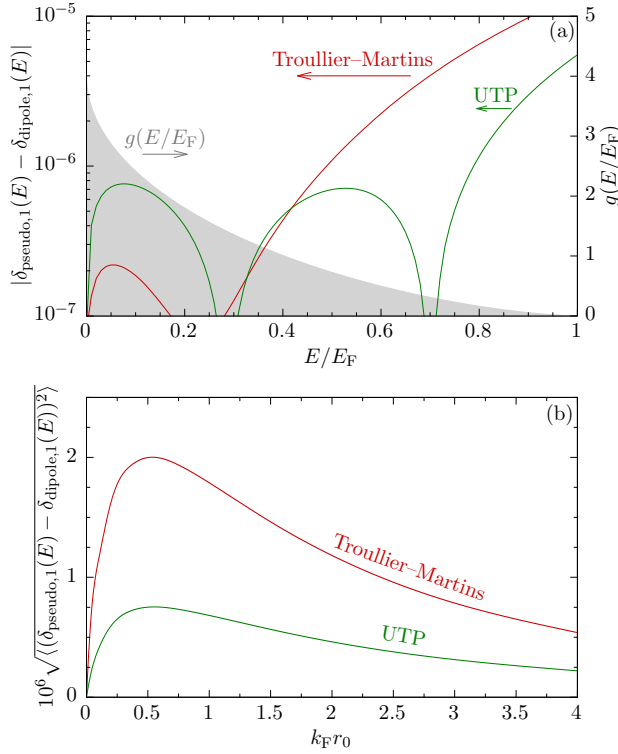
Figure 2.3: (a) The error in the scattering phase shift $|\delta_{\mathrm{pseudo},1}(E) - \delta_{\mathrm{dipole},1}(E)|$. The filled grey curve is the density of scattering states $g(E)$ in the two-body Fermi sea on a linear scale. (b) The root-mean-squared error in the scattering phase shift as a function of interaction strength.

has a polynomial form inside the cutoff,

$$
V_{\mathrm{UTP}}(r) = \frac{d^2}{r_{\mathrm{c}}^3}
\begin{cases}
\begin{aligned}
& 1 + 3\left(1 - \frac{r}{r_{\mathrm{c}}}\right)\left(\frac{r}{r_{\mathrm{c}}}\right)^2 \\
& \quad + \left(1 - \frac{r}{r_{\mathrm{c}}}\right)^2 \left[v_1\left(\frac{1}{2} + \frac{r}{r_{\mathrm{c}}}\right) + \sum_{i=2}^{N_v} v_i \left(\frac{r}{r_{\mathrm{c}}}\right)^i \right],
\end{aligned}
& r < r_{\mathrm{c}}, \\[2em]
r_{\mathrm{c}}^3/r^3, & r \geq r_{\mathrm{c}},
\end{cases}
$$

with $N_v = 3$. The term $1 + 3(1 - r/r_{\mathrm{c}})(r/r_{\mathrm{c}})^2$ guarantees that the potential and its first derivative are continuous at $r = r_{\mathrm{c}}$. In the next term, the expression $(1 - r/r_{\mathrm{c}})^2$ also ensures continuity of the potential at the cutoff radius, and $v_1(1/2 + r/r_{\mathrm{c}})$ constrains the potential to have zero derivative at the origin. This ensures that the pseudo-wavefunction is smooth, easing the application of numerical methods.

To determine the coefficients $\{v_i\}$ we minimise the total squared error in the

phase shift over all the possible pairs of interacting particles in a Fermi gas

$$\left\langle \left| \delta_{\mathrm{UTP},\ell}\left(E\right) - \delta_{\mathrm{dipole},\ell}\left(E\right) \right|^2 \right\rangle$$
$$= \int \left| \delta_{\mathrm{UTP},\ell}\left(E\right) - \delta_{\mathrm{dipole},\ell}\left(E\right) \right|^2 g(E/E_{\mathrm{F}})\, \mathrm{d}E/E_{\mathrm{F}}\,, \qquad (2.5)$$

where

$$g(x) = 4 - \frac{8}{\pi}\left(\sqrt{x(1-x)} + \arcsin\sqrt{x} \right)$$

is the density of scattering states in energy (see Appendix B and Reference [75]), shown in Fig. 2.3(a). The density of scattering states decreases as a function of energy due to the finite size of the Fermi sea of scattering particles limiting the available range of scattering energies. Modifyications to this density of scattering states, perhaps to weight scattering states near the Fermi surfaces more heavily, are expected to only weakly change the derived UTP. We primarily work in the leading-order $\ell = 1$ angular momentum channel. The UTP formalism is capable of creating pseudopotentials that are accurate in several angular momentum channels by summing over them in Equation (2.5) whilst accounting for the occupation of the channels that goes as $1/\sqrt{(2\ell+1)!!}$ [62], which strongly suppresses the effect of all the channels above $\ell = 1$. The total squared phase shift error Eq. (2.5) is numerically minimised with respect to the v_i to create our UTP.

The scattering phase shift behaviour of the UTP is shown in Fig. 2.3(a). Although it is less accurate than the Troullier–Martins pseudopotential at the Troullier–Martins calibration energy, the UTP is more accurate at higher incident energies. At zero scattering energy both pseudopotentials are exact, as the scattering particles never penetrate the region $r < r_{\mathrm{c}}$ where the pseudopotentials deviate from the real dipolar interaction.

In Fig. 2.3(b) we show the average phase shift error in the pseudopotentials as a function of interaction strength. At its worst the Troullier–Martins pseudopotential has an average accuracy of 2×10^{-6}, whilst the average UTP accuracy is always better than 1×10^{-6}. Over a broad range of interaction strengths the UTP is more accurate than the Troullier–Martins pseudopotential, but both are exact at $k_{\mathrm{F}}r_0 = 0$ where the particles do not interact. At high interaction strengths the pseudopotentials become highly accurate, as the increasing interaction strength effectively rescales
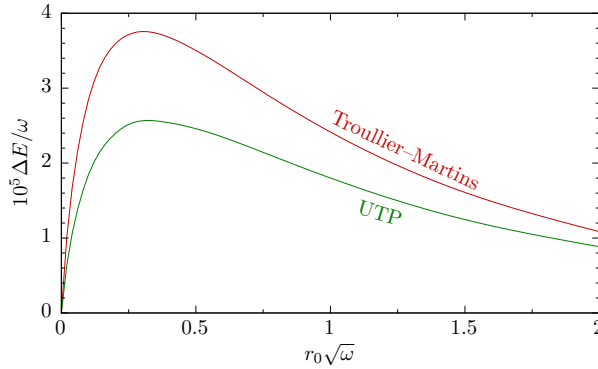
Figure 2.4: The deviation of the energy of two particles in an harmonic trap as calculated using both Troullier–Martins and UTP pseudopotentials from that calculated using the exact dipolar potential, as a function of interaction strength.

the potential size, and so for a given range of scattering energies the particles will be kept further apart and so less strongly probe the region $r < r_{\mathrm{c}}$ where the potentials differ. We also note that a further advantage of the UTP is that at high interaction strengths, $k_{\mathrm{F}} r_0 > 4$ with $k_{\mathrm{F}} r_{\mathrm{c}} = 2$, it is not possible to solve the system of equations defining the Troullier–Martins pseudopotential, whilst it is still possible to derive a UTP.

Having constructed two different pseudopotentials and demonstrated their accuracy in a homogeneous two-body setting, we now test their flexibility by solving an inhomogeneous two-body system.

2.4   Two fermions in an harmonic trap

We have developed pseudopotentials that exhibit the correct scattering properties for an isolated two-body system. To test them we turn to the experimentally realisable [76, 77] configuration of two fermionic dipolar particles aligned by an external field and held in a circularly symmetric two-dimensional harmonic well with trapping frequency ω. Given that the identical fermions must be in different single-particle states of the harmonic trap the non-interacting energy of the reduced system is 2ω. This system is a good place to test our pseudopotentials as it has a non-trivial background potential, but at the same time is still simple enough to solve accurately with the real dipolar potential.

We calculate the energy of two particles held in such a trap by solving the

Schrödinger equation for the relative motion in the system,

$$-\nabla^2\psi + \frac{1}{4}\omega^2 r^2\psi + V(r)\psi = E\psi \,, \tag{2.6}$$

with $V(r)$ set as either the exact dipolar potential or a pseudopotential. We solve the system in the lowest-energy $\ell = 1$ angular momentum channel available to identical fermions, calibrating the Troullier–Martins pseudopotential at $E_{\mathrm{c}} = (2\omega)/4 = \omega/2$ by analogy to the homogeneous system. For the cutoff radius r_{c} we choose the characteristic width of the trap, $1/\sqrt{\omega}$.

The energy differences between the pseudopotential and exact dipolar solutions to Equation (2.6) are shown in Fig. 2.4 as a function of interaction strength. Approaching zero interaction strength the form of the interaction potential has diminishing impact, and so the difference in energies goes to zero; and in the high-interaction strength limit the particles are kept further apart by the strong potential, so less strongly probe $r < r_{\mathrm{c}}$ where the potentials differ and again the error in the ground state energy becomes negligible. At intermediate interaction strengths $r_0\sqrt{\omega} \approx 1/4$ the pseudopotentials are still accurate to order $10^{-5}\omega$, which exceeds the $\sim 10^{-4}\omega$ accuracy attainable in exact diagonalisation of this system [78] and many-body quantum Monte Carlo calculations [60, 61, 79]. The UTP provides an improvement in accuracy over the Troullier–Martins pseudopotential at all interaction strengths.

2.5   Fermi gas

Having demonstrated that the Troullier–Martins and UTP pseudopotentials are accurate tools for studying both scattering and inhomogeneous trapped two-body systems, we are well placed to test the pseudopotentials in a many-body system: a gas of fermionic dipolar particles. The particles are constrained to lie in two dimensions with all their dipole moments aligned normal to the plane, which has been suggested for experimental investigation [7]. We use diffusion Monte Carlo (DMC) calculations to study the system, using the CASINO code [65].

2.5.1 Formalism

Our DMC calculations use 81 particles per simulation cell and a Slater–Jastrow type wavefunction $\Psi = \mathrm{e}^J D$. Here D is a Slater determinant of plane-wave orbitals, with wavevectors given by the reciprocal lattice vectors of our simulation cell, and the Jastrow factor e^J describes the interparticle correlations [80], with

$$J = \sum_{i \neq j} \left(\sum_{k=0}^{N_\mathrm{u}} u_k r_{ij}^k \left(1 - \frac{r_{ij}}{L} \right)^3 \Theta \left(L - r_{ij} \right) + \sum_{\mathbf{G}} p_{|\mathbf{G}|} \cos(\mathbf{G} \cdot \mathbf{r}_{ij}) \right), \qquad (2.7)$$

where the first sum runs over all particles labelled i, j with separation $\mathbf{r}_{ij}$, $N_\mathrm{u} = 7$, and the $\mathbf{G}$ vectors are the 36 shortest reciprocal lattice vectors (first 8 sets of equal-length reciprocal lattice vectors). The cutoff function $(1 - r_{ij}/L)^3$ ensures that the wavefunction's first two derivatives go smoothly to zero at a radius L, chosen to be the Wigner-Seitz radius of the simulation cell. Calculations with the exact dipolar interaction have a cusp correction term in the Jastrow factor, using the exponential form $\prod_{i>j} \exp(-2\sqrt{r_0/r_{ij}})$ as discussed in Section 2.2. We also test the Bessel function cusp correction proposed in Reference [60]. The coefficients $\{u_k\}$ and $\{p_{|\mathbf{G}|}\}$ are optimised in a variational Monte Carlo calculation, and then this optimised wavefunction is taken as the trial wavefunction for a DMC calculation to evaluate the ground state energy.

We use 4000 particle configurations in DMC, and by running tests with 2000, 4000, and 8000 configurations checked that 4000 configurations gives results within statistical uncertainty of the extrapolated result with an infinite number of configurations. Similarly we checked that our system of 81 particles gave similar results to systems of 45 and 145 particles, although a full extrapolation of results to the thermodynamic limit is not necessary to verify the accuracy of short ranged pseudopotentials, and so not a focus of this work. We did however correct the non-interacting energy of the system to the result of the infinite system, to reduce finite-size effects in the calculation [61, 81].

To evaluate the dipolar interaction we explicitly sum over pairs of particles within a distance R_s of each other, and then include the effect of particles further apart by integrating over them, assuming a uniform particle density. By taking R_s as ~ 18 simulation cell lattice vectors the error due to the finite value of R_s is smaller than $10^{-6} E_\mathrm{F}$, and therefore negligible compared to our DMC statistical errors [60, 82].

Figure 2.5: (a) The variation of the energy per particle in the Fermi gas with pseudopotential cutoff radius, calculated using DMC. The red points are for the Troullier–Martins pseudopotential, the green a UTP pseudopotential, and the magenta point is the exact dipolar potential. Stochastic error bars are of order $10^{-5}E_{\rm F}$. The vertical dashed line denotes the recommended cutoff radius. (b) The variance in the individual local energy samples (as seen in Fig. 2.1) taken during a DMC calculation using the pseudopotentials. Also shown are results for the dipolar potential both with and without Kato-like cusp corrections applied.
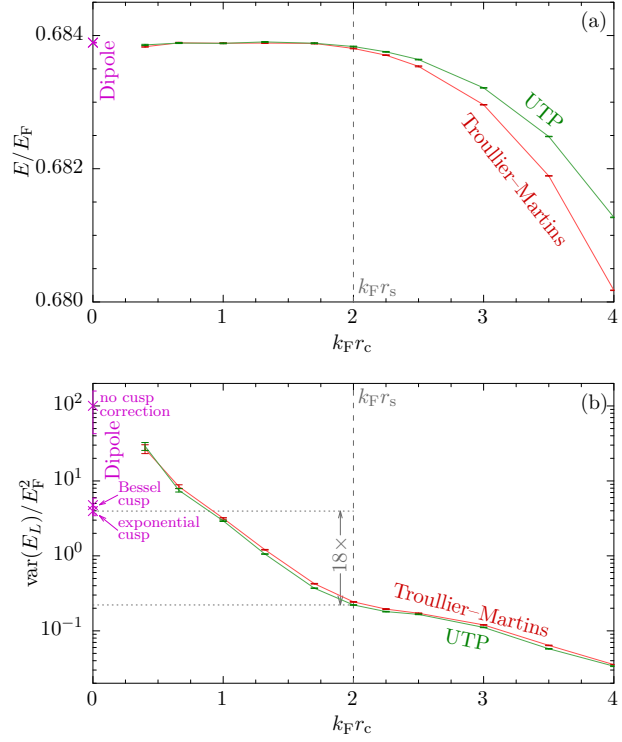
In order to analyse the accuracy of our pseudopotentials in capturing the dipolar gas, we start by fixing the interaction strength and investigate the dependence of the accuracy on the cutoff radius $r_{\rm c}$. Having selected a cutoff radius we then study the effect of the DMC timestep τ, and finally present results at a variety of interaction strengths.

In simulations using the pseudopotentials decreasing the cutoff radius makes the calculation more accurate by increasing the similarity to the real potential and reducing the likelihood of three-body interactions within the cutoff radius. This is shown in Fig. 2.5(a), calculated at $k_{\rm F}r_0 = 1/2$ with timestep $\tau E_{\rm F} = 0.0092$. However, this increased similarity to the dipolar potential also has the effect of increasing the variance in the individual local energy samples taken during the simulation, as shown in Fig. 2.5(b), which the runtime of a DMC calculation is proportional to [37]. When using the pseudopotentials a balance therefore has to be struck between accuracy and speedup: we choose to take the cutoff radius as equal to $r_{\rm s}$, the density parameter that corresponds to the average separation of particles. This gives DMC calculations with an accuracy of order $10^{-4}E_{\rm F}$, whilst as shown in Fig. 2.5(a) this

accuracy quickly drops off for $r_c > r_s$.

In Fig. 2.5(b) we compare the variance in the individual local energy samples from the pseudopotentials to that from the real dipolar potential, using wavefunctions both with and without Kato-like cusp corrections applied. The two forms of cusp correction, the Bessel function cusp correction proposed for this system in Reference [60] and our simpler exponential cusp correction, agree to within statistical uncertainty. As discussed in Section 2.2 this is because both give rise to $r^{-5/2}$ divergences in the local energy, which are preferable to the higher variance in the local energy from the bare dipolar potential, which diverges as r^{-3}. The source of this divergence is, however, more transparent for the exponential cusp correction than the Bessel function cusp correction, and so we use the exponential form in the rest of our calculations.

Taking $r_c = r_s$ for the cutoff radius gives an 18-times reduction in the variance of the local energy samples of the many-body system using a pseudopotential when compared to using the real dipolar interaction with a Kato-like exponential cusp correction. To get the same statistical error in our results we therefore need to take 18 times fewer samples, leading to an 18-times statistical speedup in calculations.

There is however an additional speedup benefit from using the pseudopotential. The random walk in the DMC calculations is performed at a finite timestep τ [65, 83]. The use of a short-time approximation in the DMC algorithm gives rise to a linear dependence of the final estimate of the energy on τ [65]. If we were to use a short timestep to remove this systematic error the DMC walkers would not be able to move far in configuration space in each step, giving rise to serial correlations in the calculated values of the energy, and an explicit $\tau^{-1/2}$ dependence of the statistical standard error in the energy [84]. These two competing effects are shown in Fig. 2.6(a) and Fig. 2.6(b) respectively for our Fermi gas at $k_F r_0 = 1/2$. The dependence on the energy on τ is both flatter when using the UTP compared to the dipolar potential, and also retains its linear form out to larger timesteps: this is advantageous as it allows the use of longer timesteps in DMC, which is more efficient. Fig. 2.6(b) confirms the $\tau^{-1/2}$ dependence of the standard error in the energy, and that the smoothness of the UTP delivers a smaller standard error.

We express the linear short-time approximation as giving an offset in the calculated energy of $a\tau$, where a is a fitting parameter, and the serial correlations as giving a variance in the energy of $s_E^2 = \sigma^2 N^{-1}\tau^{-1}$, with σ being a fitting parameter.

Figure 2.6: (a) The variation of the energy per particle in the Fermi gas with timestep τ. The magenta points are using the exact dipolar potential, and the green points using a UTP pseudopotential. The error bars show DMC stochastic errors, and are of order $10^{-5}E_F$. Fitted values of the linear error parameters a (see main text) are also given. (b) The standard error s_E in the energy per particle in the Fermi gas, for both the dipolar potential and UTP pseudopotential. Values of the fitting parameters σ for a $1/\sqrt{\tau}$ fit are also given for each.
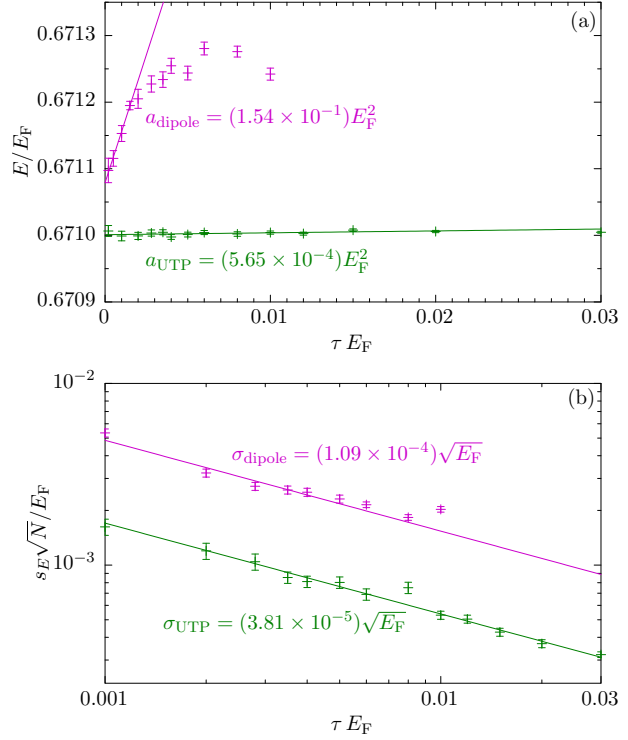
The statistical error can be reduced by taking more samples N [37]. We can then express the expected value of the square error in the energy as being distributed to leading order as a Gaussian [62, 85]

$$\left\langle \Delta E^2 \right\rangle = \int \Delta E^2 \mathrm{e}^{-\frac{(\Delta E - a\tau)^2}{2\sigma^2 N^{-1}\tau^{-1}}} \mathrm{d}(\Delta E)$$

$$= a^2\tau^2 + \sigma^2 N^{-1}\tau^{-1}. \tag{2.8}$$

The expected square error in the energy is minimised at the optimal timestep

$$\tau_{\text{optimum}} = \left(\frac{1}{2}\frac{\sigma^2}{a^2}\frac{1}{N} \right)^{1/3},$$

and substituting this into Eq. (2.8), the ratio of the number of steps required to give the same expected square error in the energy when using the dipolar potential and
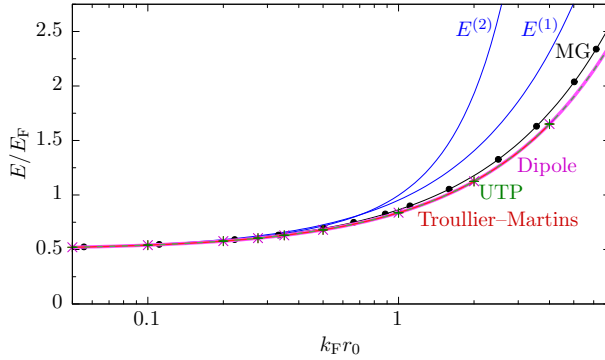
Figure 2.7: The equation of state of the 2D isotropic, homogeneous dipolar gas. The blue curves show the first- and second-order perturbation theory ($E^{(1)}$ and $E^{(2)}$) equations of state [75], and our DMC data are shown in: magenta, for the dipolar potential; red for the Troullier–Martins pseudopotential calibrated at $E_{\mathrm{F}}/4$; and green for a UTP. The latter three curves overlie each other to within the width of the plotted lines. Stochastic error bars are of order $10^{-5} E_{\mathrm{F}}$. The black circles show data from DMC calculations using the dipolar potential by Matveeva and Giorgini (MG) in Reference [60].

the UTP is

$$\frac{a_{\mathrm{dipole}} \sigma_{\mathrm{dipole}}^2}{a_{\mathrm{UTP}} \sigma_{\mathrm{UTP}}^2}. \tag{2.9}$$

For the values of the fitting parameters a and σ in Fig. 2.6 this gives a ratio of required number of steps and hence speedup when using the pseudopotential of $\sim$ 2230. This value for the speedup includes the variance difference of 18 that was found with the recommended value of r_{c}, the remainder coming from the improvement of the finite timestep behaviour when using the pseudopotential.

Use of a second order propagator in the DMC algorithm might improve the efficiency of the calculations by allowing the use of a longer timestep than was possible here [86–88]. In a second order DMC algorithm the square error in the energy would take the form $\langle \Delta E^2 \rangle = b^4 \tau^4 + \sigma^2 N^{-1} \tau^{-1}$. The parameter b, which is zero if the exact wavefunction is used in DMC, should grow with the standard deviation in the local energy. This same effect is seen in Fig. 2.6(a) and in the results of Reference [62]. We therefore expect $b_{\mathrm{UTP}} < b_{\mathrm{dipole}}$, and saw above that $\sigma_{\mathrm{UTP}} < \sigma_{\mathrm{dipole}}$. With this form of the square error in the energy, the speedup when using the pseudopotential relative to the real dipolar potential would take the form

Figure 2.8: The deviation of the equation of state as calculated using the pseudopotentials from that calculated using the exact dipolar potential. The dipolar potential is shown in magenta, with the Troullier–Martins pseudopotential in red, the UTP in green, and first- and second-order perturbation theory ($E^{(1)}$ and $E^{(2)}$) in blue. The grey box around the results using the dipolar potential shows the target $3 \times 10^{-4} E_{\mathrm{F}}$ accuracy level.
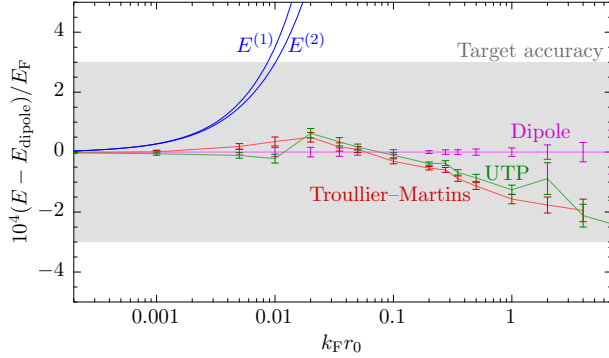
$b_{\mathrm{dipole}} \sigma_{\mathrm{dipole}}^2 / (b_{\mathrm{UTP}} \sigma_{\mathrm{UTP}}^2)$. We obtain the same statistical speedup as in the linear case from the factor $\sigma_{\mathrm{dipole}}^2 / \sigma_{\mathrm{UTP}}^2$, and the ratio $b_{\mathrm{dipole}} / b_{\mathrm{UTP}}$ should be greater than 1, as was found for the ratio $a_{\mathrm{dipole}} / a_{\mathrm{UTP}}$ in the linear case, to further increase the speedup.

Recognising that our pseudopotential gives accurate results with around 2000-times smaller computational outlay than using the real dipolar interaction, we now investigate the third parameter that could affect the accuracy, interaction strength.

2.5.2 Equation of state

We compare the equations of state of the 2D dipolar Fermi gas as calculated using the exact dipolar potential and the Troullier–Martins and UTP pseudopotentials in Fig. 2.7. The pseudopotential cutoff is taken as $r_{\mathrm{c}} = r_{\mathrm{s}}$ and we extrapolate to zero timestep following the procedure outlined in Reference [83]. We find the equations of state to be the same to order $10^{-4} E_{\mathrm{F}}$. Shown as black circles in Fig. 2.7 is the equation of state of the system as calculated using DMC by Matveeva and Giorgini (MG) in Reference [60]. We explicitly repeat the simulation of Reference [60], using the same system of 81 particles, but our calculated energies using the dipolar potential are of order $10^{-2} E_{\mathrm{F}}$ lower than reported there, and as DMC is a variational technique this indicates that our trial wavefunction is likely more accurate than was available to the authors of Reference [60], possibly due to our inclusion of a Jastrow factor with variational parameters. On the scale of Fig. 2.7 it is not possible to
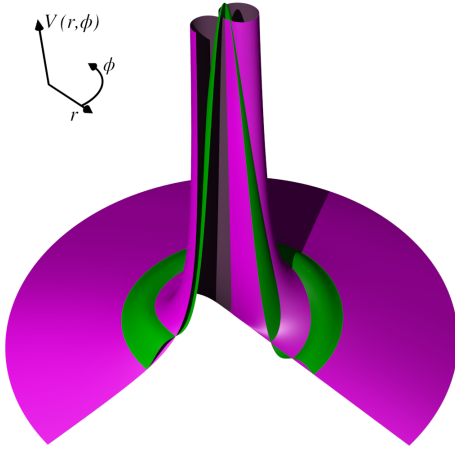
Figure 2.9: The dipolar potential $V(r, \phi)$ in magenta, and the UTP $V_{\mathrm{UTP}}(r, \phi)$ for the same tilt angle, in green. The potentials are cut through for $3\pi/2 < \phi < 2\pi$ to contrast the radial variation of the dipolar potential along $\phi = 3\pi/2$ and $\phi = 2\pi$, and show the smooth join of the UTP onto the dipolar potential at $r = r_{\mathrm{c}}$.

distinguish our pseudopotential calculations from those using the real dipolar interaction, and so in order to properly analyse them we examine the error from the true dipolar potential in Fig. 2.8.

Following the accuracy used in Reference [60] to draw conclusions about which phases are energetically favourable in the dipolar gas, we choose a target accuracy of $3 \times 10^{-4} E_{\mathrm{F}}$ for our pseudopotentials, shown as a grey box in Fig. 2.8. Over a wide range of interaction strengths our pseudopotentials fall within this accuracy, with the UTP being slightly more accurate than the Troullier–Martins pseudopotential at most interaction strengths. We also compare our DMC results to second-order perturbation theory [75, 89]

$$E^{(2)} = \frac{E_{\mathrm{F}}}{2} \left[1 + \frac{128}{45\pi} k_{\mathrm{F}} r_0 + \frac{1}{4} (k_{\mathrm{F}} r_0)^2 \ln(1.43 k_{\mathrm{F}} r_0) \right],$$

noting that it differs significantly from the DMC results above interaction strengths of $k_{\mathrm{F}} r_0 \gtrsim 0.01$. In Fig. 2.7 we also note that above $k_{\mathrm{F}} r_0 \gtrsim 1$ first-order perturbation theory is more accurate than $E^{(2)}$, indicating that perturbation theory is not an adequate approximation except at very low interaction strengths $k_{\mathrm{F}} r_0 \ll 0.01$.

We have constructed and tested pseudopotentials using the Troullier–Martins and UTP methods. In each test, shown in Figures 2.3(b), 2.4, and 2.8, the UTP method has given more accurate results. We therefore recommend the use of the UTP method to construct pseudopotentials for the dipolar interaction, and recommend its use over the dipolar potential with a cusp correction due to the 2000-times speedup in calculations that can be achieved whilst still achieving sufficient accu-

racy. We now go on to show that the UTP can be generalised to capture the effects of an anisotropic interaction in a system of tilted dipoles.

2.6   Tilted dipoles

The above analysis has focused on dipoles aligned normal to their 2D plane of motion by an external electric or magnetic field. However, this same electric or magnetic field could be used to align the dipoles at an angle θ to the normal to the plane [7]. The dipolar interaction then takes the anisotropic form $V(r, \phi) = d^2[1 - \frac{3}{2}\sin^2\theta(1 + \cos 2\phi)]/r^3$ where ϕ is the polar angle in the plane, between the dipole-dipole separation and the projection of the electric field. We focus on the $\theta \leq \theta_{\mathrm{c}} = \arcsin(1/\sqrt{3})$ regime, where the potential is purely repulsive and there are no bound states. The potential $V(r, \phi)$ is shown in magenta in Fig. 2.9 for $\theta = \theta_{\mathrm{c}}$ and $k_{\mathrm{F}}r_0 = 1/2$. As well as the r^{-3} divergence, the potential is strongly anisotropic, separating into two lobes. These properties make it difficult to work with numerically, and so we again develop a pseudopotential to ease the numerical simulation of this system.

The Troullier–Martins formalism used in the non-tilted system is not applicable to the case of $\theta > 0$, and so here we propose the UTP

$$V_{\mathrm{UTP}}(r,\phi) = \frac{d^2}{r_{\mathrm{c}}^3} \begin{cases} \begin{aligned} & \left[1 - \tfrac{3}{2}\sin^2\theta(1+\cos 2\phi)\right] \\[2ex] & + 3\left(1 - \tfrac{r}{r_{\mathrm{c}}}\right)\left(\tfrac{r}{r_{\mathrm{c}}}\right)^2 \left[1 - \tfrac{3}{2}\sin^2\theta(1+\cos 2\phi)\right] \\[2ex] & + \left(1 - \tfrac{r}{r_{\mathrm{c}}}\right)^2 \left(1 - \tfrac{3}{2}\sin^2\theta\right)\left[v_1\left(\tfrac{1}{2} + \tfrac{r}{r_{\mathrm{c}}}\right)\right. \\[2ex] & \hspace{5em} \left. + \sum_{i=2}^{N_v} v_i\left(\tfrac{r}{r_{\mathrm{c}}}\right)^i\right] \\[2ex] & + \sin^2\theta\cos 2\phi\left[\left(1 - \tfrac{r}{r_{\mathrm{c}}}\right)^2 v_{N_v+1}\left(\tfrac{r}{r_{\mathrm{c}}}\right)^2\right. \\[2ex] & \hspace{3em} \left. + 3\left(\tfrac{1}{2} - \tfrac{3}{2}\left(\tfrac{r}{r_{\mathrm{c}}}\right)^2 + \left(\tfrac{r}{r_{\mathrm{c}}}\right)^3\right)\right], \qquad r < r_{\mathrm{c}}, \\[2ex] & \left[1 - \tfrac{3}{2}\sin^2\theta(1+\cos 2\phi)\right] r_{\mathrm{c}}^3/r^3, \qquad\qquad\quad r \geq r_{\mathrm{c}}, \end{aligned} \end{cases}$$

$$(2.10)$$

which is constrained to be smooth to first derivative in both radial and azimuthal directions at the origin and at r_{c}, where it joins onto the exact dipolar potential. N_v is again set as 3, and the coefficients $\{v_i\}$ are minimised similarly to the non-tilted case. At $\theta = 0$ Eq. (2.10) reduces to the non-tilted form. A sample UTP is shown along with the tilted dipolar potential in Fig. 2.9, demonstrating its non-divergent properties at particle coalescence and that it smoothly merges into the dipolar potential at $r = r_{\mathrm{c}}$. Furthermore, the angular variation of the UTP is less extreme than the real dipolar potential, which should lead to smoother estimates of the local energy at high tilt angles.

To optimise the pseudopotential we again calibrate in the two-body system. The $\cos 2\phi$ term in the potential couples together angular momentum channels of the wavefunction that differ by two angular momentum quanta, meaning that we can no longer solve the Schrödinger Equation separately in each angular momentum channel. Now that weight will be passed between the channels, they need to be considered explicitly and simultaneously.

Figure 2.10: The equation of state of the tilted dipolar gas system as a function of tilt angle θ. Our DMC data using the dipolar potential and UTP overlie one another to within the width of the plotted lines, with stochastic error bars of order $10^{-5} E_\mathrm{F}$. First-order perturbation theory $E^{(1)}$ is shown in blue.
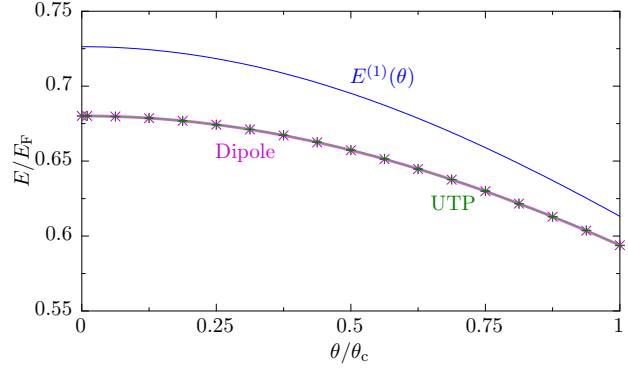
We solve the Schrödinger Equation simultaneously in the lowest four occupied angular momentum channels, $\ell = \{1, 3, 5, 7\}$, numerically for both the dipolar potential and, separately, using the pseudopotential, in order to find values for the coefficients $\{v_i\}$. As part of this process we optimise the weight in each channel. Unlike in the $\theta = 0$ case it is not possible to find an analytic scattering wavefunction in the two-body homogeneous system that correctly captures the physics of the system in any limit. Instead we optimise the parameters $\{v_i\}$ by matching the energy of two particles in an harmonic trap, in effect minimising the error that was shown in Fig. 2.4.

We need to select an optimal trap frequency ω at which to calibrate the pseudopotential. To do this, we re-write the reduced system Hamiltonian for particles in an harmonic trap as $\hat{H} = \hat{H}_\mathrm{iso}(\hat{r}) + \hat{H}_\mathrm{aniso}(\hat{r}, \hat{\phi})$, with

$$\hat{H}_\mathrm{iso}(\hat{r}) = -\nabla^2 + \frac{1}{4}\omega^2 \hat{r}^2 + \frac{\bar{d}^2}{\hat{r}^3},$$

$$\hat{H}_\mathrm{aniso}(\hat{r}, \hat{\phi}) = -\frac{\bar{d}^2}{\hat{r}^3} \frac{\frac{3}{2}\sin^2\theta}{1 - \frac{3}{2}\sin^2\theta} \cos 2\hat{\phi},$$

and $\bar{d}^2 = d^2(1 - \frac{3}{2}\sin^2\theta)$. $\hat{H}_\mathrm{iso}$ captures the effect of the harmonic trap and the isotropic part of the dipolar interaction, whilst $\hat{H}_\mathrm{aniso}$ captures the anisotropic part of the dipolar interaction. We seek a trap frequency ω at which the average kinetic energy of the harmonic trap system is the same as that of the homogeneous system, allowing us to select the appropriate Fermi momentum k_F to describe the interaction strength $k_\mathrm{F} r_0$. For the isotropic part of the Hamiltonian we can apply a cusp correction to the non-interacting harmonic trap wavefunction, in the same spirit as
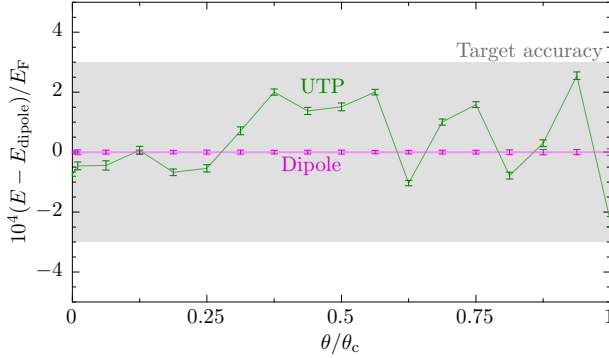
Figure 2.11: The deviation of the equation of state as calculated using the tilted pseudopotential from that calculated using the exact dipolar potential. Results using the dipolar potential are shown in magenta, with those using UTP pseudopotential in green. Similarly to Fig. 2.8, the grey box around the results using the dipolar potential shows the targeted $3 \times 10^{-4} E_{\mathrm{F}}$ accuracy level.

Section 2.2. This gives a trial wavefunction

$$\psi(r, \phi) \propto \omega\, r\, \mathrm{e}^{-\frac{1}{4}\omega r^2 - 2\frac{d}{\sqrt{r}}}.$$

We set the average kinetic energy of the isotropic harmonic trap system as equal to the kinetic energy of the homogeneous system and solve for ω, which for interaction strength $k_{\mathrm{F}} r_0 = 1/2$ is $\omega_{\mathrm{iso}} \approx 2.2 E_{\mathrm{F}}$.

Having analysed the isotropic part of the Hamiltonian we now turn to the anisotropic $\hat{H}_{\mathrm{aniso}}$. As there is no analytical solution to the tilted two-body scattering problem available we instead perform a perturbative analysis in small θ. We search for the most important contribution that $\hat{H}_{\mathrm{aniso}}$ makes to the system's energy, which occurs where $|\psi(r, \phi)\hat{H}_{\mathrm{aniso}}\psi(r, \phi)|$ is maximal. This is at $r \approx r_0$ and $\phi = 0$, and using these values in the functional form of $\hat{H}_{\mathrm{aniso}}$ we get a perturbative energy $\frac{3}{2}r_0^{-2}\sin^2\theta\left(1 - \frac{9}{4}\sin^4\theta\right)$ for small θ. Adding this to the isotropic trap frequency we obtain the harmonic trap frequency $\omega \approx 2.2 E_{\mathrm{F}} + \frac{3}{2}r_0^{-2}\sin^2\theta\left(1 - \frac{9}{4}\sin^4\theta\right)$, which we use to optimise the pseudopotentials. An example UTP is shown in Fig. 2.9, demonstrating its smooth and non-divergent properties. The form of the pseudopotential is robust against changes in the trap frequency ω used to construct it. With the pseudopotential in place we perform DMC calculations to evaluate the ground state energy of the anisotropic, homogeneous dipolar gas. In Fig. 2.10 we show the equation of state of the tilted dipole gas at interaction strength $k_{\mathrm{F}} r_0 = 1/2$ over a range of tilt angles $0 \leq \theta \leq \theta_{\mathrm{c}}$ away from vertical. We use a similar trial wavefunction to

the non-tilted case, with the addition to the Jastrow factor of an anisotropic term

$$\prod_{i \neq j} \exp \left[\left(\sum_{k=0}^{N_{\text{s}}} s_k r_{ij}^k \cos\left(2\phi_{ij}\right) \right) \left(1 - \frac{r_{ij}}{L} \right)^3 \Theta(L - r_{ij}) \right],$$

where the variables have the same meaning as in Eq. (2.7), ϕ_{ij} is the polar angle between the particles labelled i, j, and $N_{\text{s}} = 6$. This term captures the leading-order anisotropies in the inter-particle correlations. The addition of higher-order angular terms did not provide any significant benefit. In calculations using the real tilted dipolar potential we also modify the cusp condition to the form $\prod_{i>j} \exp(-2\bar{d}/\sqrt{r_{ij}})$.

In Fig. 2.10 we compare our DMC estimates of the equation of state to first-order perturbation theory [48]

$$E^{(1)}(\theta) = \frac{E_{\text{F}}}{2} \left[1 + \frac{128}{45\pi} k_{\text{F}} r_0 \left(1 - \frac{3}{2} \sin^2 \theta \right) \right].$$

Similarly to the non-tilted case we find that perturbation theory overestimates the energy, and also that it overestimates the reduction in energy with increasing tilt angle. Again the results using the exact dipolar interaction and those using our UTP are so similar they cannot be distinguished on this scale, and so we analyse the pseudopotential accuracy by examining the energy error from the dipolar potential in Fig. 2.11. As in the non-tilted system the pseudopotential achieves our target accuracy of $3 \times 10^{-4} E_{\text{F}}$ across a wide range of parameter space. The pseudopotential is particularly accurate below $\theta \lesssim \theta_{\text{c}}/4$ where there is less coupling between angular momentum channels, at $\theta \to 0$ reproducing the same accuracy that was found in the non-tilted system.

To determine the full benefit of using the pseudopotential in a tilted system we examine the behaviour of the calculated energy with DMC timestep in Fig. 2.12, evaluated at $k_{\text{F}} r_0 = 1/2$ and $\theta = \theta_c/2$. Similarly to the non-tilted case, Fig. 2.12(a) shows that the energy calculated using the pseudopotential has significantly improved behaviour with timestep when compared to the dipolar potential, having less severe variation of the energy with timestep and also remaining in the linear regime out to larger τ. There is also a reduction in standard error of ~ 2.2 times when using the pseudopotential, as seen in Fig. 2.12(b). Combining the fitting parameters in Fig. 2.12 in the way set out in Section 2.5.1 shows the pseudopotential
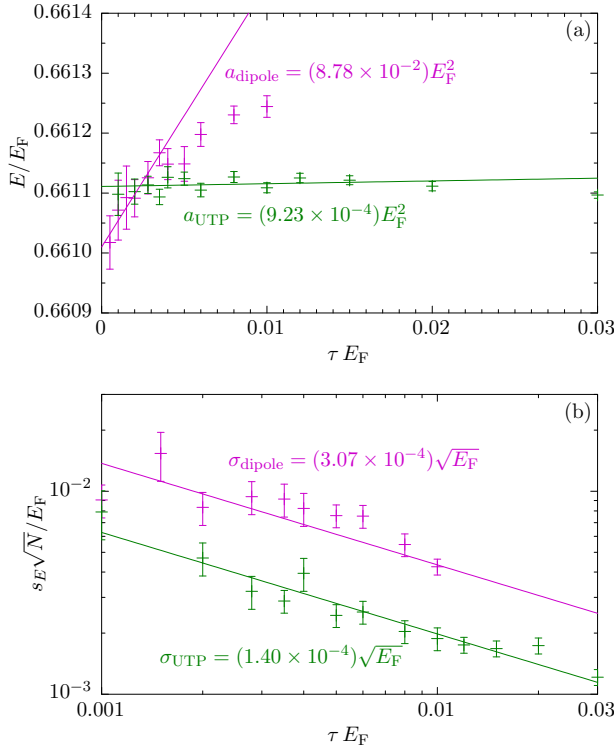
Figure 2.12: (a) The variation of the energy per particle in the Fermi gas of tilted dipoles with timestep τ, with the values of the linear error parameters a. (b) The standard error s_E in the energy per particle in the Fermi gas, again with fitted $1/\tau$ parameters given.

to be ~ 450 times quicker to use than the real tilted dipolar interaction.

We have constructed pseudopotentials for the dipolar interaction at tilt angles $0 \leq \theta \leq \theta_c$, and shown that they give the ground state energy of the anisotropic, homogeneous dipolar gas to within $3 \times 10^{-4} E_F$, and also provide a 450-times speedup over using the real tilted dipolar interaction. This means that they will be an accurate and efficacious tool to carry out DMC investigations of the whole $0 \leq \theta \leq \theta_c$ phase diagram.

2.7   Discussion

We have developed accurate pseudopotentials for the dipolar interaction in two dimensions and tested them against the dipolar interaction by comparing scattering phase shifts, energies in an harmonic trap, and the ground state of a Fermi gas. The pseudopotentials deliver ground state energies of the Fermi gas to an accuracy of $3 \times 10^{-4} E_F$, and their smoothness accelerates DMC calculations by a factor of up to ~ 2000.

The pseudopotentials have been constructed to work in situations where the dipole moments are aligned both normal and at an angle to the two-dimensional plane of motion of the particles. This could allow the formalism developed here to be used in an analysis of the full phase diagram of the 2D dipolar gas, including investigating the high interaction strength regime where the Fermi fluid forms a Wigner-type crystal [60], possibly after passing through a stripe phase [48], or to turn to the tilted section of the phase diagram, with the possibility of superfluid behaviour at high tilt angles [90]. Superfluidity is also expected in a system of dipoles dressed by an external microwave field [91, 92], a system that would also be amenable to analysis using a pseudopotential. The method used here for constructing pseudopotentials for the tilted system could also be extended to a 3D system of dipolar particles, or to study a classical analogue of the system.

Data used for this Chapter are available online [93].

Chapter 3

Pseudopotential for the two-dimensional contact interaction

We propose a smooth pseudopotential for the contact interaction acting between ultracold atoms confined to two dimensions. The pseudopotential reproduces the scattering properties of the repulsive contact interaction up to 200 times more accurately than a hard disk potential, and in the attractive branch gives a 10-fold improvement in accuracy over the square well potential. Furthermore, the potential enables diffusion Monte Carlo simulations of the ultracold gas to be run 15 times quicker than was previously possible.

3.1   Introduction

Many collective quantum phenomena emerge from reduced dimensionality, including the quantum Hall effect [94], high-temperature superconductivity [95], quantum magnetism [96], and topological insulators [97]. Consequently, two-dimensional (2D) systems have recently attracted a great deal of attention [82, 98–103]. 2D systems may now be realised, for example, at the interface between two solids [104], or in an ultracold atomic gas in an anisotropic optical trap, with one dimension tightly confined relative to the other two [105–107]. This coincidence of novel many-body phenomena with accurate experimental realisations makes 2D systems attractive for numerical investigation.

Ultracold atoms provide a clean model Hamiltonian with a tunable interaction strength, and their study has delivered new insights into many-body quantum physics [108–111]. The resonant Feshbach interaction between ultracold atoms (as discussed in Section 1.2.3) is usually modelled by a contact potential [20–28]. Despite its widespread usage, the contact interaction causes sampling problems in numerical simulations due to its infinitesimally short range and divergence at coalescence. It also harbours a bound state, complicating the use of ground state methods for examining repulsive scattering between particles. These difficulties are conventionally circumvented by replacing the contact potential by, for example, a hard disk potential, which we show leads to inaccurate scattering properties. This problem has recently been resolved in three dimensions by Bugnion *et al.* with the development of a smooth pseudopotential [61] that results in a hundred-fold increase in the accuracy of the scattering properties. The smoothness of the new pseudopotential formalism also radically speeds up numerical calculations [62], as seen in Chapter 2. Here we follow that prescription to develop a pseudopotential that improves the modelling of 2D quantum gases with a contact interaction.

In Section 3.2 we discuss two particles interacting via the 2D contact potential. In Section 3.3 we derive the pseudopotential, and in Section 3.4 demonstrate its accuracy in an inhomogeneous two-body system. In Section 3.5 we examine the pseudopotential's advantages over other methods in a homogeneous many-body system, before discussing potential future applications of the pseudopotential in Section 3.6.

3.2 Analytical results

In order to develop a pseudopotential for use in many-body simulations, it is essential to first understand the behaviour of the two-particle system. Here we analyse an isolated two-body system of distinguishable fermions, starting with non-interacting particles and then adding a short-ranged interaction potential, which not only allows us to find solutions for the contact interaction, but also serves as a platform from which to propose a pseudopotential. Atomic units ($\hbar = m = 1$) are used throughout, and anticipating that we will study many-body systems, we measure energies in units of the Fermi energy E_F and lengths in units of the Fermi length k_F^{-1}.

3.2.1 Short-ranged two-particle interactions

We consider two equal-mass, distinguishable fermions in a vacuum. In their centre-of-mass frame, the Schrödinger Equation for particles interacting via a potential $V(r)$ is given by

$$-\nabla^2 \psi(r, \theta) + V(r)\psi(r, \theta) = E\psi(r, \theta), \tag{3.1}$$

where E is the energy in the centre-of-mass frame.

The analytic solution to Eq. (3.1) for non-interacting particles ($V(r) = 0$) in a vacuum takes the form

$$\psi_\ell(r, \theta) = R_\ell(r)\Theta_\ell(\theta)$$

with

$$\Theta_\ell(\theta) = \frac{1}{\sqrt{2\pi}}\mathrm{e}^{i\ell\theta},$$
$$R_\ell(r) = \mathcal{A}(k)J_\ell(kr) + \mathcal{B}(k)Y_\ell(kr),$$

where $k = \sqrt{E}$ is the wavevector in the centre-of-mass frame, ℓ is angular momentum projected onto the normal to the 2D plane, and $\mathcal{A}(k)$ and $\mathcal{B}(k)$ are constants set by the boundary conditions. $J_\ell(kr)$ and $Y_\ell(kr)$ are Bessel functions of the first and second kinds, respectively.

If we take the potential $V(r)$ to be short ranged and cylindrically symmetric, for

distinguishable fermions the only effect of the potential is in the $\ell = 0$ channel. The wavefunction beyond the interaction range, where $V(r) = 0$, then takes the same form as in the non-interacting case,

$$\psi_0(r) \propto \mathcal{A}(k)J_0(kr) + \mathcal{B}(k)Y_0(kr). \tag{3.2}$$

There are two branches of solutions, scattering states for $E > 0$ and bound states for $E < 0$.

Scattering states ($E > 0$)

For two-particle scattering with positive E, the non-interacting wavefunction given by Eq. (3.2) with $k = \sqrt{E}$ can be written at large separations in the oscillatory form

$$\psi_{\rm s}(r) \propto \frac{\sin\left(kr + \frac{\pi}{4} + \delta(k)\right)}{\sqrt{kr}}, \tag{3.3}$$

where the scattering phase shift $\delta(k)$, given by

$$\cot \delta = -\mathcal{A}(k)/\mathcal{B}(k), \tag{3.4}$$

describes the large radius behaviour of the wavefunction and captures the full impact of the scattering interaction.

Bound states ($E < 0$)

Two particles with $E < 0$ are in a bound state in which they remain in close proximity if no external force is applied. The bound state wavefunction has the form

$$\psi_{\rm b}(r) \propto \mathcal{A}(\kappa)J_0(i\kappa r) + \mathcal{B}(\kappa)Y_0(i\kappa r),$$

where $\kappa = \sqrt{-E}$. For the wavefunction to be normalisable $\mathcal{A}$ and $\mathcal{B}$ must satisfy $\mathcal{B}(\kappa)/\mathcal{A}(\kappa) = i$, and therefore the wavefunction

$$\begin{aligned}\psi_{\rm b}(r) &\propto J_0(i\kappa r) + iY_0(i\kappa r) \\ &\propto H_0^{(1)}(i\kappa r),\end{aligned} \tag{3.5}$$

where $H_0^{(1)}(x) = J_0(x) + iY_0(x)$ is the Hankel function of the first kind. Note that $H_0^{(1)}(i\kappa r) \to \mathrm{e}^{-\kappa r}/\sqrt{\kappa r}$ as $\kappa r \to \infty$, with the expected exponential decay of a bound state.

3.2.2 2D contact interaction

We now apply these results for short-ranged 2D interactions to the 2D contact interaction $V^{\mathrm{cont}}(r)$. In a fermionic system this zero-ranged interaction acts only between distinguishable particles, with the interaction strength described by a scattering length a. We can capture the full effect of the interaction by imposing the boundary condition [113, 114]

$$\left(r\frac{\mathrm{d}}{\mathrm{d}r} - \frac{1}{\ln(r/a)} \right) \psi(r) = 0 \tag{3.6}$$

at $r = 0$ and then at $r > 0$ use the non-interacting solution Eq. (3.2), which gives

$$\psi_0^{\mathrm{cont}}(r) \propto J_0(kr) - \frac{\pi}{2[\gamma + \ln(ka/2)]} Y_0(kr), \tag{3.7}$$

where $\gamma \approx 0.577$ is Euler's constant.

For $E > 0$ the scattering phase shift is evaluated using Eq. (3.4) as

$$\cot \delta^{\mathrm{cont}}(k) = \frac{2}{\pi} \left[\gamma + \ln(ka/2)\right]. \tag{3.8}$$

The pseudopotential must be able to reproduce this phase shift as a function of scattering wavevector.

For $E < 0$ the bound state wavefunction is given by Eq. (3.5). The corresponding bound state energy can be found from the condition $\mathcal{B}/\mathcal{A} = i$ and Eq. (3.7) as

$$E_{\mathrm{b}} = -\frac{4}{a^2}\mathrm{e}^{-2\gamma}.$$

Examples of a scattering and bound state wavefunction are shown in Fig. 3.1. At large radii the scattering state wavefunction takes the form of a wave, with the first node occurring at $r = a$ in the $k \to 0$ limit, whilst the bound state wavefunction decays exponentially. Both wavefunctions diverge at particle coalescence, which makes them difficult to sample in numerical methods. This motivates us to
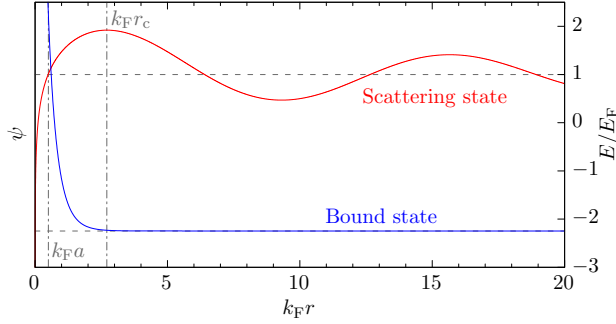
Figure 3.1: The bound (blue) and scattering (red) state wavefunctions of the contact interaction with $k_F a = 1/2$. The wavefunctions are offset by their energies, $E_s = E_F$ for the scattering state and $E_b = -\frac{4}{a^2} \exp(-2\gamma)$ for the bound state. The radius r_c gives the position of the first antinode in the scattering state, which is used as the cutoff radius for the pseudopotentials.

develop a smooth pseudopotential for the contact interaction, which will give rise to a wavefunction that is easier to sample numerically.

3.3 Derivation of the pseudopotentials

To develop smooth pseudopotentials for the contact interaction we continue to investigate the two-particle system in a vacuum, where the particles are distinguishable fermions and an analytical solution exists. We first focus on scattering states where, after reviewing the hard and soft disk potentials that are commonly used in ultracold atomic gas calculations, we construct a pseudopotential using the method proposed by Troullier and Martins (TM) [115]. This method was originally developed for making pseudopotentials for electron-ion interactions, but has been successfully applied to other systems of interacting particles [61, 112]. Next we construct another, "ultratransferable", pseudopotential (UTP) following the method in Ref. [61], as also used in Chapter 2. We then compare the accuracy of the TM and UTP pseudopotentials with that of the hard and soft disk potentials. Finally, we develop pseudopotentials for bound states. We have made the software used to generate all the pseudopotentials in this work available online [116].

3.3.1 Pseudopotentials for scattering states

Hard disk potential

Here we briefly review the hard disk potential that is currently used in many numerical studies of the contact interaction [20, 27, 82]. The interaction potential has the form

$$V^{\text{HD}}(r) = \begin{cases} \infty, & r \leq R, \\ 0, & r > R, \end{cases}$$

where R is the radius of the potential. Solving the Schrödinger Eq. (3.1) with a boundary condition $\psi_0^{\text{HD}}(R) = 0$, the wavefunction is given by

$$\psi_0^{\text{HD}}(r) \propto \begin{cases} 0, & r \leq R, \\ -Y_0(kR)J_0(kr) + J_0(kR)Y_0(kr), & r > R, \end{cases}$$

and the scattering phase shift defined by Eq. (3.4) is

$$\begin{aligned} \cot \delta^{\text{HD}}(k) &= \frac{Y_0(kR)}{J_0(kR)} \\ &= \frac{2}{\pi}[\gamma + \ln(kR/2)] + \frac{(kR)^2}{2\pi} + \mathcal{O}\big((kR)^4\big). \end{aligned} \qquad (3.9)$$

By setting the hard disk radius R equal to the scattering length a, the low energy scattering phase shift from the hard disk has the same form as the phase shift from the contact potential in Eq. (3.8). A hard disk potential with $R = a$ then gives the phase shift for the contact interaction with an error of order $\mathcal{O}((ka)^2)$, delivering the correct scattering properties only in the $k \to 0$ limit. An example of a hard disk potential is shown in Fig. 3.2.

Soft disk potential

To reduce the error in the scattering phase shift at finite k from that found with the hard disk, we may instead use a soft disk potential [117]

$$V^{\mathrm{SD}}(r) = \begin{cases} U, & r \le R, \\ 0, & r > R, \end{cases}$$

where U is the height of the soft disk potential. The extra degree of freedom in this potential relative to the hard disk allows it to remove the error in the scattering phase shift in Eq. (3.9) of $(kR)^2/2\pi$, and so describe the scattering correct to $\mathcal{O}((ka)^4)$. We solve the Schrödinger Equation using this potential separately in the regions $r < R$ and $r > R$, enforcing continuity of the wavefunction and its derivative at $r = R$, and expanding the scattering phase shift Eq. (3.4) to second order around $k = 0$. Setting the first term equal to the contact potential scattering phase shift of Eq. (3.8) relates R and the scattering length a via

$$R = a_{\mathrm{SD}} = a \exp\left(\frac{I_0(\chi)}{\chi I_1(\chi)}\right),$$

where $I_\ell(\chi)$ is the modified Bessel function of the first kind, and the factor $\chi^2 = UR^2 \approx 3.57$ is obtained by setting the second order term in the phase shift expansion to zero. This uniquely specifies a soft disk potential for a given a, whose scattering properties are correct up to order $\mathcal{O}((ka)^4)$. An example of a soft disk potential is shown in Fig. 3.2. It has a larger radius R than the hard disk potential but a lower height U, with the width tending to zero and the height to infinity as the scattering length goes to zero.

Troullier–Martins pseudopotential

The previous subsections showed that the hard and soft disk potentials give accurate scattering properties only in the limit of $k \to 0$. However a Fermi gas contains all the scattering wavevectors in the range $0 < k \le k_{\mathrm{F}}$, and so the hard and soft disk potentials will give rise to inaccurate results. To demonstrate how the accuracy may be improved at finite k, we develop pseudopotentials using the TM formalism [61, 115]. This formalism produces scattering state pseudopotentials that

Figure 3.2: Scattering state pseu-
dopotentials $V(r)$ for the contact
potential with $k_F a = 1/2$. The
pseudopotential for the hard disc
with radius a is shown in cyan, the
soft disk with radius a_{SD} in blue,
the TM pseudopotentials in red and
green, and the UTP in magenta.
The pseudopotential cutoff radius r_c
is the same as in Fig. 3.1.
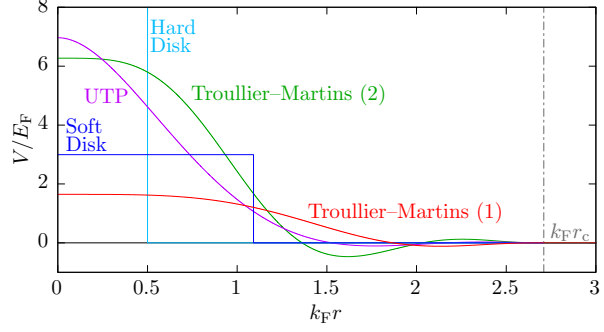
1. should reproduce the phase shift of the contact potential accurately for all scattering wavevectors in the Fermi sea;

2. are smooth everywhere, which accelerates numerical calculations; and

3. for repulsive interactions do not support a bound state.

This formalism requires two prescribed parameters, namely the calibration wavevector k_c at which the resulting pseudo-wavefunction has identical scattering properties to the contact potential, and a cutoff radius r_c at which the pseudopotential smoothly becomes zero.

The calibration wavevector must be chosen for each system. For example, in a superfluid we might choose $k_c = k_F$, as that is where the most important physics of Cooper pair formation occurs. For a fermionic gas we choose $k_c = k_F/2$, which minimises the average phase shift error (see also Chapter 2.

By choosing the cutoff radius to be larger than the radius of the first node in the analytic wavefunction, which is at $r \approx a$ in Fig. 3.1, we ensure that the pseudo-wavefunction does not contain the innermost node that corresponds to the bound state of the contact interaction [61]. In order to avoid unnecessarily removing scattering states from the potential the cutoff radius must also be smaller than the radius of the second node, and so we choose the cutoff radius to be at the first antinode of the wavefunction with $k = k_c$, shown in Fig. 3.1.

The TM pseudopotential takes the form

$$V^{\text{TM}}(r) = \begin{cases} k_c^2 + p'' + p'^2 + \frac{p'}{r}, & r \le r_c, \\ 0, & r > r_c, \end{cases}$$
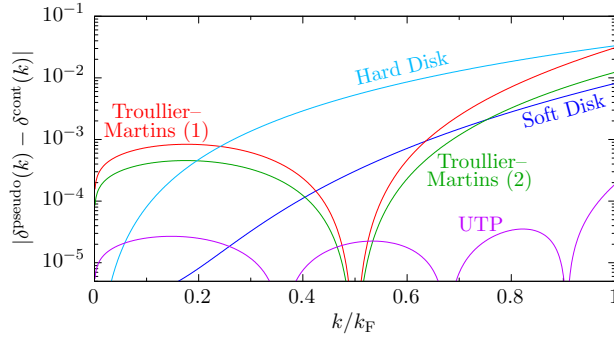
Figure 3.3: The error in the scattering phase shift $|\delta^{\mathrm{pseudo}}(k) - \delta^{\mathrm{cont}}(k)|$ as a function of scattering wavevector for the different pseudopotentials at $k_{\mathrm{F}}a = 1/2$. The error from the hard disk is shown in cyan, the error from the soft disk in blue, the errors from the two TM pseudopotentials in red and green, and the error from the UTP in magenta.

where the polynomial $p(r) = \sum_{i=0}^{6} c_i r^{2i}$, and primes indicate derivatives with respect to r. The coefficients $\{c_i\}$ are determined by a set of constraints on the pseudopotential and pseudo-wavefunction, whose form is $\psi(r) = \exp[p(r)]$: that the pseudo-wavefunction is smooth up to the fourth derivative at r_{c}; that the pseudopotential has zero curvature at the origin; and that the norm of the pseudo-wavefunction within r_{c} equals that of the wavefunction from the real contact potential [61, 115], as in Chapter 2. This gives rise to a set of coupled equations for the $\{c_i\}$ of which one is quadratic and the others linear: there are therefore two separate branches of solutions, which give rise to two separate TM pseudopotentials.

In Fig. 3.2 we compare all of the discussed pseudopotentials for the contact interaction, with $k_{\mathrm{F}}a = 1/2$. The TM pseudopotentials, being everywhere smooth and finite, are easier to work with numerically than the hard and soft disks, and they do not introduce discontinuities in the first derivative of the wavefunction. The potential labelled Troullier–Martins (1) in Fig. 3.2 is smaller than Troullier–Martins (2) at particle coalescence, but larger at further separations to give similar average scattering.

Errors in scattering phase shift

The quality of a pseudopotential for scattering states may be determined by how accurately it reproduces the phase shift of the contact potential. All information on the difference between the pseudopotential and contact potential can be obtained from the wavefunction just beyond the edge of the pseudopotential. We match the analytical pseudo-wavefunction that solves Eq. (3.1), ψ, and its first derivative to the non-interacting solution Eq. (3.2) at a radius R_{e} beyond the radius of the

pseudopotential. This leads to an expression for the scattering phase shift

$$\cot \delta(k) = \frac{\frac{\psi'(R_\mathrm{e})}{\psi(R_\mathrm{e})} Y_0(kR_\mathrm{e}) + kY_1(kR_\mathrm{e})}{\frac{\psi'(R_\mathrm{e})}{\psi(R_\mathrm{e})} J_0(kR_\mathrm{e}) + kJ_1(kR_\mathrm{e})}.$$

We calculate the difference in the phase shift between the contact interaction and pseudopotentials, showing the error in the calculated phase shifts from using the pseudopotentials $|\delta^\mathrm{pseudo}(k) - \delta^\mathrm{cont}(k)|$ in Fig. 3.3, with $R_\mathrm{e} = r_\mathrm{c}$. The hard and soft disk potentials are exact in the limit of $k \to 0$, but deviate away from that point, with the soft disk performing better than the hard disk. The TM (1) pseudopotential is on average around twice as accurate as the hard disk potential, with the TM (2) pseudopotential being around twice as accurate again, and the soft disk being another 1.3 times more accurate. Both TM pseudopotentials capture the scattering behaviour perfectly at $k_\mathrm{c} = k_\mathrm{F}/2$ but deviate at all other scattering wavevectors, which is a consequence of the norm-conserving condition on the pseudo-wavefunctions. To further improve the accuracy of the pseudopotentials, a natural extension to the formalism is to construct a pseudopotential that minimises this deviation in the phase shift over all wavevectors $k \leq k_\mathrm{F}$. We propose such a pseudopotential here, referring to it as an "ultratransferable pseudopotential" (UTP) [61].

Ultratransferable pseudopotential

Similarly to the TM pseudopotential, the UTP takes a polynomial form within a cutoff radius r_c,

$$V^\mathrm{UTP}(r) = \begin{cases} \left(1 - \frac{r}{r_\mathrm{c}}\right)^2 \left[u_1\left(1 + \frac{2r}{r_\mathrm{c}}\right) + \sum_{i=2}^{N_u} u_i \left(\frac{r}{r_\mathrm{c}}\right)^i \right], & r \leq r_\mathrm{c}, \\ 0, & r > r_\mathrm{c}, \end{cases}$$

with $N_u = 3$. The term $(1 - r/r_\mathrm{c})^2$ ensures that the pseudopotential goes smoothly to zero at $r = r_\mathrm{c}$, and the component $u_1(1 + 2r/r_\mathrm{c})$ constrains the pseudopotential to have zero derivative at the origin. This ensures that the pseudo-wavefunction is smooth, easing the application of numerical methods.

To determine the coefficients $\{u_i\}$ we numerically solve the scattering problem,

extract the scattering phase shift $\delta^{\text{UTP}}(k)$, and then minimise the total squared error in the phase shift over all scattering wavevectors k,

$$\langle\left|\delta^{\text{UTP}}(k)-\delta^{\text{cont}}(k)\right|^2\rangle = \int_0^{k_{\text{F}}}\left|\delta^{\text{UTP}}(k)-\delta^{\text{cont}}(k)\right|^2 g(k/k_{\text{F}})\mathrm{d}k,$$

where the weighting is given by the density of states in the centre of mass frame $g(k) = k(4 - \frac{8}{\pi}[k\sqrt{1-k^2}+\arcsin(k)])$, as in Chapter 2. An example UTP is shown in Fig. 3.2, confirming that this construction gives smooth potentials. The scattering phase shift error from the UTP is shown in Fig. 3.3, demonstrating that the UTP construction creates pseudopotentials that are significantly more accurate than the Troullier–Martins pseudopotentials and soft disk potential, and some 200 times more accurate than the hard disk. This is achieved by the phase shift error from the UTP being optimised to be zero at three different wavevectors, as opposed to the single wavevector for the TM pseudopotentials.

3.3.2   Pseudopotentials for bound states

Pseudopotentials may also be constructed for particles in a bound state, with $E < 0$. In order to accurately imitate the contact potential, the pseudopotentials must reproduce the bound state energy of the contact potential $E_{\text{b}} = -(4/a^2)\exp(-2\gamma)$, and also must accommodate only one bound state. We first discuss the square well pseudopotential, which has been used in previous ultracold atomic gas calculations, and then again develop smooth pseudopotentials using the TM formalism. For bound states there is no quantity like the scattering phase shift that can be used to directly determine the quality of the pseudopotentials. We therefore demonstrate their accuracy in a two-body inhomogeneous system in Section 3.4.

Square well potential

The square well potential has the form

$$V^{\text{SW}}(r) = \begin{cases} -U, & r \leq R, \\ 0, & r > R. \end{cases}$$

This potential may be made arbitrarily close to the bound state contact interaction by taking the well radius $R \to 0$ and depth $U \to \infty$. Decreasing R, however, reduces the sampling efficiency and thereby increases the computational cost. We require R to be less than the average interparticle separation $\sim 1/k_{\mathrm{F}}$, in order to avoid the unphysical situation of three or more particles interacting simultaneously. In Section 3.4 we investigate the R dependence of the accuracy of the square well pseudopotential.

Because there is no analogue of the scattering phase shift for the bound system it is not possible to uniquely define a U and R for a given a, as we did for the soft disk potential in which U and R were related by the second order term in the expansion. However one parameter may be determined by ensuring that the bound state energy of the potential is E_{b}, and for a given R the value of U this sets can be found as a solution to

$$\frac{-J_0(k_1 R)}{k_1 J_1(k_1 R)} = \frac{J_0(ik_2 R) - iY_0(-ik_2 R)}{k_2\left(-iJ_1(ik_2 R) + Y_1(-ik_2 R)\right)},$$

where $k_1 = \sqrt{U - |E_{\mathrm{b}}|}$ and $k_2 = \sqrt{|E_{\mathrm{b}}|}$. An example of a square well potential is shown in Fig. 3.4. Except in the limit of being infinitely deep and narrow, the square well potential does not give rise to the same wavefunction as the true contact interaction, but within the potential the wavefunction and therefore probability density is too small. This means that in the presence of an external potential (for example an harmonic trap, as in Section 3.4) there is too much weight at large particle separations, giving rise to inaccurate values of the system's energy. As $R \to 0$ the wavefunction approaches the exact form given by Eq. (3.5).

Troullier–Martins pseudopotential

The Troullier–Martins pseudopotential resolves the problem of having too much weight at large particle separations by being a norm-conserving pseudopotential, and so has the correct amount of weight within and outside of its cutoff radius. The construction of the TM pseudopotential for the bound state is identical to that of the scattering state, except that the calibration energy is now given by the bound state energy $E_{\mathrm{c}} = E_{\mathrm{b}}$. The cutoff radius r_{c} should be kept smaller than the average interparticle separation $\sim 1/k_{\mathrm{F}}$ to reduce the probability of three or more particles
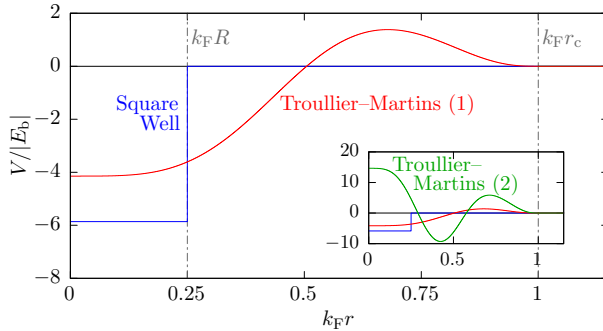
Figure 3.4: Bound state pseudopotentials for the contact potential with $k_\mathrm{F} a = 1/2$. A square well with $k_\mathrm{F} R = 1/4$ is shown in blue, and the TM (1) pseudopotentials with $k_\mathrm{F} r_\mathrm{c} = 1$ is shown in red. Inset: the TM (2) pseudopotential, shown in green and with $k_\mathrm{F} r_\mathrm{c} = 1$, behaves qualitatively differently near particle coalescence.

interacting at once, but there is no lower bound on r_c: similarly to the case of the square well, reducing r_c increases the accuracy but also the computational cost of simulations. The square well and TM pseudopotentials are shown in Fig. 3.4.

One of the TM pseudopotentials, labelled (1) in Fig. 3.4, behaves as would be expected qualitatively for a short-ranged potential giving rise to a bound state: it has a large negative region near particle coalescence. The other TM solution, labelled (2) and shown in the inset to Fig. 3.4, does not show this behaviour, instead having an attractive region at finite particle separation. This will give rise to a non-zero expected separation between bound particles, which is physically discordant with the contact interaction. We therefore reject the TM (2) pseudopotential because of its unphysical behaviour and select the TM (1) pseudopotential instead, referring to it henceforth simply as the TM pseudopotential.

Since all particles in bound states have approximately the same energy, the UTP formalism does not offer any advantage in this system. We now move on to testing the pseudopotentials in an inhomogeneous two-body system.

3.4   Two fermions in an harmonic trap

We have constructed pseudopotentials that describe the scattering behaviour of two isolated fermions. To test the pseudopotentials we turn to the experimentally realisable [76, 118] system of two distinguishable fermions in a circular harmonic trapping potential $\frac{1}{4}\omega^2 r^2$ of frequency ω. This system also has the advantage of being analytically soluble, which provides a stringent test for the pseudopotentials that we will use in many-body simulations.

Figure 3.5: Analytic energy levels for two particles in an harmonic trap as a function of the dimensionless interaction strength $g = -1/\ln(a/d)$. The excited states (solid lines) correspond to the scattering states of the contact potential and the ground state (dashed line) corresponds to the bound state. The non-interacting energies are shown by circles along the line $g = 0$.
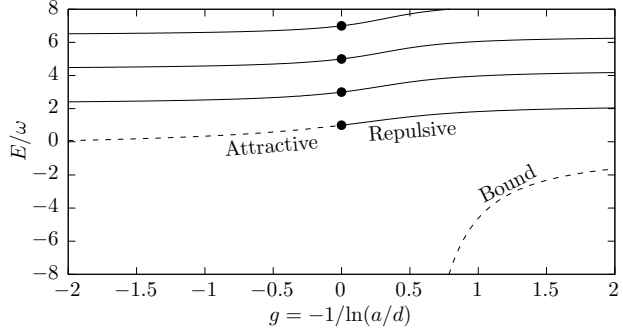
3.4.1 Analytic energy levels

In the centre-of-mass frame the Schrödinger Equation for two distinguishable fermions in an harmonic trap is given by

$$-\nabla^2 \psi(r) + \frac{1}{4}\omega^2 r^2 \psi(r) + V^{\mathrm{cont}}(r)\psi(r) = E\psi(r)$$

where the interparticle interaction term $V^{\mathrm{cont}}(r)\psi$ can be replaced by a boundary condition given by Eq. (3.6). For the contact interaction the energy levels in the centre-of-mass frame are solutions to the nonlinear equation [113, 119]

$$\Psi\left(-\frac{E}{2\omega} + \frac{1}{2}\right) = \ln\left(\frac{d^2}{a^2}\mathrm{e}^{-2\gamma}\right),\tag{3.10}$$

where $d = \sqrt{2/\omega}$ is the characteristic length scale of the trap and Ψ is the digamma function. These solutions are shown in Fig. 3.5 as a function of the dimensionless interaction strength $g = -1/\ln(a/d)$. In the non-interacting case $g = a = 0$ the energies have the expected values $E = \omega(2n+1)$ for non-interacting particles. As the repulsive interaction strength $g > 0$ in Fig. 3.5 increases, the energy increases and at $g \to \infty$ joins onto the energy of the attractive branch at $g \to -\infty$, in an analogue of unitarity in the BEC-BCS crossover [120]. The bound state of the contact potential survives in this inhomogeneous system as the deep bound state at $g > 0$.
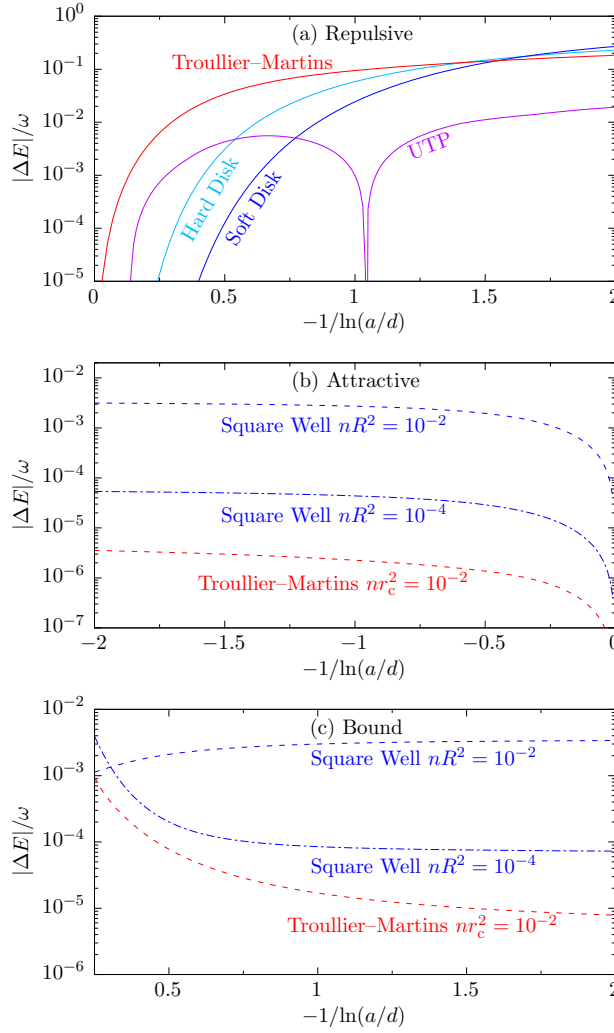
Figure 3.6: Error in the centre-of-mass energy of two fermions in an harmonic trap calculated using pseudopotentials from the analytic value of the energy from Eq. (3.10). (a) Error in the centre-of-mass energy of particles with a repulsive interaction as a function of interaction strength for the hard disk in cyan, the soft disk in blue, the TM pseudopotential in red, and the UTP in magenta. (b) Error in the centre-of-mass energy of particles with a weakly attractive interaction as a function of interaction strength. The square well pseudopotentials have radii given by $nR^2 = 10^{-4}$ and $nR^2 = 10^{-2}$, and the TM pseudopotential has a cutoff radius given by $nr_c^2 = 10^{-2}$, with the different cutoff radii denoted by different types of line dashing. (c) Error in the bound state energy as a function of interaction strength.

3.4.2 Accuracy of the pseudopotentials

We compare the estimates of the centre-of-mass energies of two particles in an harmonic trap to the analytic result in: Fig. 3.6(a), for repulsive interactions; Fig. 3.6(b) for attractive interactions; and Fig. 3.6(c) for bound particles.

In the repulsive case, we find that the hard and soft disk potentials and TM pseudopotential are accurate at small interaction strengths, but at large interaction strengths the error in the calculated energies is greater than 10%. The UTP pseudopotential is around 10 times more accurate at high interaction strengths, and becomes exact in the non-interacting limit.

To choose the radii of the potentials for the attractive and bound branches we

follow the approach used in Ref. [61] and use a TM pseudopotential with a cutoff radius of $nr_c^2 = 10^{-2}$, where $n = \omega/2\pi$ is the peak density of two non-interacting particles in the trap. We compare this to square wells with radii given by the same $nR^2 = 10^{-2}$ and the smaller $nR^2 = 10^{-4}$ [21, 61]. We note that in both the attractive and bound branches, reducing the well radius increases the accuracy of the square well potential, but that the TM pseudopotential gives up to 10 times higher accuracy than a square well with a radius 1/10 the size. The ability to use a larger cutoff radius with the TM pseudopotential brings significant benefits in numerical sampling of the potential, with the sampling efficiency expected to scale as $\sim r_c^2$. The increased accuracy can be related to the fact that the square well gives rise to wavefunctions with too much weight at large particle separations, raising the energy in the external trap, whilst the TM pseudopotential is norm-conserving, having the correct weight in the wavefunction outside r_c. The norm-conservation condition ensures that the TM pseudopotential gives a bound state wavefunction that is robust against changes in the local environment, and hence performs well in the spatially varying harmonic trap. As opposed to the single calibration energy of the TM pseudopotential, in constructing the UTP we would average over a range of energies. This would offer no advantage in the attractive and bound branches, where there is a definite binding energy for the pair of particles, and so we do not examine the UTP in these branches.

We have shown that for particles in an harmonic trap with attractive interactions, the TM pseudopotential gives an increase in both accuracy and sampling efficiency relative to the square well potential. For two particles with repulsive interactions, the use of a UTP can offer a 10-fold increase in accuracy relative to using the TM pseudopotential or hard or soft disk potentials. We now go on to demonstrate the scaling benefits of the UTP in a many-body simulation.

3.5   Fermi gas

Having demonstrated the effectiveness of the UTP for studying the two body scattering problem and two distinguishable fermions in an harmonic trap, we now demonstrate the advantages of the UTP in a prototypical setting: a two-dimensional homogeneous Fermi gas. Such a system serves as a benchmark for cold atom experiments [121, 122] and also as a model for electrons in conductors.

We focus on the repulsive branch of the contact interaction. Here the hard and soft disk potentials are uniquely defined for a given interaction strength, and may not be improved to attain arbitrarily high accuracy, as is possible in the attractive and bound branches by reducing the well radius to zero. This allows us to demonstrate the intrinsic benefits of the UTP formalism over the hard and soft disk potentials.

The smoothness of the UTP relative to the hard and soft disk potentials will be reflected in the many-body wavefunction, which will make it easy to work with numerically. Having shown in Section 3.4 that the UTP is more accurate than the competing hard and soft disk potentials and Troullier–Martins pseudopotential, we proceed here to verify the accuracy of the UTP by comparing the energy of a Fermi gas with first- and second-order perturbation theory calculations [123–125].

3.5.1   Formalism

To calculate the ground state energies we use the diffusion Monte Carlo (DMC) technique. DMC is a highly-accurate Green's function projector method for determining ground state energies and expectation values [37, 126, 127], and it is well-suited to investigating homogeneous gaseous phases. We use the CASINO implementation [65] of the DMC method with a Slater–Jastrow trial wavefunction $\Psi = \mathrm{e}^J D_\uparrow D_\downarrow$, where $D_\uparrow$ ($D_\downarrow$) is a Slater determinant of plane-wave states for the spin up (down) channel. The Jastrow factor e^J describes correlations between particles, with

$$J = \sum_{\substack{j \neq i \\ \alpha, \beta \in \{\uparrow, \downarrow\}}} \left(1 - \frac{r_{ij}}{L_{\mathrm{c}}}\right)^3 u_{\alpha\beta}\left(r_{ij}\right) \Theta\left(L_{\mathrm{c}} - r_{ij}\right), \tag{3.11}$$

where $r_{ij} = |\mathbf{r}_i - \mathbf{r}_j|$ is the distance between two particles with labels i and j, and $u_{\alpha\beta}$ are eighth-order polynomials, whose parameters are optimised using variational Monte Carlo subject to the symmetry requirements $u_{\uparrow\uparrow} = u_{\downarrow\downarrow}$ and $u_{\uparrow\downarrow} = u_{\downarrow\uparrow}$. L_{c} is a cutoff length that we set equal to the radius of a circle inscribed within the simulation cell, and Θ is the Heaviside step function.

We calculate the ground state energy expectation value for 49 spin-up and 49 spin-down particles in a homogeneous two-dimensional system for increasing interaction strengths $-1/\ln(k_{\mathrm{F}}a)$ up to a maximum value of 1.8 before the system would phase separate into a fully polarised state. To accurately capture the hard disk
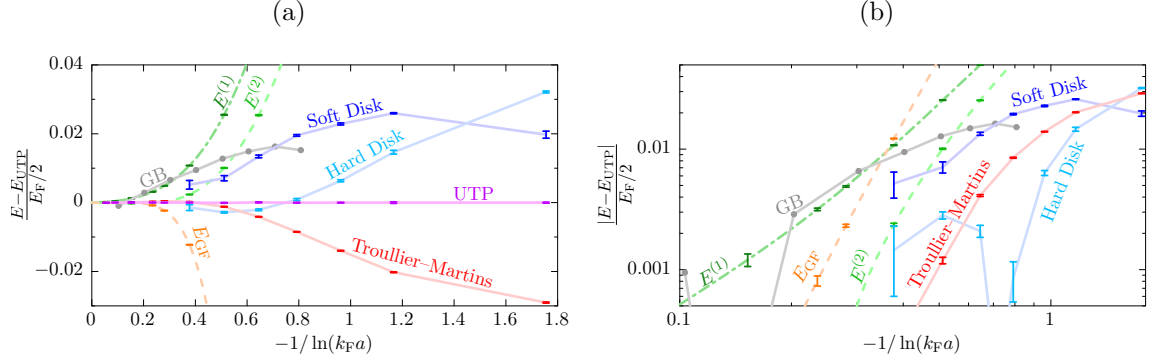
Figure 3.7: (a) Differences in ground state energy from the result obtained with the UTP as a function of interaction strength, normalised by the energy of the non-interacting system. The green lines denoted $E^{(1)}$ and $E^{(2)}$ are predictions from first- and second-order perturbation theory [123–125] and E_{GF} is the result of a Galitskii-Feynman partial resummation of Feynman diagrams reported in Ref. [125], shown in orange. GB is the Monte Carlo result from Ref. [27], calculated using a hard disk potential and shown in grey, and our results using the hard disk are shown in cyan, the soft disk in blue, the TM pseudopotential in red, and the UTP in magenta. (b) The same results on a logarithmic scale.

wavefunction at small inter-particle distances in our DMC simulations we add an additional term to the Jastrow factor in Eq. (3.11),

$$
u_{\mathrm{H}}(r) = \begin{cases} -\infty, & r \leq R, \\ \ln[\tanh(\frac{r/R-1}{1-r/L_{\mathrm{c}}})], & R < r < L_{\mathrm{c}}, \\ 0, & r \geq L_{\mathrm{c}}, \end{cases} \tag{3.12}
$$

as in Ref. [82], where R is the hard disk radius. In the present study the additional term applies to opposite spins only.

We extrapolate to zero DMC timestep to obtain accurate ground state energies. For each data point we run three simulations with timesteps $0.25dt, 0.5dt, dt$, [83] with dt the maximum timestep in the linear regime, and extrapolate to zero timestep by minimising the weighted least squares fit. All error bars represent the DMC stochastic error combined with the concomitant uncertainty in the timestep extrapolation. We expect that the use of a quadratic DMC algorithm would give similar results [86, 87].

3.5.2   Results

In Fig. 3.7 we compare ground state energies of the Fermi gas obtained using the different potentials. It is clear that for $-1/\ln(k_{\mathrm{F}}a) > 0.7$ both the hard and soft disk potentials, as well as the Troullier–Martins pseudopotential, are insufficient to obtain the desired $10^{-4}E_{\mathrm{F}}$ accuracy that has been obtained in other DMC studies of homogeneous systems [61, 62, 79, 112].

To verify the DMC results we compare our estimates for the ground state energy with perturbation theory [123–125]. As can be seen in Fig. 3.7(b), first order perturbation theory $E^{(1)} = \frac{E_{\mathrm{F}}}{2}(1 + [-1/\ln(k_{\mathrm{F}}a)])$ deviates quadratically in the interaction strength $-1/\ln(k_{\mathrm{F}}a)$ from the UTP result as expected, and second order perturbation theory

$$E^{(2)} = \frac{E_{\mathrm{F}}}{2}\left[1 + \left(\frac{-1}{\ln(k_{\mathrm{F}}a)}\right) + \left(\frac{3}{4} - \ln(4\mathrm{e}^{-\gamma})\right)\left(\frac{-1}{\ln(k_{\mathrm{F}}a)}\right)^2\right]$$

deviates cubically in $-1/\ln(k_{\mathrm{F}}a)$ and outperforms first order perturbation theory. In Fig. 3.7 we also show the result obtained in Ref. [125] using a partial resummation of Feynman diagrams in the Galitskii-Feynman (GF) scheme which is correct to order $\mathcal{O}\left([-1/\ln(k_{\mathrm{F}}a)]^3\right)$, and note that this indeed deviates cubically in interaction strength from the UTP result. The agreement of the scaling behaviour of the energy calculated using the UTP with interaction strength when compared to these analytic results confirms the accuracy of the UTP.

In addition to the analytic approximations, we compare our DMC results with an independent study using the hard disk potential and the same number of particles in Ref. [27], labelled GB. We note that their predicted energies are higher than those from our DMC calculations using the hard disk potential, and as DMC is a variational method this indicates that our trial wavefunction is likely more accurate than was available to the author of Ref. [27], possibly due to our inclusion of a Jastrow factor with variational parameters.

Having confirmed the accuracy of the UTP we now examine its performance benefits. The local energy, $E_{\mathrm{L}} = \Psi^{-1}\hat{H}\Psi$, is a crucial quantity in DMC calculations [65]. The stochastic error in a DMC calculation is proportional to the standard deviation σ_{L} in the local energy distribution, and therefore a smoother local energy will give rise to more accurate results for the same computation time. Fig. 3.8 shows

Figure 3.8: Standard deviation of the local energy distribution of the trial wavefunction. The hard and soft disk pseudopotentials exhibit a larger standard deviation, due to the sudden changes in energy when two particles approach one another.
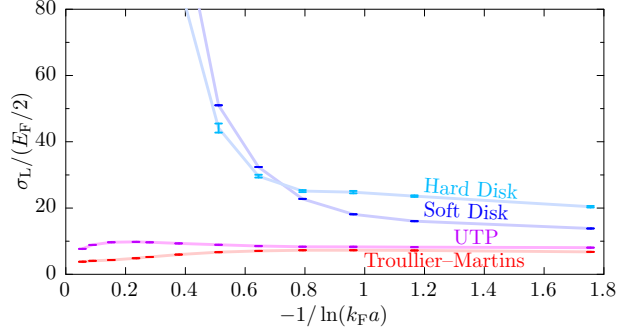
the standard deviation of the local energy distribution of the trial wave function when using all of our pseudopotentials. Both the UTP and TM pseudopotentials benefit from their smoothness in obtaining a lower local energy standard deviation compared to the hard and soft disk potentials. For weak interactions the hard disk potential benefits from an additional Jastrow factor term, Eq. (3.12), relative to the soft disk potential, whose height U also diverges as $a \to 0$. However for larger interactions the soft disk potential results in a smoother wavefunction than the hard disk potential and therefore has lower local energy variance. The variance in the local energies diverges for the hard and soft disk potentials for weak interactions, whereas it decays for the UTP and TM pseudopotentials. The standard deviation for the TM pseudopotential is slightly lower than the UTP at all interaction strengths, which is understood from the larger size of the potential for the UTP in Fig. 3.2 compared to the TM pseudopotential. This behaviour is similar to the 3D case reported in Ref. [61].

The reduced variance in the local energy lowers the computational effort T required for a DMC calculation, which scales as $T \propto \sigma_L^2/dt$ [62, 128], as seen in Chapter 2. From Fig. 3.8 we see that at intermediate interaction strength $-1/\ln(k_F a) = 0.8$ the variance of the local energy for the UTP is 2.7 and 3.0 times lower than for the soft and hard disk potentials respectively, corresponding to a speedup of 7.5 and 9.1.

In addition to the lower local energy variance, our pseudopotentials offer an additional speedup. The DMC estimate of the energy must be extrapolated to zero timestep, and the larger the region of linear dependence of energy on timestep, the larger timestep can be used. This reduces computational effort even further, as $T \propto 1/dt$. In Fig. 3.9 we observe that the extent of the linear regime of the error in ground
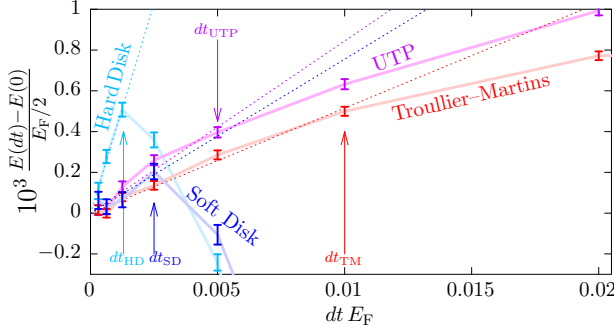
Figure 3.9: Error in the estimated ground state energy as a function of DMC timestep. The results using the hard disk are shown in cyan, the soft disk in blue, the TM potential in red and the UTP in magenta, with solid lines indicating the values calculated using DMC and dotted lines a linear extrapolation. This enables the identification of when the error leaves the linear regime.

state energy with timestep differs between the pseudopotentials: it extends up to $dt_{\text{HD}} = 1.25 \times 10^{-3}/E_{\text{F}}$ for the hard disk, up to $dt_{\text{SD}} = 2.5 \times 10^{-3}/E_{\text{F}}$ for the soft disk, up to $dt_{\text{UTP}} = 5.0 \times 10^{-3}/E_{\text{F}}$ for the UTP, and up to $dt_{\text{TM}} = 1.0 \times 10^{-2}/E_{\text{F}}$ for the TM pseudopotential. This means that the maximum timestep for a calculation with the UTP is two and four times larger than for the soft and hard disk potentials respectively. Combining this with the reduced variance we therefore accomplish a total speedup of at least 15 times by using the UTP instead of the hard and soft disks.

To summarise, we have demonstrated the importance of using a pseudopotential with scattering properties that accurately describe the contact interaction. For weak interactions we observe that a divergence in the variance in the local energy severely constrains the accuracy of DMC simulations with soft or hard disk potentials. At strong interactions these inaccurate potentials introduce a significant bias into the results, such that we were unable to attain the $10^{-4}E_{\text{F}}$ target accuracy in the ground state energy. However the UTP delivers highly accurate results over the full range of interaction strengths and additionally offers 15 times better computational performance. We therefore recommend the UTP as an accurate and efficacious tool for studying the contact interaction in 2D.

3.6 Discussion

We have developed a high-accuracy pseudopotential for the contact interaction in 2D, building on the work of Ref. [61]. We have demonstrated that our ultratrans-

ferable pseudopotential provides accurate scattering phase shifts, accurate energies for two harmonically confined particles, and we have demonstrated its advantages in many-body simulations. The energies obtained with our UTP are over 10 times more accurate in the repulsive branch of the interaction than is afforded by the hard and soft disk potentials used in recent studies. Moreover, we have demonstrated that for many-body systems our pseudopotential delivers a speedup of at least 15 times in diffusion Monte Carlo computations, on top of the more accurate result.

The performance and ease of construction of the pseudopotential suggests that it could be widely applicable across first-principles methods beyond quantum Monte Carlo. The pseudopotential formalism has already been used to study the Coulomb [62] and dipolar [112] interactions. Although in this work we have focused on using the pseudopotential to accurately capture the scattering properties of the contact interaction, our formalism allows the further improvement of modelling of quantum gases by calibrating the pseudopotentials to more accurately describe the scattering properties of the underlying Feshbach resonance interaction. To next lowest order in scattering wavevector, this corresponds to including the effective range term essential for describing narrow Feshbach resonances, which may exhibit exotic breached superfluidity [129, 130], or other interactions with non-zero effective ranges, which are applicable in the study of nucleon reactions [131]. Rather than a description in terms of the scattering phase shift, the pseudopotentials could instead be calibrated to other scattering properties. For example, they could be calibrated to the cross-section for elastic scattering measured experimentally via the thermalisation rate, or the inelastic loss coefficient, to capture the full physical interaction between particles [19].

Data used for this Chapter are available online [132].

Chapter 4

Jastrow correlation factor for periodic systems

We propose a Jastrow factor for electron-electron correlations that interpolates between the radial symmetry of the Coulomb interaction at short inter-particle distance and the space-group symmetry of the simulation cell at large separation. The proposed Jastrow factor captures comparable levels of the correlation energy to current formalisms, is 40% quicker to evaluate, and offers benefits in ease of use, as we demonstrate in quantum Monte Carlo simulations.

4.1   Introduction

Quantum Monte Carlo (QMC) is a prominent family of techniques for studying strong correlations in quantum many-body systems [37]. In particular, the variational and diffusion Monte Carlo methods (VMC and DMC) are accurate tools for studying ground-state energies and expectation values. Both methods are predicated on the use of a trial wavefunction, whose similarity to the true ground state determines the accuracy and efficiency of the calculations [40], as discussed in Chapter 1. It is therefore important to have access to a high fidelity trial wavefunction.

A common foundation for constructing a fermionic trial wavefunction is to begin with the Hartree–Fock wavefunction $\Psi_{\mathrm{HF}} = D_\uparrow D_\downarrow$, where $D_\uparrow$ ($D_\downarrow$) is a Slater determinant of single-electron states for the up (down) spin species. The Slater determinants encode the fermionic antisymmetry of the trial wavefunction, ensuring Pauli exchange is satisfied, but do not include any effects of electron correlation. To describe such correlations, we modify the trial wavefunction to be of the Slater–Jastrow [39] form $\Psi = \mathrm{e}^{J(\mathbf{R})} D_\uparrow D_\downarrow$, where $\mathrm{e}^{J(\mathbf{R})}$ is a Jastrow factor that is a function of all the electron positions, $\mathbf{R}$. For real $J(\mathbf{R})$ the Jastrow factor is positive definite, and hence does not modify the nodal structure of the Hartree–Fock wavefunction.

In order to allow the Jastrow factor to accurately describe the correlations in a particular system of interest, $J(\mathbf{R})$ depends on a number of variational parameters [80, 133–139]. These parameters can be optimised using the relatively inexpensive VMC method, and then the optimal trial wavefunction used as the starting point for a more accurate but more expensive DMC calculation. In principle the DMC estimate of the energy depends only on the nodal surface of the trial wavefunction [140], but in practice a more accurate trial wavefunction with an optimised Jastrow factor allows the method to proceed more efficiently.

In this Chapter we consider Jastrow factors for infinite, periodic systems. These systems are amenable to numerical simulation through the use of finite simulation cells which are tessellated, with periodic boundary conditions, to fill all of space. Jastrow factors in the literature tend to either respect the short range radial symmetry of the Coulomb interaction, or abide by the symmetry of the simulation cells, but not both [80, 133–135]. Here we propose a Jastrow factor that interpolates between these symmetries; is easier to use than current Jastrow factors by virtue of having a single parameter that tunes its accuracy, as opposed to two such parameters

for other Jastrow factors of similar accuracy; requires fewer variational parameters to reach comparable accuracy; and is 40% quicker to evaluate than these current Jastrow factors.

All of our QMC simulations were performed using the CASINO package [65], and we use Hartree atomic units throughout this Chapter. In Section 4.2 we review common Jastrow factors from the literature, and then show how our proposed Jastrow factor fits into this hierarchy. In Section 4.3 and Section 4.4 we examine the accuracy and efficiency of the Jastrow factors in the homogeneous electron gas and crystalline beryllium, respectively, before drawing our conclusions in Section 4.5.

4.2   Jastrow factor

We are concerned with Jastrow factors that capture correlation between electrons, and hence include functions of electron-electron separation,

$$J(\mathbf{R}) = \sum_{\substack{j > i \\ \sigma,\tau \in \{\uparrow,\downarrow\}}} J_{\sigma\tau}(\mathbf{r}_{ij}),$$

where $\mathbf{r}_{ij} = \mathbf{r}_i - \mathbf{r}_j$, the sum runs over all electrons labelled i, j, and we refer to $J_{\sigma\tau}(\mathbf{r}_{ij})$ as a Jastrow function. The Jastrow function contains variational parameters that we optimise within a VMC calculation to minimise the variance in the local energy [141].

There are some fundamental constraints on the form of the Jastrow function. Firstly, in order to retain the spin expectation value of the Hartree–Fock wavefunction $J_{\sigma\tau}(\mathbf{r}_{ij})$ must be even under exchange of particles. Secondly, in order to avoid non-physical divergences in the local energy, $J_{\sigma\tau}(\mathbf{r}_{ij})$ must be at least twice-differentiable everywhere except at particle coalescence ($\mathbf{r}_{ij} = \mathbf{0}$).

However, at particle coalescence the Coulombic potential energy of two electrons diverges. In order to retain a non-divergent local energy the kinetic energy therefore has to diverge in the opposite direction at particle coalescence. This may be achieved by imposing the Kato cusp conditions [66] on the wavefunction, which may be

expressed as

$$\left.\frac{\partial J_{\sigma\tau}}{\partial r_{ij}}\right|_{r_{ij}=0} = \Gamma_{\sigma\tau},$$

giving spherically-symmetric behaviour at short radius $J_{\sigma\tau}(\mathbf{r}_{ij}) = \Gamma_{\sigma\tau} r_{ij} + \ldots$, where, for 3D systems, $\Gamma_{\uparrow\uparrow} = \Gamma_{\downarrow\downarrow} = \frac{1}{4}$ and $\Gamma_{\uparrow\downarrow} = \Gamma_{\downarrow\uparrow} = \frac{1}{2}$. The final constraint on the Jastrow factor is that, in periodic systems like those we consider here, $J_{\sigma\tau}(\mathbf{r}_{ij})$ must satisfy periodic boundary conditions at the edge of the simulation cell in order to tessellate space.

Before presenting and testing our proposal for a Jastrow factor, we first review other Jastrow factors that are commonly used in the literature. We organise the Jastrow factors by their symmetry, starting with a spherically symmetric function and then examining a Jastrow factor with the symmetry of the simulation cell before proposing our Jastrow factor that interpolates between these symmetries.

4.2.1   Term with spherical symmetry

The interaction between two isolated electrons is isotropic, and so it is reasonable to take the Jastrow factor as being spherically symmetric and purely a function of particle separation where two-body effects dominate, and especially at inter-particle separations shorter than the average nearest-neighbour separation in many-body systems. However, the simulation cells used in numerical calculations are not spherically symmetric as they have to tessellate to fill 3D space. Because of this requirement, and in order to limit the effect of otherwise infinite-ranged terms to within the simulation cell, radial terms in the Jastrow factor are cut off at a finite radius that is less than or equal to the Wigner–Seitz radius corresponding to the simulation cell. This is implemented by including a term $(1 - r_{ij}/L_{\sigma\tau})^C \Theta(L_{\sigma\tau} - r_{ij})$ in the Jastrow function, which goes to zero at a radius $L_{\sigma\tau}$, with $C - 1$ continuous derivatives. We take $C = 3$ in order to keep the local energy continuous at the cutoff radius [134]. $\Theta(L_{\sigma\tau} - r_{ij})$ is a Heaviside step function, which forces the Jastrow function to be zero everywhere beyond the radius $L_{\sigma\tau}$.

It has been found in the literature [80, 134, 142–144] that a Taylor expansion in electron-electron separation captures the most important short-ranged isotropic inter-particle correlations, and so here we review that expansion. Writing the Jas-

trow correlation function as a Taylor series around particle coalescence results in an expression

$$u_{\sigma\tau}(r_{ij}) = \left(\frac{L_{\sigma\tau}}{3} \left[\alpha_{1,\sigma\tau} - \Gamma_{\sigma\tau} \right] + \sum_{m=1}^{N_{\mathrm{u}}} \alpha_{m,\sigma\tau} r_{ij}^m \right) (1 - r_{ij}/L_{\sigma\tau})^3 \, \Theta \left(L_{\sigma\tau} - r_{ij} \right), \quad (4.1)$$

which is referred to as a u term [80, 134]. Here the N_{u} coefficients $\alpha_{m,\sigma\tau}$ are parameters that are optimised using VMC, and the cutoff length $L_{\sigma\tau}$ is also optimised variationally. The term $L_{\sigma\tau}[\alpha_{1,\sigma\tau} - \Gamma_{\sigma\tau}]/3$ ensures that the Kato cusp conditions are satisfied. Using a pseudopotential for the electron-electron interaction [62] would set $\Gamma_{\sigma\tau} = 0$.

The u term Jastrow function with parameters optimised for an homogeneous electron gas with $r_{\mathrm{s}} = 4$ is shown in Fig. 4.1a. The short-range behaviour of the u term is linear to satisfy the Kato cusp condition, and then at large separation the cutoff function limits the range of the u term to within the Wigner-Seitz radius of the simulation cell, shown as a grey arc in Fig. 4.1a. This not only limits the maximum range of the correlations that can be captured by the u term, but also prevents it from capturing correlations in the corners of the simulation cell.

4.2.2 Term with simulation cell symmetry

One method to extend the ability of the Jastrow factor to capture correlations over the whole simulation cell is to use a form of Jastrow factor that innately has the space-group symmetry of the simulation cell. A simple but effective example of a Jastrow function that has such symmetry is a plane-wave basis, which also explicitly ensures periodicity of the Jastrow function. The so-called p term takes the form [80, 134]

$$p_{\sigma\tau}(\mathbf{r}_{ij}) = \sum_{\ell=1}^{N_{\mathrm{P}}} a_{\ell,\sigma\tau} \sum_{\mathbf{G}_\ell^+} \cos(\mathbf{G}_\ell \cdot \mathbf{r}_{ij}). \quad (4.2)$$

Here the $\{\mathbf{G}_\ell\}$ are the reciprocal lattice vectors of the simulation cell that belong to the ℓth star of vectors equivalent under the full symmetry group of the simulation cell, sorted by increasing size of $|\mathbf{G}_\ell|$ (and in periodic systems not including the trivial vector $\mathbf{0}$); "+" means that if $\mathbf{G}_\ell$ is included in the sum, $-\mathbf{G}_\ell$ is excluded; and
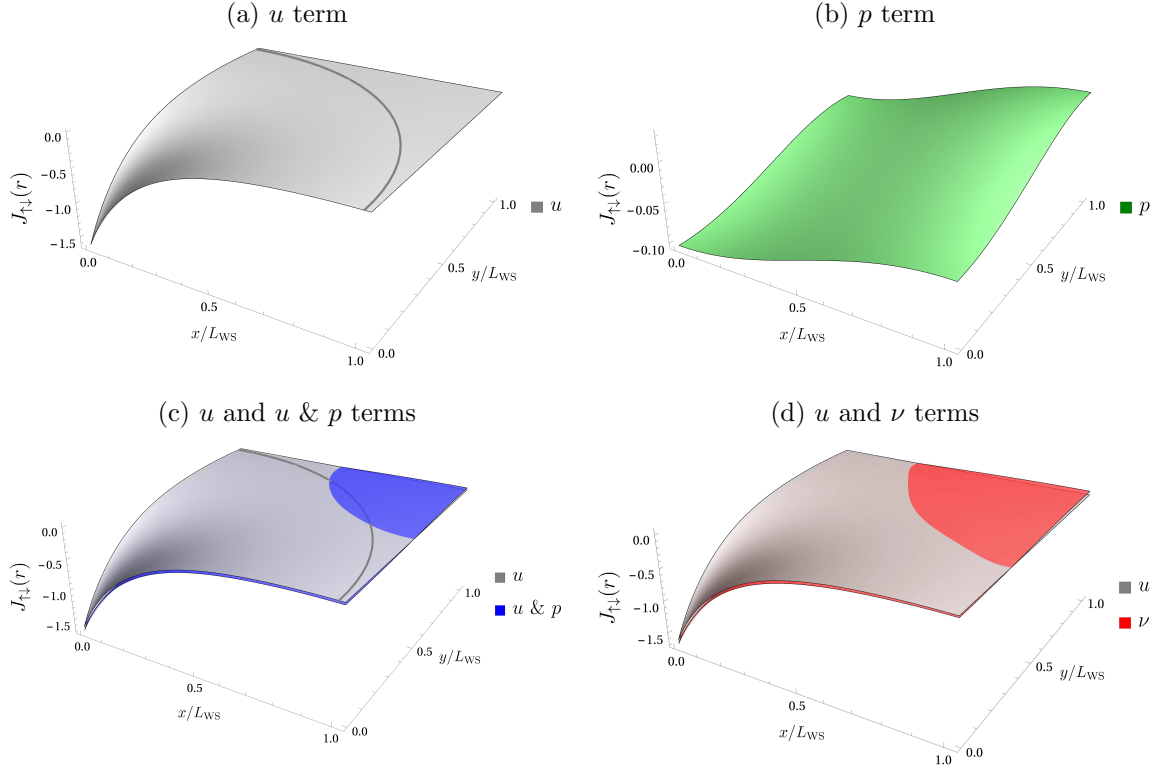
Figure 4.1: The Jastrow functions discussed in the main text, showing the (a) u, (b) p, (c) u (grey) and u & p (blue), and (d) u (grey) and ν (red) functions. The u, u & p, and ν terms each have a total of five variational parameters, optimised using VMC in the homogeneous electron gas system. The data are taken for an opposite-spin electron pair in the $z = 0$ plane, with one particle at the origin, showing one quadrant of the simulation cell. A grey arc indicates the u term's cutoff radius, which is comparable to the Wigner–Seitz radius L_{WS} of the simulation cell. We have subtracted a physically-irrelevant constant from the ν Jastrow function for clarity.

the $a_{\ell,\sigma\tau}$ are variational parameters, of which there are N_{p}.

A p term with $N_{\mathrm{p}} = 1$ for the homogeneous electron gas is shown in Fig. 4.1b. The p term exists over the whole simulation cell, including where the u term is cut off to zero. This means the p term can capture correlations in the cell corners that the u term misses. However, the p term does not tend to a radial form at short radius and so cannot satisfy the Kato cusp conditions at particle coalescence, meaning that on its own it does not make for an effective Jastrow factor. A common approach in the literature [79, 145–150], and also used in Chapter 2, is to combine both u and p terms to give a composite Jastrow function

$$J_{\sigma\tau}(\mathbf{r}_{ij}) = u_{\sigma\tau}(r_{ij}) + p_{\sigma\tau}(\mathbf{r}_{ij}), \tag{4.3}$$

which uses the u term to capture short-range correlations and the Kato cusp conditions, and the p term to capture long-range correlations in the corners of the simulation cell. We refer to such a combination as a u & p term.

An example of this composite Jastrow function, with $N_{\mathrm{u}} = 3$ and $N_{\mathrm{p}} = 1$ and parameters optimised in an homogeneous electron gas, is shown in Fig. 4.1c. As expected, the behaviour at short range is dominated by the u term. Yet at large radius this Jastrow function has structure due to the p term, including in the corner of the simulation cell outside the cutoff radius of the u term, shown by the grey arc, which allows the composite u & p term to capture longer-range correlations.

However, this construction has several undesirable features that limit its effectiveness at capturing inter-particle correlations. For a given amount of computing time to be spent optimising the parameters in the Jastrow factor, a choice needs to be made of the relative number of u and p terms to be used. We do not know a priori the optimal ratio of N_{u} to N_{p}, and so must explore a two-dimensional parameter space to determine it. A large proportion of the VMC calculation time is spent evaluating the Jastrow factor, and so it is important that the Jastrow factor is as simple as possible. But there is not equality of expense between the u and p terms, as sinusoidal p terms are more expensive to calculate than polynomial u terms, and the expense of a p term also increases with the number of elements of the reciprocal lattice vector stars used to evaluate it. Higher-order stars generally contain more elements than lower-order ones, meaning high-order p terms are even more expensive to calculate. To further complicate the optimisation of the u & p

term, although the p term was intended to capture longer-range correlations, it does also exist at short radius; this means it interferes with the effect of higher-order contributions from the u term.

One further problem with the form of Jastrow function given by Eq. (4.3) is that the cutoff length $L_{\sigma\tau}$ enters the expression non-linearly. To optimise the cutoff length and other parameters we need to solve a multi-dimensional non-linear set of equations, which is a significantly more difficult problem than solving a multi-dimensional linear set of equations, where the full force of linear algebra may be applied to increase the efficiency of the process [151].

We are interested in finding a form for the Jastrow factor that avoids these problems with the current method, by being a term with a single tuning parameter that determines the accuracy of the Jastrow factor, and which is also cheap to evaluate with linear coefficients. At the same time the proposed term should reproduce the advantageous properties of the u term, accurately capturing short-range correlations, and also the p term, exhibiting the symmetry of the simulation cell at large inter-particle separation.

4.2.3 ν term

We propose a Jastrow factor that combines the properties and symmetries of the u term at small radius with the properties and symmetries of the p term at large separation. The Jastrow function, referred to here as the ν term, is

$$\nu_{\sigma\tau}(\mathbf{r}_{ij}) = \sum_{n=1}^{N_\nu} c_{n,\sigma\tau} \left| f_x^2(\mathbf{x}_{ij}) + f_y^2(\mathbf{y}_{ij}) + f_z^2(\mathbf{z}_{ij}) \right|^{n/2},$$

$$f_x(\mathbf{x}) = |\mathbf{x}| \left(1 - \frac{|\mathbf{x}/L_x|^3}{4} \right), \tag{4.4}$$

where the N_ν parameters $c_{n,\sigma\tau}$ are optimised using VMC, and the length L_x is the width of the simulation cell in the Cartesian x-direction. In Section 4.4.1 below we generalise the ν term to non-cuboidal geometries.

At small radius, the function $f_x(\mathbf{x}) = |\mathbf{x}| + O\left(|\mathbf{x}|^4\right)$, and so $|f_x^2(\mathbf{x}) + f_y^2(\mathbf{y}) + f_z^2(\mathbf{z})|^{1/2} = r + O\left(r^4\right)$. This has the correct spherical symmetry to describe short-range electron-electron correlations, so at short radius the Jastrow function $\nu_{\sigma\tau}(\mathbf{r}_{ij}) = \sum_{n=1}^{N_\nu} c_{n,\sigma\tau} r_{ij}^n + \dots$ consists of an expansion in electron-electron separa-

tion, similarly to the u term. This means the ν term will reproduce the ability of the u term to capture short-ranged correlations and it is easy to satisfy the Kato cusp conditions by setting $c_{1,\sigma\tau} = \Gamma_{\sigma\tau}$.

The function $f(\mathbf{x})$ is symmetric under $\mathbf{x} \rightarrow -\mathbf{x}$, and automatically satisfies periodic boundary conditions at the edge of the simulation cell, with $f(L_{\mathrm{x}}\hat{\mathbf{x}}) \neq 0$, $f'(L_{\mathrm{x}}\hat{\mathbf{x}}) = 0$, and $f''(L_{\mathrm{x}}\hat{\mathbf{x}}) \neq 0$: this is achieved through the use of the cubic power in the definition of f, chosen by analogy to the cutoff function in the u term to distinguish long- and short-ranged components of the Jastrow function. Importantly, the f functions satisfying periodic boundary conditions means any function constructed from them, such as the ν term, will also correctly satisfy periodic boundary conditions. The scaling of the f functions in the different Cartesian directions lends the ν term the symmetry of the simulation cell at large inter-particle separation, and allows the ν term to capture long-range correlations, similarly to the p term. Not requiring a cut-off function also means all the variational parameters enter the expression for $\nu_{\sigma\tau}(\mathbf{r}_{ij})$ linearly, and so are easier to optimise than the equivalent number of variational parameters in the u term [151].

The ν Jastrow function optimised for a homogeneous electron gas is shown in Fig. 4.1d, demonstrating that it has the same small-radius behaviour as the u term. We can also see that the ν term still has structure in the corner of the simulation cell, similarly to the u & p term, which allows it to capture long-range inter-particle correlations. We will examine this similarity in more detail in a case study of the homogeneous electron gas in Section 4.3.

Freedom to optimise the behaviour of the Jastrow factor in the corners of the simulation cell also provides the freedom to change the kinetic energy of the wavefunction in the corners of the simulation cell, as $f''_{\mathrm{x}}(L_{\mathrm{x}}\hat{\mathbf{x}}) \neq 0$. This allows the ν Jastrow factor to more accurately respond to a finite and/or varying potential energy in the corners of the simulation cell. From a Thomas–Fermi perspective this provides the ν term with the freedom to counteract changes in the potential energy from interactions with kinetic energy in order to keep the total energy constant.

The ν term may also be adapted to systems other than the 3D ones considered here. For 2D systems the f_{z} function may simply be omitted; or for slab geometries, with two directions periodic and one non-periodic, f_{z} should be replaced by a function that reduces to $|\mathbf{z}|$ at short radius, for example $|\mathbf{z}|\mathrm{e}^{-(|\mathbf{z}|/L_{\mathrm{z}})^2}$.

In order to demonstrate the advantages of the ν Jastrow factor, in the next two

Sections we carry out simulations of the homogeneous electron gas and a crystalline solid. We examine the accuracy, efficiency, and ease of use of the ν Jastrow factor, and compare it with other forms of Jastrow factor used in the literature.

4.3   Homogeneous electron gas

For the first test of our Jastrow factor we examine the homogeneous electron gas (HEG). This system has been widely studied using QMC [126, 147, 152, 153] and serves as an analogue for electrons in a conductor. As it does not contain any atoms it allows us to focus on the electron-electron Jastrow factor. For simplicity we assume that the intra-species correlations for the up- and down-spin electrons are identical, and so fix $J_{\uparrow\uparrow} = J_{\downarrow\downarrow}$ and $J_{\uparrow\downarrow} = J_{\downarrow\uparrow}$.

We examine a HEG with density parameter $r_\mathrm{s} = 4$ in a cubic simulation cell subject to periodic boundary conditions, and use Slater determinants of plane wave orbitals. We use a system of 57 up- and 57 down-spin electrons, and confirmed that the main results of this section were reproduced in systems of 33 and 81 electrons per spin species and so are independent of system size. We optimise all the Jastrow factors by minimising the variance in the local energy [151, 154], and confirmed that minimising the energy directly [155] gave similar results. All VMC simulations are run for 1×10^6 steps. We then carry out DMC simulations to obtain a more accurate estimate for the energy within the fixed node approximation, E_{DMC}, which corresponds to the use of a perfect Jastrow factor. DMC simulations starting with different trial wavefunctions agree to within 5×10^{-6}a.u. To measure the accuracy of the Jastrow factors, we evaluate the percentage of the DMC correlation energy missing from the VMC simulation,

$$\eta = \frac{E_{\mathrm{VMC}} - E_{\mathrm{DMC}}}{E_{\mathrm{HF}} - E_{\mathrm{DMC}}} \times 100\%$$

where the Hartree–Fock energy E_{HF} is that obtained by using just the Slater determinant part of the wavefunction.

In Fig. 4.2a we compare the percentages of the correlation energy missing when the various Jastrow factors under scrutiny are used. The horizontal axis is labelled by the number of optimisable parameters per spin channel, N, for each Jastrow function: so, for example, a u term with a given number N of optimisable parameters

per spin channel has $N_{\mathrm{u}} = N-1$ optimisable parameters of terms in the inter-particle separation expansion, $\alpha_{m,\sigma\tau}$, as the cutoff length $L_{\sigma\tau}$ is also optimised. A u & p term with N_{p} optimisable parameters $a_{\ell,\sigma\tau}$ in the p part leaves $N_{\mathrm{u}} = N-1-N_{\mathrm{p}}$ optimisable parameters for the u term coefficients $\alpha_{m,\sigma\tau}$. For the ν term $N_\nu = N+1$, as the first coefficient $c_{1,\sigma\tau}$ is set by the Kato cusp conditions. The number of optimisable parameters N required to reach a converged accuracy is an important measure of the practicality of the Jastrow factors, as N governs the complexity of the variance minimisation procedure.

We observe that a u term alone can capture over 96% of the correlation energy missing from the Hartree–Fock ($N = 0$) result, converging when $N_{\mathrm{u}} \geq 3$ ($N \geq 4$). The addition of p terms improves this to only 2% of the correlation energy missing, as inter-particle correlations in the corners of the simulation cell are now captured. The number of p terms used (if greater than zero) makes a negligible difference to the percentage of the correlation energy captured, as long as there are also sufficiently many u terms present ($N_{\mathrm{u}} \geq 3$, for a total of $N \geq 5$). The smallest number of variational parameters required to achieve convergence is $N = 5$. It is important to capture all the short-ranged correlations at the centre of the cell, and it is also important to capture the leading long-range correlations that reflect the symmetry of the simulation cell. This motivates the construction of the ν term as being based around a short-ranged expansion in inter-particle separation that interpolates to the lowest-order symmetries of the simulation cell at long range.

The ν Jastrow factor reproduces the best u & p accuracy of $\eta = 2\%$ for $N \geq 4$. The need for only $N = 4$ optimisable parameters as opposed to the $N \geq 5$ required for the u & p terms means the ν term is easier to optimise. Furthermore, the ν term has a single parameter N_ν that can be increased to improve accuracy, as opposed to having to choose both N_{u} and N_{p} for the u & p term, which reduces the size of the parameter space that needs to be explored.

The ν term has captured all of the correlation energy available to the u & p terms in this system, but another important quantity in QMC methods is the variance in the estimate of the energy. The variance of the local energy determines the efficiency of DMC simulations [37, 83] and also acts as a proxy for the quality of trial wavefunctions, as the variance in the local energy of the exact ground state is zero. In Fig. 4.2b we examine the variances in the local energy using the different Jastrow factors relative to the variance using the Hartree–Fock wavefunction. Again

(a) Correlation energy missing   (b) Local energy variance
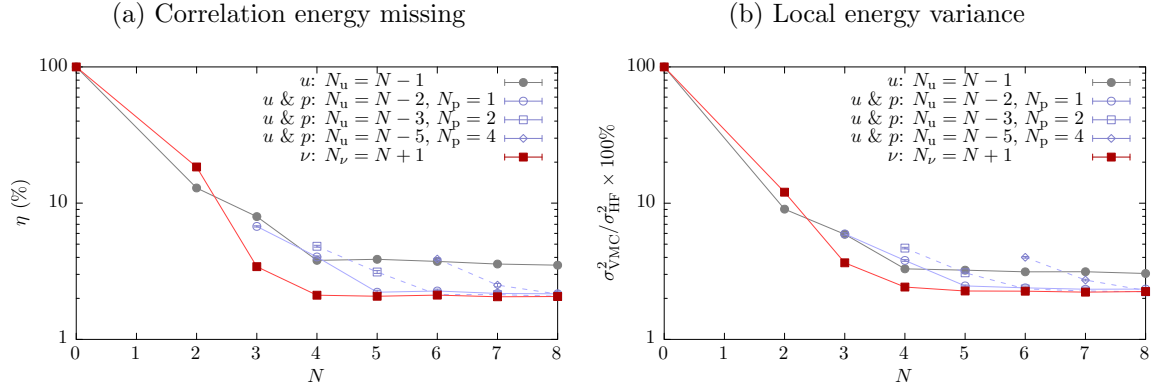
Figure 4.2: (a) The percentage of the DMC correlation energy missing from VMC simulations of the homogeneous electron gas, with N optimisable parameters in the Jastrow factor. Grey, blue, and red lines correspond to the u, u & p, and ν term respectively. (b) The variance in the local energy when using different Jastrow factors, as a percentage of the variance in the local energy using the Hartree–Fock wavefunction. Error bars, where not visible, are smaller than the size of the points.

the u term converges for $N \geq 4$, and the addition of p terms reduces the variance by another 33% if a good choice of N_{u} and N_{p} is made with $N \geq 5$. The ν term achieves the same reduction in the variance in the local energy as these more complicated terms but with fewer optimisable parameters, $N \geq 4$.

The similar levels of the correlation energy captured by the ν and u & p terms may be understood in terms of the correlations described by these Jastrow factors. In Fig. 4.3 we show the ν and $N_{\mathrm{p}} = 1$ u & p Jastrow functions with the u Jastrow function subtracted, to allow us to focus on the long-range correlations. Both Jastrow functions capture non-trivial correlations in the corner of the simulation cell, outside the radius where the u term is cut off to zero (shown by a grey arc), explaining their improved performance over the u term. Furthermore, the correlations captured by the ν and u & p terms are very similar, confirming that both are able to be optimised to capture all of the available correlation energy. The similarity of the ν and u & p terms also ensures that the zero-wavevector limits of their Fourier transforms are likewise similar, and hence that the finite-size errors from the Jastrow factors are comparable and can be dealt with following the same prescription [146, 156].

There is one further advantage to using the ν term in this system, rather than a

Figure 4.3: The $N = 5$ Jastrow functions with the u Jastrow function subtracted, to show how the Jastrow functions vary at large inter-particle separation.
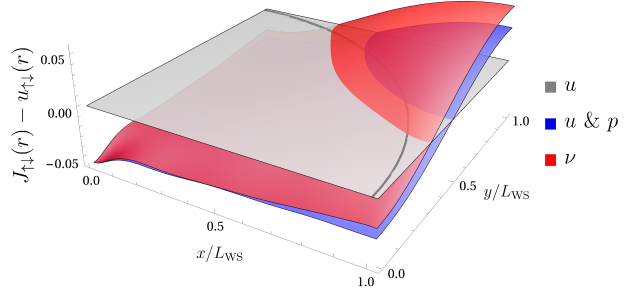
u & p term. The ν term is a polynomial expansion, like the u term, and this makes it quicker to evaluate than the p term with its sinusoids from each element of the stars of reciprocal lattice vectors. For $N = 5$, where both Jastrow factors have fully converged, the $N_{\mathrm{p}} = 1$ u & p term in the Jastrow factor is 61% slower to evaluate than the ν term, and the $N_{\mathrm{p}} = 2$ term takes over twice as long to evaluate as the ν term. This means that simulations with the ν term can be run significantly quicker than those with the u & p term, to obtain similar accuracy.

We have shown that the ν Jastrow factor captures the ground state energy of the HEG as well as a combination of the u and p terms, achieving the same accuracy and reduction in variance in the local energy. In addition to this, the ν term is easier to transfer between systems, as there is only one choice of parameter to make as opposed to two for the u & p term; the ν term requires $N = 4$ linear optimisable parameters to converge, rather than $N = 5$ non-linear parameters for the u & p term, making it cheaper to optimise; and the ν term is also quicker to evaluate. We now go on to test the ν Jastrow factor in an inhomogeneous periodic system, for which we take the example of crystalline beryllium.

4.4 Beryllium

To demonstrate that the advantages of the ν term are not restricted to simple homogeneous systems with cubic simulation cells, here we test it in a crystalline solid. As discussed in Section 4.2.3, the ν term is constructed to interpolate between the symmetry of the interaction potential (purely radial) at short radius and the simulation cell symmetry at large separation. In order to demonstrate the generality of this construction, we will focus on an analysis of a crystal with relatively low symmetry,

in the P6$_3$/mmc (hexagonal) space group, where it is non-trivial to construct the long-range form of the ν term. The simplest example of a stable crystal with this space group at zero temperature, where QMC is applicable, is crystalline beryllium, and so we use that as our example system. At the end of this Section we will also discuss results in higher-symmetry face-centred cubic (FCC) and body-centred cubic (BCC) crystals.

We model crystalline beryllium using an hexagonal simulation cell containing 32 atoms. The Be^{2+} ions are represented by pseudopotentials [65, 71, 134, 157], and the orbitals in the Slater determinants were obtained from a density functional theory [158, 159] (DFT) calculation using the CASTEP code with a plane-wave basis set [160, 161], converted to B-spline functions [162, 163].

The u and p terms are the same in this simulation cell as in the previous cubic case, with the $\mathbf{G}_\ell$ vectors for the p term being the reciprocal lattice vectors of the simulation cell, organised into stars of equal-length vectors. In order to use the ν term we generalise its functional form to allow for the use of non-cuboidal simulation cells.

4.4.1   Generalised form of ν term

To begin the generalisation of the ν term we construct a set of vectors $\{\mathbf{B}\}$, formed of the primitive reciprocal lattice vectors of the simulation cell and all symmetry-equivalent vectors. These vectors are exactly those normal to the faces of the conventional unit cell, and so encode the symmetry of the simulation cell, and have length such that $|\mathbf{B}_i \cdot \mathbf{r}_{\text{face}}| = \pi$, for any vector $\mathbf{r}_{\text{face}}$ lying in the corresponding conventional cell faces.

Constructing a matrix of the reciprocal lattice vectors $\{\mathbf{B}\}$ and then (left-)inverting and transposing it leads to a set of real-space vectors $\{\mathbf{A}\}$. By measuring the projection of the electron-electron separation vector $\mathbf{r}$ onto these real-space vectors we can express the electron-electron separation as $\mathbf{r} = \sum_\zeta \mathbf{A}_\zeta (\mathbf{B}_\zeta \cdot \mathbf{r})$. The

inter-particle distance r can then be expressed as

$$r = \sqrt{\left(\sum_\zeta \mathbf{A}_\zeta [\mathbf{B}_\zeta \cdot \mathbf{r}] \right) \cdot \left(\sum_\xi \mathbf{A}_\xi [\mathbf{B}_\xi \cdot \mathbf{r}] \right)}$$
$$= \sqrt{\sum_i \mathbf{A}_i \cdot \mathbf{A}_i w_i^2 + 2 \sum_{j>k} \mathbf{A}_j \cdot \mathbf{A}_k w_j w_k},$$

where $w_i = \mathbf{B}_i \cdot \mathbf{r}$ expresses the projection of $\mathbf{r}$ onto $\mathbf{A}_i$ as a phase between $-\pi$ and π as $\mathbf{r}$ runs between parallel faces of the convex conventional cell. In a directly analogous way to the previous, cuboidal form we then define the Jastrow function as

$$\nu_{\sigma\tau}(\mathbf{r}) = \sum_{n=1}^{N_\nu} c_{n,\sigma\tau} \left| \sum_i \mathbf{A}_i \cdot \mathbf{A}_i f^2(w_i) + 2 \sum_{j>k} \mathbf{A}_j \cdot \mathbf{A}_k g(w_j) g(w_k) \right|^{n/2}, \qquad (4.5)$$

where in order to reduce to a radial expression at short radius we require that $f(w_i) \to |w_i|$ and $g(w_i) \to w_i$ as $\mathbf{r} \to \mathbf{0}$. In order to retain the symmetry of the simulation cell at large radii we demand $f(w_i)$ be symmetric under $w_i \to -w_i$, whilst $g(w_i)$ is required to be antisymmetric, and both functions should satisfy periodic boundary conditions at $|w_i| = \pi$. To satisfy these requirements we take f and g to have the simple forms

$$f(w_i) = |w_i| \left(1 - \frac{|w_i/\pi|^3}{4} \right)$$
$$g(w_i) = w_i \left(1 - \frac{3}{2} |w_i/\pi| + \frac{1}{2} |w_i/\pi|^2 \right). \qquad (4.6)$$

$f(w_i)$ is very similar to the cuboidal form given in Eq. (4.4), and if we use a cuboidal simulation cell with orthogonal lattice vectors, where $\{\mathbf{A}\} = \{\mathbf{a}_1/2\pi, \mathbf{a}_2/2\pi, \mathbf{a}_3/2\pi\}$ and $\{\mathbf{B}\} = \{\mathbf{b}_1, \mathbf{b}_2, \mathbf{b}_3\}$, the general form of the Jastrow function Eq. (4.5) reduces to the cuboidal form Eq. (4.4). $g(w_i)$ is the lowest-order polynomial-like expansion that is antisymmetric under $w_i \to -w_i$. The sets of vectors $\{\mathbf{A}\}$ and $\{\mathbf{B}\}$ that we use for the hexagonal simulation cell, as well as for other common simulation cell geometries, are given in Appendix C.

4.4.2   Electron-ion correlations

In crystalline systems there are correlations between the ions and electrons, as well as those between electrons. The DFT orbitals in the Slater determinants describe most of the electron-ion correlations, but these are modified by the introduction of electron-electron correlations in the Jastrow factor: in our simulations we add optimisable electron-ion correlations to the electron-electron Jastrow factor to counter this,

$$J(\mathbf{R}) = \sum_{\substack{j>i \\ \sigma,\tau\in\{\uparrow,\downarrow\}}} J_{\sigma\tau}(\mathbf{r}_{ij}) + \sum_{\substack{i,I \\ \sigma\in\{\uparrow,\downarrow\}}} \chi_\sigma(\mathbf{r}_{iI}),$$

where $\mathbf{r}_{iI} = \mathbf{r}_i - \mathbf{r}_I$, for ion positions $\mathbf{r}_I$, i running over all electrons, and I running over all ions. It has been shown [80, 134] that a short-ranged u-like expansion in electron-ion separation,

$$\chi_\sigma(\mathbf{r}_{iI}) = \left(\frac{L_\sigma^\chi}{3}\beta_{1,\sigma} + \sum_{m=1}^{N_\chi} \beta_{m,\sigma} r_{iI}^m \right) (1 - r_{iI}/L_\sigma^\chi)^3\, \Theta(L_\sigma^\chi - r_{iI}),$$

captures the most important electron-ion correlations in the electron-ion term, without the need for a longer-ranged p-like term. The cutoff length L_σ^χ is generally comparable to the inter-ionic distance, and we use $N_\chi = 4$ in our simulations. As we use pseudopotentials for the ions there is no gradient discontinuity in the wavefunction at electron-ion coincidence. We also tested a cuspless form of the ν Jastrow function to capture the electron-ion correlations, which agreed with the energies obtained using $\chi_\sigma(\mathbf{r}_{iI})$ to within 10^{-5} a.u. with the same number of variational parameters. This confirms that it is the short-range electron-ion correlations that are the most important to capture, and so we shall use the well-established $\chi_\sigma(\mathbf{r}_{iI})$ term in the following investigations.

In all-electron QMC simulations, particularly of molecules, the addition of three-body electron-electron-ion correlations to the Jastrow factor lowers the calculated energy [37, 80, 164], as these terms allow a more detailed description of tightly-bound electrons. However, electron-electron-ion correlations are less important in simulations using pseudopotentials, and including them here changes the correlation energy by less than 0.9%. Similarly to the electron-ion term the dominant effect of
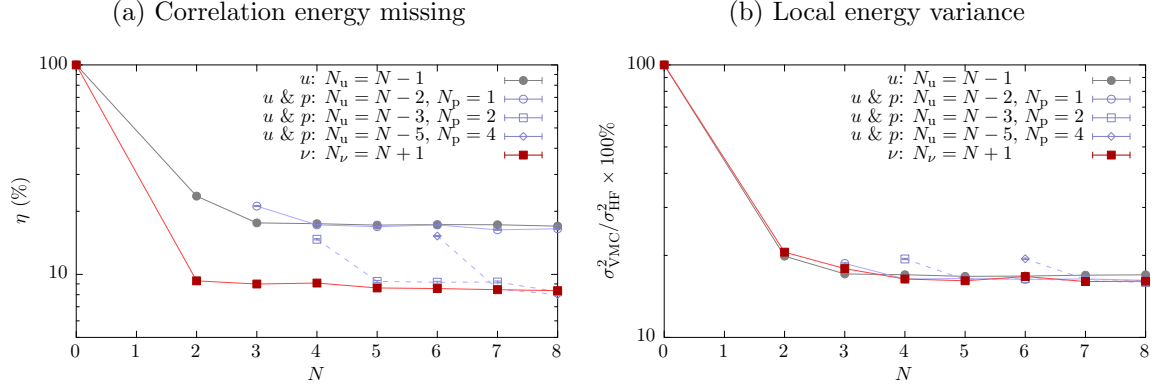
Figure 4.4: (a) The percentage of the DMC correlation energy missing from VMC simulations of crystalline beryllium, with N optimisable parameters in the Jastrow factor. Grey, blue, and red lines correspond to the u, u & p, and ν term respectively. (b) The variance in the local energy when using different Jastrow factors, as a percentage of the variance in the local energy using the Hartree–Fock wavefunction. Error bars, where not visible, are smaller than the size of the points.

electron-electron-ion terms is at short radius, and so the ν Jastrow factor formalism is expected to offer limited improvements relative to an isotropic u-like term in constructing such terms. As electron-electron-ion terms make a small difference to the energy and will not help us to discriminate between the u, u & p, and ν terms we neglect them here, although they should of course be included in simulations targeting high accuracy.

The full Jastrow function is then obtained by combining the electron-ion term $\chi_\sigma(\mathbf{r}_{iI})$ with the electron-electron Jastrow functions under examination, the u, u & p, and generalised ν terms. We now examine the accuracy and efficiency of these Jastrow functions for simulating crystalline beryllium.

4.4.3 Results

In Fig. 4.4a we compare the percentages of the DMC correlation energy missing, η, when the various Jastrow factors are used with N variational parameters in the electron-electron Jastrow factor. We observe that a u term alone is always missing nearly 20% of the correlation energy, and moreover that the addition of a single p term does not significantly improve the result. This is in contrast to the case of the HEG, where the addition of a single p term was the most important step in

Crystal type (example system)	ν	u & p: $N_{\mathrm{p}} = 2$
Hexagonal (Be)	8.6(1)%	9.3(1)%
BCC (Li)	4.7(1)%	5.0(1)%
FCC (Si)	10.1(2)%	9.6(2)%

Table 4.1: The percentage of the DMC correlation energy missing within VMC, η, for the ν and u & p terms with $N = 5$ in example systems: crystalline beryllium in a hexagonal simulation cell; crystalline lithium in a body-centred cubic (BCC) simulation cell; and crystalline silicon in a face-centred cubic (FCC) simulation cell. Bracketed numbers indicate the standard error in the values for η.

achieving a high-accuracy u & p term. This is due to the fact that, in the beryllium simulation cell, the $\mathbf{b}_3$ lattice vector orthogonal to the hexagonal planes is shorter than those in the $\mathbf{b}_1$, $\mathbf{b}_2$ plane, and so the first p term only acts along the c axis, not providing flexibility to capture correlations in the hexagonal planes. However, the addition of just one more p term reduces the correlation energy missing to around 9%, and the addition of more p terms to this does not significantly alter the result. This means that to achieve convergence we again require $N = 5$ when using the u & p term.

As in the HEG, the ν term achieves comparable accuracy to the most accurate u & p terms, reaching convergence by $N = 2$. This, combined with the necessity of otherwise using $N \geq 5$ for the u and p term, of which $N_{\mathrm{p}} = 2$ are expensive p terms, means that the ν term is significantly cheaper to optimise and use than alternative Jastrow factors.

In Fig. 4.4b we examine the variance in the local energy using different Jastrow factors. There is significantly less difference here between the Jastrow factors than in the proportion of the correlation energy they capture, but the ν term again performs as well as the most detailed other Jastrow factors, meaning that the trial wavefunctions have similar efficiency in DMC.

As well as hexagonal crystalline beryllium, we have also tested the electron-electron ν term in other crystals with different symmetry. The missing correlation energy when using the ν term and the $N_{\mathrm{p}} = 2$ u & p term is shown in Table 4.1. The u & p term is not significantly improved by increasing N_{p} in any of these crystals, and we use $N = 5$ as this is where the u & p term approaches its converged accuracy; in each case the ν term is already converged.

The two Jastrow factors capture similar levels of the correlation energy in each

system, indicating that the ν term is a good general choice of Jastrow factor for use in crystalline systems, with the slight differences between the ν and u & p terms in different systems being due to the exact details of the symmetry of the simulation cell in each case, some of which are better captured by the ν term than others. However, overall the differences between Jastrow factors are smaller than the differences between systems, and the ν Jastrow factor achieves high accuracy whilst having fewer (and only linear) parameters to optimise and being cheaper to evaluate, due to being polynomial as opposed to sinusoidal.

4.5   Discussion

We have proposed and tested a form of electron-electron Jastrow factor that interpolates between the radial symmetry of the Coulomb potential at short range and the space-group symmetry of the simulation cell at large separation. The ν Jastrow factor captures comparable levels of the correlation energy to the most detailed u & p terms used in the literature, and converges with fewer variational parameters. There is also only one choice of input to the ν term, the expansion order N_{ν}, which reduces the parameter space to be explored compared to the two variables, N_{u} and N_{p}, required for the u & p term. Finally, the polynomial ν term is quicker to evaluate than the plane-wave p term.

It would be possible to apply the ideas behind the ν term to higher angular-momentum terms in a Jastrow factor: for instance, carrying out the transformation $x/r \rightarrow g(x)/\sqrt{f^2(x) + f^2(y) + f^2(z)}$ would allow the Y_{11} spherical harmonic to be expressed in a way that satisfies the symmetry of a cuboidal simulation cell. The ν term could also be used in systems with interactions other than the Coulomb potential; for instance, QMC may also be used to study the dipolar [112] and contact [165] interactions in cold atomic gases, and also more exotic interactions such as those found in 2D semiconductors [166]. The interpolation between symmetries of the ν term could also be applicable more widely than just in Jastrow factors. Any expansion in or use of inter-particle separation in a numerical investigation could be written instead in terms of the f and g functions of the ν term, and so would immediately satisfy periodic boundary conditions in the simulation cell. Systems that might be well-suited to this approach could include two-particle pairing orbitals in Slater determinants [167], large-amplitude phonons simulated within density func-

tional theory [168], or the construction of force fields that natively reflect bond angles for molecular dynamics simulations [169].

The ν Jastrow factor is implemented in the CASINO QMC package [65,170]. Data used for this Chapter are available online [171].

Part II

Multi-particle superconductivity

Chapter 5

Multi-particle instability in a spin-imbalanced Fermi gas

Weak attractive interactions in a spin-imbalanced Fermi gas induce a multi-particle instability, binding multiple fermions together. The maximum binding energy per particle is achieved when the ratio of the number of up- and down-spin particles in the instability is equal to the ratio of the up- and down-spin densities of states in momentum at the Fermi surfaces, to utilise the variational freedom of all available momentum states. We derive this result using an analytical approach, and verify it using exact diagonalisation. The multi-particle instability extends the Cooper pairing instability of balanced Fermi gases to the imbalanced case, and in Chapter 6 will be shown to form the basis of a many-body state, analogously to the construction of the Bardeen–Cooper–Schrieffer theory of superconductivity out of Cooper pairs.

5.1   Introduction

Attractive interactions have a long and noteworthy history as the progenitors of strongly correlated states. One of the earliest yet most profound insights was that attractive interactions between up- and down-spin electrons may induce a pairing instability, resulting in the formation of Cooper pairs [172]. These Cooper pairs then form the basis of the many-body Bardeen–Cooper–Schrieffer (BCS) theory of superconductivity [42, 43]. Furthermore, even when there are unequal numbers of up- and down-spin particles in a system, Fulde and Ferrell [173] and, separately, Larkin and Ovchinnikov [174] (FFLO) showed that it is still energetically favourable for up- and down-spin particles from their respective Fermi surfaces to form Cooper pairs, leading to a strongly correlated superconducting phase in spin-imbalanced Fermi gases [175, 176]. However, the density of states in momentum at the Fermi surface of the majority-spin particles is greater than that of the minority-spin species, so the number of bound pairs that can exist is limited by the number of minority-spin particles, leaving many of the majority-spin particles at their Fermi surface unpaired and so uncorrelated. We propose a multi-particle instability that involves multiple majority-spin particles for each minority-spin particle, allowing us to utilise all of the potential of the majority-spin particles for contributing correlation energy. We find that the number of particles involved in the instability per species is proportional to the density of states in momentum at their respective Fermi surfaces. The multi-particle instability has more binding energy per particle than a Cooper pair, so could replace the Cooper pair as the building block of a superconducting state in spin-imbalanced Fermi gases.

The prototypical experimental realisation of an imbalanced Fermi gas is electrons in an external magnetic field. Most superconductors are destroyed by an external magnetic field, reverting to the normal phase. However some materials, including CeCoIn$_5$ [177] and κ-(BEDT-TTF)$_2$Cu(NCS)$_2$ [178], which are superconducting at zero magnetic field, with increasing field undergo a phase transition into an exotic second superconducting state, before a further transition into the normal phase. Other materials, including ErRh$_4$B$_4$ [179] and ErNi$_2$B$_2$C [180], display overlap of ferromagnetism and superconductivity at zero applied field, and it has recently been suggested that Bi$_2$Sr$_2$CaCu$_2$O$_{8+x}$ exhibits some characteristics of an FFLO-like phase in the pseudogap regime [181]. Further possible realisations of FFLO

superconductivity in spin-imbalanced Fermi gases include an ultracold atomic gas of fermions trapped in one dimension that displays a transition between superconducting phases [182], or a spin-orbit coupled superconductor with imbalanced Fermi surfaces [29, 30]. However, the exotic superconducting state has not been fully characterised in any of these systems, leaving the true nature of the ground state an open question.

We follow the prescription of Cooper [172] to study a multi-particle instability on top of the Fermi surfaces. Working in second quantisation notation, we construct a trial wavefunction for a multi-particle instability of several majority-spin particles binding to a (potentially smaller) number of minority-spin particles to make the binding energy per particle larger than for a Cooper pair. The optimal ratio for the number of majority- to minority-spin particles is found to be the ratio of the densities of states in momentum at their respective Fermi surfaces.

To verify our multi-particle instability we analyse the system with exact diagonalisation. We confirm that our second quantised wave function captures the crucial correlations of the exact solution, expose additional insights into the structure of the wavefunction, and verify our conclusion that the optimal number of particles in the instability is set by the ratio of the densities of states in momentum.

5.2 Theory

To explore the possibility of the multi-particle instability we study a two-spin fermionic system with an attractive contact interaction at zero temperature. The BCS Hamiltonian takes the form

$$\hat{H} = \sum_{\sigma, \mathbf{k}} \xi_{\sigma\mathbf{k}} c_{\sigma\mathbf{k}}^{\dagger} c_{\sigma\mathbf{k}} - g \sum_{\mathbf{k}, \mathbf{k}', \mathbf{q}} c_{\uparrow(\mathbf{q}-\mathbf{k})}^{\dagger} c_{\downarrow\mathbf{k}}^{\dagger} c_{\downarrow\mathbf{k}'} c_{\uparrow(\mathbf{q}-\mathbf{k}')}, \tag{5.1}$$

where $\sigma \in \{\uparrow, \downarrow\}$ is the spin index, $\xi_{\sigma\mathbf{k}}$ is the single-particle dispersion for spin species σ and momentum $\mathbf{k}$, $c_{\sigma\mathbf{k}}^{\dagger}$ ($c_{\sigma\mathbf{k}}$) is a creation (annihilation) operator for a fermionic particle, and $g > 0$ is the strength of the attractive contact interaction. In the absence of interactions the ground state of the Hamiltonian in Eq. (5.1) is a

(a) $(N_\uparrow, N_\downarrow) = (1, 1)$ Cooper pair instability

(b) $(N_\uparrow, N_\downarrow) = (2, 1)$ multi-particle instability
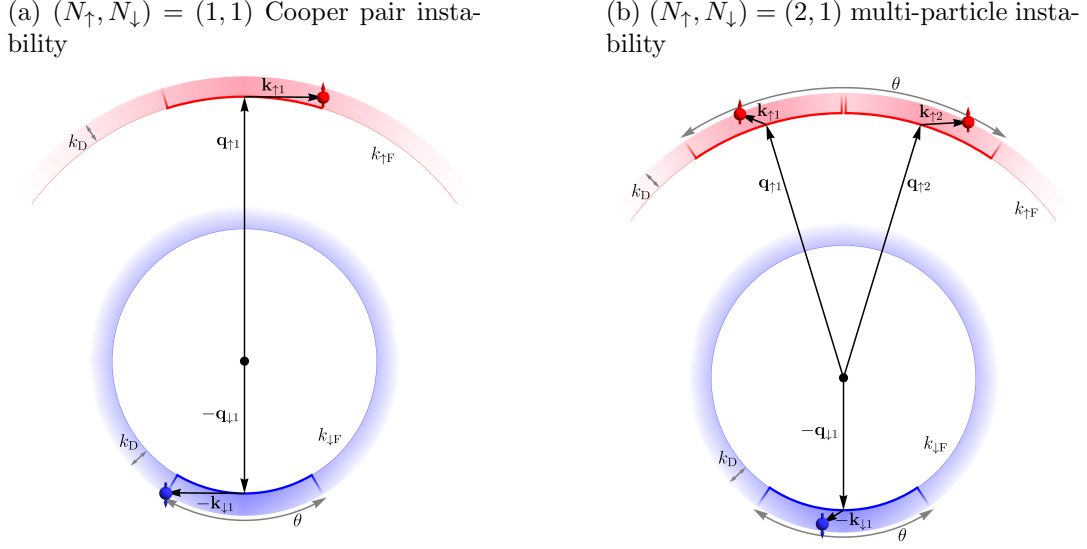
Figure 5.1: Idealised representation of the spin-imbalanced system showing Fermi surfaces for the down- (light blue circle) and up-spin (light red fragment of circle) species, with shaded areas denoting the allowed momentum states extending outwards by the Debye momentum k_D. Also shown are Fermi surface arcs, bounded by thick blue lines for the down-spin species and thick red lines for the up-spin species, for (a) the simplest instability of one up-spin and one down-spin particle, and (b) a proposed multi-particle instability with $(N_\uparrow, N_\downarrow) = (2, 1)$, indicating the bounds on the momentum states $\mathbf{k}_{\sigma i}$ used in the trial wavefunctions.

filled Fermi sea,

$$|\mathrm{FS}\rangle = \prod_{\xi_{\uparrow \mathbf{k}_\uparrow} < E_{\uparrow \mathrm{F}}} c^\dagger_{\uparrow \mathbf{k}_\uparrow} \prod_{\xi_{\downarrow \mathbf{k}_\downarrow} < E_{\downarrow \mathrm{F}}} c^\dagger_{\downarrow \mathbf{k}_\downarrow} |0\rangle,$$

with species-dependent Fermi energies $E_{\sigma \mathrm{F}}$ (corresponding to Fermi momenta $k_{\sigma \mathrm{F}}$) and $|0\rangle$ being the vacuum state. Without loss of generality we fix the number of particles in the Fermi sea of the up-spin species to be greater than or equal to that of the down-spin species. We follow the prescription of Cooper [172] and assume that the non-interacting ground state remains undisturbed for $\xi_{\sigma \mathbf{k}} < E_{\sigma \mathrm{F}}$, and focus only on a few-particle instability at $\xi_{\sigma \mathbf{k}} \gtrsim E_{\sigma \mathrm{F}}$. We work in a general number $D \geq 2$ of dimensions.

5.2.1   Fermi surface arcs

The idealised conceptual situation where we expect a multi-particle instability to be present consists of two Fermi surfaces for the different species that are different sizes, but otherwise geometrically similar. In Fig. 5.1 we show example Fermi surfaces for the up- and down-spin particles in $D = 2$ dimensions. Above the Fermi surfaces are the unoccupied momentum states that can host the multi-particle instability, which for typical phonon-mediated interactions extend over a species-independent Debye momentum k_{D}. We assume that $k_{\mathrm{D}}/k_{\sigma\mathrm{F}} \ll 1$, as for many conventional superconductors [183–185].

To construct the trial wavefunction for the multi-particle instability, we start by developing multi-particle basis states. To capture all possible correlations in the system, we require that the interaction term in the Hamiltonian can couple the different basis states. As the interaction term conserves momentum, all basis states must have the same total momentum. To construct these basis states, first consider the Cooper pair situation with only one up-spin and one down-spin particle in the instability. We start with a basis state that has both particles on their respective Fermi surfaces on opposite sides of the Fermi seas (at the momenta labelled $\mathbf{q}_{\uparrow 1}$ and $-\mathbf{q}_{\downarrow 1}$ in Fig. 5.1a). In systems with anisotropic Fermi surfaces, like many of the candidate systems for FFLO [186–188], the Cooper pair (and, later, the multi-particle instability) will be dominated by the lowest-curvature parts of the Fermi surface, and so in a general dispersion we place the initial basis state at the points on the Fermi surfaces with the lowest curvature.

If we move away from these starting momenta, tangentially to the Fermi surfaces by equal and opposite momenta for the different species to conserve momentum, we eventually reach the Debye momentum k_{D} above the Fermi surfaces where there are no more momentum states accessible via the interaction term (reach the outer edge of the shaded regions in Fig. 5.1a). The tighter curvature of the down-spin species means we will first run out of allowed momentum states for the down-spin species (at the point $-\mathbf{q}_{\downarrow 1} - \mathbf{k}_{\downarrow 1}$ in Fig. 5.1a). The angular width of the allowed down-spin momentum states thus sets the angular width of the up-spin momentum states for Cooper pairs.

We refer to the allowed momentum states for the particles as forming 'arcs' on the Fermi surfaces. An idealised version of the available momentum states for the

down-spin species is indicated in Fig. 5.1a by the arc above the down-spin Fermi surface bounded by blue lines, with angular width θ. The corresponding up-spin species arc is shown bounded by red lines.

Because it was the down-spin species that exhausted its available momentum states first in the Cooper pair situation in Fig. 5.1a, we wasted the opportunity for some up-spin species momentum states to become involved in the instability and so lower the energy of the system. We can make use of twice as many up-spin momentum states by duplicating the arc of up-spin momentum states that were available in the Cooper pair situation, offsetting the arcs so they do not intersect as required by Pauli exclusion, and placing a particle in each arc. If we allow either up-spin particle to interact with the down-spin particle, we have increased the variational freedom in the system and would generically expect the binding energy to become larger. Two such Fermi surface arcs for the up-spin species are shown in Fig. 5.1b, bounded by red lines.

We can generalise the above argument to include more than two up-spin and more than one down-spin particles: in general we may have $N_\uparrow$ up-spin arcs and particles, and $N_\downarrow$ down-spin arcs and particles. However, if we include too many particles, the gradients of the Fermi surfaces of the different species will differ radically at the extremal Fermi surface arcs, and it will not be possible to move around one species' arc without immediately pushing the other species out of their allowed momentum states. We bound the maximum extent of the Fermi surface arcs by noting that when the tangents to the species' Fermi surfaces are parallel it is possible to move particles of both species simultaneously without either being forced from their allowed momentum states. For dispersions with inversion symmetry this is achieved when the total angular widths of the two species' arcs are equal, shown in Fig. 5.1b with the total width of the arcs of both species taking the value θ.

The densities of states in momentum of the occupied arcs, ν_σ, describe the availability of momentum states throughout all arcs for each species, in our two-dimensional example being proportional to θ. The density of states in momentum per particle is then ν_σ/N_σ. The species with the smaller value of this ratio limits the angular size available for each particle to move in, and we refer to this as the 'critical' species, with N_c particles and density of states in momentum ν_c.

To show that an instability with multiple particles in separate Fermi surface arcs is the energetically favourable solution for a broad class of spin-imbalanced systems,

we follow the approach of Cooper [172] to construct a variational wavefunction for the multi-particle instability. We demonstrate that in spin-imbalanced systems the multi-particle instability gives an improved binding energy over traditional Cooper pairs.

5.2.2 Basis states

To formalise the above description of the Fermi surface arcs, we label the angular centre of each arc, on the Fermi surface, by a q-vector $\mathbf{q}_{\sigma i}$. These q-vectors therefore satisfy $|\mathbf{q}_{\sigma i}| = k_{\sigma \mathrm{F}}$ for a free dispersion and $\xi_{\sigma \mathbf{q}_{\sigma i}} = E_{\sigma \mathrm{F}}$. For $k_{\mathrm{D}} \ll k_{\sigma \mathrm{F}}$ and so small θ the $\mathbf{q}_{\sigma i}$ for both species can be taken to be parallel, $|\mathbf{q}_{\sigma i} - \mathbf{q}_{\sigma j}| \ll |\mathbf{q}_{\sigma i}|$. All the momenta within a particular arc are described by $\mathbf{q}_{\sigma i} + \mathbf{k}_{\sigma i}$, where the vectors $\mathbf{k}_{\sigma i}$ indicate the positions of the particles within the Fermi surface arcs, and for small $k_{\mathrm{D}} \ll k_{\sigma \mathrm{F}}$ we have $|\mathbf{k}_{\sigma i}| \ll |\mathbf{q}_{\sigma i}|$. This guarantees $\xi_{\uparrow (\mathbf{q}_{\uparrow i} + \mathbf{k}_{\uparrow i})} \gtrsim E_{\uparrow \mathrm{F}}$ and $\xi_{\downarrow (-\mathbf{q}_{\downarrow j} - \mathbf{k}_{\downarrow j})} \gtrsim E_{\downarrow \mathrm{F}}$ so that the particle momenta lie near their corresponding Fermi surfaces. Examples of this labelling procedure are shown in Fig. 5.1.

The proposed multi-particle instability is an excitation of $(N_\uparrow, N_\downarrow)$ correlated particles on top of the undisturbed Fermi seas, with each particle existing in a unique arc. This can be constructed out of basis states

$$|\mathbf{K}_\uparrow; \mathbf{K}_\downarrow\rangle = \prod_i^{N_\uparrow} c_{\uparrow (\mathbf{k}_{\uparrow i} + \mathbf{q}_{\uparrow i})}^\dagger \prod_j^{N_\downarrow} c_{\downarrow (-\mathbf{k}_{\downarrow j} - \mathbf{q}_{\downarrow j})}^\dagger |\mathrm{FS}\rangle,$$

where $\mathbf{K}_\sigma = (\mathbf{k}_{\sigma 1}, \mathbf{k}_{\sigma 2}, \dots, \mathbf{k}_{\sigma N_\sigma})$ is an $N_\sigma \times D$ matrix of particle momenta in D spatial dimensions.

5.2.3 Trial wavefunction

The trial wavefunction for a system with a given set of $\mathbf{q}_{\sigma i}$ vectors is a sum over basis states with optimisable coefficients $\alpha(\mathbf{K}_\uparrow, \mathbf{K}_\downarrow)$,

$$|\psi\rangle = \sideset{}{'}\sum_{\mathbf{K}_\uparrow, \mathbf{K}_\downarrow} \alpha(\mathbf{K}_\uparrow, \mathbf{K}_\downarrow) |\mathbf{K}_\uparrow; \mathbf{K}_\downarrow\rangle, \tag{5.2}$$

where the sum is over all N_σ momentum components $\mathbf{k}_{\sigma i}$ of each matrix $\mathbf{K}_\sigma$, with the prime on the sum indicating that we only sum over $\mathbf{k}_{\sigma i}$ such that $\sum_i^{N_\uparrow} \mathbf{k}_{\uparrow i} = \sum_j^{N_\downarrow} \mathbf{k}_{\downarrow j}$,

ensuring momentum conservation. We take the $\alpha(\mathbf{K}_\uparrow, \mathbf{K}_\downarrow)$ coefficients to be non-zero only if all of the momenta $\mathbf{k}_{\sigma i}$ lie within their respective arcs of the Fermi surfaces. With $N_\uparrow = N_\downarrow = 1$ Eq. (5.2) collapses to the trial wavefunction for a Cooper pair.

5.2.4   Kinetic energy

To find an analytic expression for the energy expectation value E, we first focus on the kinetic energy term and linearise the dispersions near the Fermi surfaces, $\xi_{\sigma\mathbf{p}} \approx (|\mathbf{p}| - k_{\sigma\mathrm{F}})\xi'_{\sigma k_{\sigma\mathrm{F}}}$. Here $k_{\sigma\mathrm{F}}$ is the momentum corresponding to the Fermi energy, which for small enough $k_\mathrm{D} \ll k_{\sigma\mathrm{F}}$ can be considered constant over the Fermi surface arcs, and $\xi'_{\sigma k_{\sigma\mathrm{F}}}$ is the derivative of the single-particle energy at the Fermi surface. For the dispersions involved, $\xi_{\uparrow(\mathbf{k}_{\uparrow i}+\mathbf{q}_{\uparrow i})}$ and $\xi_{\downarrow(-\mathbf{k}_{\downarrow i}-\mathbf{q}_{\downarrow i})}$, recall that $|\mathbf{q}_{\sigma i}| = k_{\sigma\mathrm{F}}$ and $|\mathbf{k}_{\sigma i}| \ll |\mathbf{q}_{\sigma i}|$, and so $\xi_{\uparrow(\mathbf{k}_{\uparrow i}+\mathbf{q}_{\uparrow i})} \approx k_{\uparrow i}\xi'_{\uparrow k_{\uparrow\mathrm{F}}}$ and $\xi_{\downarrow(-\mathbf{k}_{\downarrow i}-\mathbf{q}_{\downarrow i})} \approx k_{\downarrow i}\xi'_{\downarrow k_{\downarrow\mathrm{F}}}$ where $k_{\sigma i}$ is the projection of $\mathbf{k}_{\sigma i}$ along $\mathbf{q}_{\sigma i}$ (or equivalently, the radial component of $\mathbf{k}_{\sigma i}$).

This linearity simplifies the full expression for the kinetic energy of our trial wavefunction. With kinetic energy operator $\hat{T} = \sum_{\sigma,\mathbf{k}} \xi_{\sigma\mathbf{k}} c^\dagger_{\sigma,\mathbf{k}} c_{\sigma,\mathbf{k}}$, we find

$$\langle \mathbf{K}_\uparrow; \mathbf{K}_\downarrow | \hat{T} | \psi \rangle$$

$$= \alpha(\mathbf{K}_\uparrow, \mathbf{K}_\downarrow) \left(\sum_i^{N_\uparrow} \xi_{\uparrow(\mathbf{k}_{\uparrow i}+\mathbf{q}_{\uparrow i})} + \sum_j^{N_\downarrow} \xi_{\downarrow(-\mathbf{k}_{\downarrow j}-\mathbf{q}_{\downarrow j})} \right)$$

$$\approx \alpha(\mathbf{K}_\uparrow, \mathbf{K}_\downarrow) \left(\sum_i^{N_\uparrow} k_{\uparrow i}\xi'_{\uparrow k_{\uparrow\mathrm{F}}} + \sum_j^{N_\downarrow} k_{\downarrow j}\xi'_{\downarrow k_{\downarrow\mathrm{F}}} \right),$$

which may be simplified further by using the conservation of total momentum to define $\sum_i^{N_\uparrow} k_{\uparrow i} = \sum_j^{N_\downarrow} k_{\downarrow j} = K$, giving

$$\langle \mathbf{K}_\uparrow; \mathbf{K}_\downarrow | \hat{T} | \psi \rangle \approx 2\alpha(\mathbf{K}_\uparrow, \mathbf{K}_\downarrow) K \xi',$$

with $\xi' = \frac{1}{2}(\xi'_{\uparrow k_{\uparrow\mathrm{F}}} + \xi'_{\downarrow k_{\downarrow\mathrm{F}}})$.

5.2.5 Potential energy

To evaluate the total energy of the wavefunction $|\psi\rangle$ we also need to evaluate the effect of the potential energy operator $\hat{V} = g\sum_{\mathbf{k},\mathbf{k}',\mathbf{q}} c^{\dagger}_{\uparrow(\mathbf{q}-\mathbf{k})} c^{\dagger}_{\downarrow\mathbf{k}} c_{\downarrow\mathbf{k}'} c_{\uparrow(\mathbf{q}-\mathbf{k}')}$. The interaction operator removes two particles, one of each spin species, from a basis state and then replaces them, having transferred momentum $\mathbf{m} = \mathbf{k}' - \mathbf{k}$ between them. For a general basis state $|\mathbf{K}_{\uparrow}; \mathbf{K}_{\downarrow}\rangle$ there are $N_{\uparrow}N_{\downarrow}$ ways of choosing the pairs of particles that are involved. We can formalise this procedure by defining

$$\hat{V}|\mathbf{K}_{\uparrow};\mathbf{K}_{\downarrow}\rangle = g\sum_{\vec{P}_{\uparrow},\vec{P}_{\downarrow},\mathbf{m}} \left| \mathbf{K}_{\uparrow} - \vec{P}_{\uparrow} \otimes \mathbf{m}; \mathbf{K}_{\downarrow} - \vec{P}_{\downarrow} \otimes \mathbf{m} \right\rangle, \qquad (5.3)$$

and hence

$$\langle \mathbf{K}_{\uparrow};\mathbf{K}_{\downarrow}|\hat{V}|\psi\rangle = g\sum_{\vec{P}_{\uparrow},\vec{P}_{\downarrow},\mathbf{m}} \alpha\left(\mathbf{K}_{\uparrow} - \vec{P}_{\uparrow} \otimes \mathbf{m}, \mathbf{K}_{\downarrow} - \vec{P}_{\downarrow} \otimes \mathbf{m} \right),$$

where the vectors $\vec{P}_{\sigma}$ form a set of standard basis vectors in particle-number space: each has one element that takes the value 1, with the remaining $(N_{\sigma} - 1)$ elements having value 0. These label the particles in the different arcs in Fig. 5.1b. The effect of an outer product of a $\vec{P}_{\sigma}$ vector with a scattering vector $\mathbf{m}$ is to construct the matrix $(\mathbf{0}, \ldots, \mathbf{m}, \ldots, \mathbf{0})$, where the column containing $\mathbf{m}$ is determined by the particular $\vec{P}_{\sigma}$ vector. We sum over all possible pairs of up- and down-spin particles.

5.2.6 Multi-particle instability

We are now ready to combine the effect of the kinetic and potential energies by projecting the full Schrödinger equation $\hat{H}|\psi\rangle = E|\psi\rangle$ onto the state $\langle \mathbf{K}_{\uparrow}; \mathbf{K}_{\downarrow}|$ to calculate the energy expectation value E. We find that

$$(2K\xi' - E)\,\alpha(\mathbf{K}_{\uparrow}, \mathbf{K}_{\downarrow})$$
$$= g\sum_{\vec{P}_{\uparrow},\vec{P}_{\downarrow},\mathbf{m}} \alpha\left(\mathbf{K}_{\uparrow} - \vec{P}_{\uparrow} \otimes \mathbf{m}, \mathbf{K}_{\downarrow} - \vec{P}_{\downarrow} \otimes \mathbf{m} \right),$$

which, following the approach of Cooper [172], we divide by $(2K\xi' - E)$ and sum over all $\mathbf{K}_\sigma$ to obtain

$$\sideset{}{'}\sum_{\mathbf{K}_\uparrow,\mathbf{K}_\downarrow} \alpha(\mathbf{K}_\uparrow, \mathbf{K}_\downarrow)$$

$$= g\sideset{}{'}\sum_{\mathbf{K}_\uparrow,\mathbf{K}_\downarrow} \sum_{\vec{P}_\uparrow,\vec{P}_\downarrow,\mathbf{m}} \frac{\alpha\left(\mathbf{K}_\uparrow - \vec{P}_\uparrow \otimes \mathbf{m}, \mathbf{K}_\downarrow - \vec{P}_\downarrow \otimes \mathbf{m}\right)}{2K\xi' - E}.$$

Shifting the dummy momentum variables $\mathbf{K}_\sigma$ on the right hand side by $\vec{P}_\sigma \otimes \mathbf{m}$ to remove the $\vec{P}_\sigma$ and $\mathbf{m}$ from the arguments of $\alpha(\mathbf{K}_\uparrow, \mathbf{K}_\downarrow)$, we bring the implicit expression for the energy to the form

$$\sideset{}{'}\sum_{\mathbf{K}_\uparrow,\mathbf{K}_\downarrow} \alpha(\mathbf{K}_\uparrow, \mathbf{K}_\downarrow)$$

$$= g \sum_{\vec{P}_\uparrow,\vec{P}_\downarrow} \sideset{}{'}\sum_{\mathbf{K}_\uparrow,\mathbf{K}_\downarrow} \alpha(\mathbf{K}_\uparrow, \mathbf{K}_\downarrow) \sum_{\mathbf{m}} \frac{1}{2(K+m)\xi' - E}, \qquad (5.4)$$

where m is the radial projection of $\mathbf{m}$. We can now separate the angular and radial parts of the sum over $\mathbf{m}$, and carry out the angular summation. The angular summation is limited by the critical species, giving a contribution of the density of available states ν_c/N_c, meaning that the whole sum over $\mathbf{m}$ should be considered as over the critical species.

We can also make the substitution $m' = K+m$, which has the effect of restraining the $\mathbf{K}_\sigma$ dependence of the right hand side of Eq. (5.4) entirely to the parameters $\alpha(\mathbf{K}_\uparrow, \mathbf{K}_\downarrow)$ and the limits of the sums over m'. However, the momentum m' accounts only for single momentum-transfer events, which following the prescription of Cooper theory have a maximum radial width in momentum of the Debye momentum k_D.

The maximum kinetic energy $2m'\xi'$ of a basis state is obtained when each particle is at the upper end of its Fermi surface arc, giving a total kinetic energy $2m'\xi' = (N_\uparrow + N_\downarrow)k_D\xi'$, and the minimum kinetic energy is obtained when each particle is at the bottom of its arc, for $2m'\xi' = 0$. The summation over m' may be

extended to cover this range, giving an implicit expression for the energy of

$$\sideset{}{'}\sum_{\mathbf{K}_\uparrow,\mathbf{K}_\downarrow} \alpha(\mathbf{K}_\uparrow,\mathbf{K}_\downarrow)$$

$$= \frac{2g\nu_\mathrm{c}}{(N_\uparrow+N_\downarrow)N_\mathrm{c}} \sum_{\vec{P}_\uparrow,\vec{P}_\downarrow} \sideset{}{'}\sum_{\mathbf{K}_\uparrow,\mathbf{K}_\downarrow} \alpha(\mathbf{K}_\uparrow,\mathbf{K}_\downarrow) \sum_{m'=0}^{\frac{(N_\uparrow+N_\downarrow)k_\mathrm{D}}{2}} \frac{1}{2m'\xi'-E}. \tag{5.5}$$

The only dependence on the $\mathbf{K}_\sigma$ in the implicit expression for the energy is in the coefficients $\alpha(\mathbf{K}_\uparrow,\mathbf{K}_\downarrow)$, so we can factorise out $\sum'_{\mathbf{K}_\uparrow,\mathbf{K}_\downarrow} \alpha(\mathbf{K}_\uparrow,\mathbf{K}_\downarrow)$ from both sides of Eq. (5.5). We have also removed all dependence on $\vec{P}_\sigma$ from the expression, and so can explicitly carry out those summations to give a factor of $N_\uparrow N_\downarrow$. This leaves us with

$$1 = g\frac{2N_\uparrow N_\downarrow}{(N_\uparrow+N_\downarrow)}\frac{\nu_\mathrm{c}}{N_\mathrm{c}} \sum_{m'=0}^{\frac{(N_\uparrow+N_\downarrow)k_\mathrm{D}}{2}} \frac{1}{2m'\xi'-E}, \tag{5.6}$$

analogous to Eq. (4) of Cooper's original paper [172].

We have reduced the complexity of the multi-particle instability to a single summation with a multiplicative constant. In the same manner as Cooper's original analysis we may now convert this summation to an integral and solve, finding the binding energy

$$E_\mathrm{b} = \frac{(N_\uparrow+N_\downarrow)k_\mathrm{D}\xi'}{\exp\left(\frac{(N_\uparrow+N_\downarrow)\xi'}{gN_\uparrow N_\downarrow}\frac{N_\mathrm{c}}{\nu_\mathrm{c}}\right)-1}. \tag{5.7}$$

In the weakly interacting limit this binding energy simplifies to

$$E_\mathrm{b} = (N_\uparrow+N_\downarrow)k_\mathrm{D}\xi'\exp\left(-\frac{(N_\uparrow+N_\downarrow)\xi'}{gN_\uparrow N_\downarrow}\frac{N_\mathrm{c}}{\nu_\mathrm{c}}\right), \tag{5.8}$$

similar to the familiar form of the binding energy of a Cooper pair.

We wish to identify the number of particles $(N_\uparrow, N_\downarrow)$ in the energetically optimal multi-particle instability. The strongest dependence of the binding energy in Eq. (5.8) on $N_\uparrow$ and $N_\downarrow$ is in the exponential, with the binding energy being maximised when the argument of the exponential function is least negative. The values

of N_σ which achieve this, and are therefore the optimal solutions for the system, can be deduced by symmetry to satisfy the relation

$$\frac{N_\uparrow}{N_\downarrow} = \frac{\nu_\uparrow}{\nu_\downarrow}, \tag{5.9}$$

i.e. the number of particles involved in the wavefunction per spin species is proportional to the density of states in momentum. This means that all of the available momentum states are involved in the instability, and so contributing the maximum possible binding energy. Eq. (5.9) suggests that in $D \geq 2$ dimensions a multi-particle instability is energetically favourable over conventional pair instabilities in a spin-imbalanced system.

In the next subsection we shall analyse our expression for the binding energy in the light of Eq. (5.9), which gives a definite prediction for the energetically optimal instability in different systems. We shall then return to the trial wavefunction given by Eq. (5.2), and look further at its properties and limits.

5.2.7 Binding energy analysis

To build our intuition for the expression for the binding energy of the multi-particle instability found in Eq. (5.7), we now examine the binding energy as a function of the ratio of the number of particles $N_\uparrow/N_\downarrow$. We render the binding energy dimensionless by normalising by g, the interaction strength; k_D, the maximum interaction momentum; $\nu_\uparrow \nu_\downarrow$, in order to account for different system sizes; and N_c/ν_c, the number of critical species particles per density of states in momentum. Normalising by this final ratio looks forward to the eventual creation of a many-body strongly-correlated state from multi-particle instabilities, with the number of instabilities merged being limited by the availability of critical species particles. We note, however, that at low interaction strengths the dominant term in the binding energy in Eq. (5.8) is the exponential, so the normalisation could be chosen to be by the total number of particles without affecting the results below. This results in a measure of the binding energy per critical species particle of

$$X_b = \frac{1}{g k_D \nu_\uparrow \nu_\downarrow} \frac{E_b}{N_c/\nu_c}. \tag{5.10}$$

To further justify this measure of the binding energy per critical species particle, we first examine the strongly interacting limit of Eq. (5.7). Here, in terms of the normalised ratio of number of particles per species,

$$x = \frac{N_\uparrow}{N_\downarrow} \frac{\nu_\downarrow}{\nu_\uparrow},$$

the binding energy per critical species particle takes the simple form

$$X_\mathrm{b} = \begin{cases} x, & x < 1, \\ 1/x, & x > 1. \end{cases} \tag{5.11}$$

This expression is maximised at $x = 1$, that is when $N_\uparrow/N_\downarrow = \nu_\uparrow/\nu_\downarrow$, in agreement with the expression in Eq. (5.9) for the weakly-interacting limit.

Away from the strongly- and weakly-interacting limits the optimal binding energy remains at $N_\uparrow/N_\downarrow = \nu_\uparrow/\nu_\downarrow$. In Fig. 5.2 we show the binding energy per critical species particle X_b from Eq. (5.7) as a function of imbalance x for ratios of densities of states in momentum $\nu_\uparrow/\nu_\downarrow \in \{1, 2, 3, 4\}$ at an intermediate interaction strength $g = E_{\uparrow\mathrm{F}}$. We take as an example system a free dispersion with $\xi'_{\sigma k_{\sigma\mathrm{F}}} = k_{\sigma\mathrm{F}}$ in $D = 2$ dimensions, so that $\nu_\sigma \propto k_{\sigma\mathrm{F}}$, although similar results hold in other systems. The balanced system $\nu_\uparrow = \nu_\downarrow$ is shown by the grey line, with the conventional Cooper state, having $N_\uparrow = N_\downarrow$, being the energetically optimal instability. This line is symmetric about $N_\uparrow/N_\downarrow = \nu_\uparrow/\nu_\downarrow$ on the log-log scale, which reflects the symmetry between spin species when $\nu_\uparrow = \nu_\downarrow$. For the spin-imbalanced systems where $\nu_\uparrow > \nu_\downarrow$, the energetically optimal instability is still found at $N_\uparrow/N_\downarrow = \nu_\uparrow/\nu_\downarrow$, as predicted by Eq. (5.9). To the right of this there are too many up-spin particles in the instability, and to the left there are too many down-spin particles in the instability; this leads to the $\nu_\uparrow > \nu_\downarrow$ lines not being symmetric about their maxima, as in imbalanced systems including the wrong number of up-spin particles is not equivalent to including the wrong number of down-spin particles.

Having examined the result of Eq. (5.9) that the optimum ratio of number of particles is given by the ratio of densities of states in momentum, we now discuss the difference between instabilities with different numbers of particles, but the same ratio $N_\uparrow/N_\downarrow$.
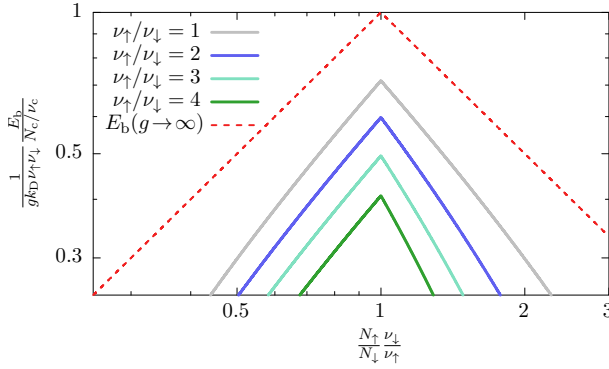
Figure 5.2: The binding energy per critical species particle as a function of the normalised ratio of number of particles per species at intermediate interaction strength $g = E_{\uparrow F}$. Results are shown for a free dispersion in $D = 2$ dimensions and for different imbalance ratios, with the infinite-interaction-strength limit indicated by a dashed line.

5.2.8   Instabilities with same ratio $N_\uparrow/N_\downarrow$

The prediction given in Eq. (5.9) that the energetically optimal numbers of particles involved in the instability are related by $N_\uparrow/N_\downarrow = \nu_\uparrow/\nu_\downarrow$ only sets the ratio between $N_\uparrow$ and $N_\downarrow$, but does not predict the absolute numbers of particles. To probe the effect of changing the absolute numbers of particles, we need to examine in more detail the effect of Pauli blocking.

The effect of Pauli blocking has been carefully analysed [189–191] for the product of two $(N_\uparrow, N_\downarrow) = (1,1)$ instabilities, and found to give only a small correction to the binding energy of two separate pairs (the correction going as the inverse of the number of available momentum states). This agreement with our result for a $(N_\uparrow, N_\downarrow) = (2,2)$ instability, up to small Pauli blocking corrections that vanish in the thermodynamic limit, supports our finding that the binding energy per critical species particle is independent of the total number of particles involved in the instability. We shall present further numerical evidence that captures the Pauli blocking corrections in Subsection 5.3.4.

However, the effect of Pauli blocking will become more acute in a many-body state constructed from multi-particle instabilities. This suggests that in the limit of a large number of multi-particle instabilities in a system, instabilities with fewer total particles will be energetically favourable over instabilities with more particles but the same value of $N_\uparrow/N_\downarrow$ in a given system.

Having investigated the structure and binding energy of the proposed multi-particle instability, we now turn to some of its limits. We examine the conventional Cooper system, with balanced Fermi seas, and identify the predictions made for one-

dimensional systems, recovering in both cases agreement with well-known results from the literature. We also briefly examine the strongly-interacting limit of the proposed multi-particle instability.

5.2.9 Cooper limit

The system studied originally by Cooper [172] is a balanced Fermi gas, and so has $k_{\uparrow\text{F}} = k_{\downarrow\text{F}} = k_\text{F}$, $\nu_\uparrow = \nu_\downarrow = \nu$, which we predict should have the optimal ratio $N_\uparrow/N_\downarrow = 1$ in agreement with Cooper's findings. Moreover, with $N_\uparrow = N_\downarrow = 1$ our trial wavefunction Eq. (5.2) reproduces the conventional Cooper trial wavefunction [172]. Therefore, with a free dispersion $\xi_{\sigma k} = k^2/2 - k_\text{F}^2/2$ the weakly-interacting binding energy given by Eq. (5.8) reduces to the familiar Cooper expression [172]

$$E_\text{b} = 2k_\text{D}\xi' \exp\left(-\frac{2k_\text{F}}{g}\frac{1}{\nu}\right) = 2\omega_\text{D} \exp\left(-\frac{2}{g\Omega}\right),$$

where the Debye energy $\omega_\text{D} = k_\text{D}\xi'$ and the density of states in energy $\Omega = \nu/k_\text{F}$.

5.2.10 One-dimensional limit

Although the discussion in previous subsections has focused on $D \geq 2$ dimensions, our main prediction of $N_\uparrow/N_\downarrow = \nu_\uparrow/\nu_\downarrow$ also holds in $D = 1$ dimension. Here the density of states in momentum is independent of the Fermi momentum, and so $\nu_\uparrow/\nu_\downarrow = 1$ for both balanced and imbalanced systems. This suggests that a Cooper pair instability with $N_\uparrow = N_\downarrow = 1$ should be energetically optimal for both balanced and imbalanced systems in $D = 1$ dimension. This is in agreement with both analytical predictions [192–194] and numerically exact calculations [195, 196] that show an FFLO phase constructed from Cooper pairs is the ground state throughout a large part of the phase diagram of one-dimensional Fermi gases.

5.2.11 Strongly-interacting limit

In the limit of strong attractive interactions $g \gg E_{\sigma\text{F}}$ we expect the system to promote particles to the energy of the up-spin Fermi surface to reconstruct full rotational symmetry, similar to a breached superconductor [130, 197, 198]. This turns the system effectively into one with balanced reconstructed Fermi surfaces, and so
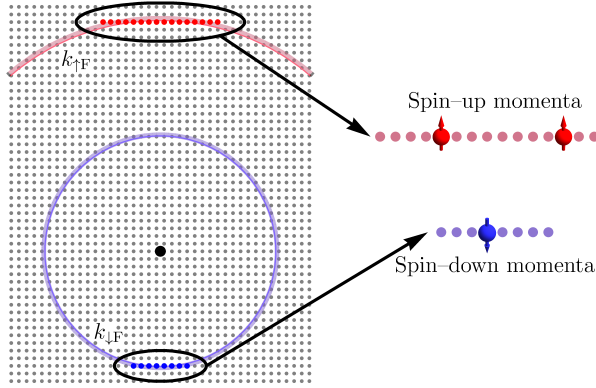
Figure 5.3: Example discretised momentum states (grey points) for use in exact diagonalisation calculations, showing up- and down-spin Fermi surfaces (red and blue curves) with a ratio of $\nu_\uparrow/\nu_\downarrow = 2$. The origin is marked by the large black point. The subsets of momentum states used in calculations are coloured and circled, in this case showing a $(L_\uparrow, L_\downarrow) = (16, 8)$ system. These states are shown larger, for clarity, on the right-hand side, with sample particle occupations.

supporting conventional Cooper pair instabilities. In the strongly-interacting limit of a many-body theory built from Cooper pairs, the pair coherence length becomes small on the scale of the separation between pairs, and so the pairs can be considered tightly-bound dimers [199, 200].

We have shown that the proposed multi-particle instability reduces to the well-studied Cooper problem in the balanced limit, and collapses to a pair instability in one dimension, which both link with previous results, and also reproduces a known result in the strongly-interacting limit. This gives us confidence that the multi-particle construction is also valid away from these limits. Having shown the strength of the formalism in reproducing these known limits, we now provide numerical evidence for the multi-particle instability being energetically optimal in a range of spin-imbalanced systems.

5.3 Exact diagonalisation

5.3.1 Method

In order to provide further insights into our conclusion that the optimal ratio of number of particles in an instability is given by $N_\uparrow/N_\downarrow = \nu_\uparrow/\nu_\downarrow$ we turn to a numerical evaluation of the wavefunction $|\psi\rangle$ and energy expectation value $\langle\psi|\hat{H}|\psi\rangle/\langle\psi|\psi\rangle$. To gain computational traction, we examine a reduced Hilbert space, taking only

finitely many momentum states from the Fermi surfaces. We indicate this reduction in Hilbert space size in Fig. 5.3, where instead of considering all momentum states (grey points) or even all momentum states on the up- and down-spin Fermi surfaces (red and blue curves), we use just linear subsets from opposite sides of the Fermi surfaces. This allows us to focus on the angular extent of the Fermi arcs, the driving force behind the emergence of the multi-particle instability. We work in the strongly interacting limit, to minimise the effect of neglecting the radial component of the sum over momentum. We use systems with $L_\uparrow$ momentum states for up-spin particles, and $L_\downarrow$ momentum states for down-spin particles: the ratio $L_\uparrow/L_\downarrow$ then mimics the ratio of densities of states in momentum $\nu_\uparrow/\nu_\downarrow$. Fig. 5.3 shows an example system with $(L_\uparrow, L_\downarrow) = (16, 8)$.

To numerically identify the ground state of the $(N_\uparrow, N_\downarrow)$ system of particles in a system with $(L_\uparrow, L_\downarrow)$ momentum states, we explicitly construct the $\binom{L_\sigma}{N_\sigma}$ combinations of particle momenta for each species, for a total of $\binom{L_\uparrow}{N_\uparrow} \times \binom{L_\downarrow}{N_\downarrow}$ basis states. Note that we do not explicitly include the additional constraint of the separation into Fermi surface arcs used in the wavefunction Eq. (5.2). We then directly evaluate and diagonalise the matrix of interactions between these states, with the optimal instability being that with the most negative eigenvalue.

5.3.2 Binding energy

We investigate the dependence of the optimal binding energy on the ratio of number of particles $N_\uparrow/N_\downarrow$ in the instability in Fig. 5.4, where we plot the normalised binding energy per critical species particle against the ratio of number of particles per species, normalised by the inverse ratio of number of momentum states. This rescaling of $N_\uparrow/N_\downarrow$ ensures that our predicted optimal binding energies are located at $N_\uparrow L_\downarrow/N_\downarrow L_\uparrow = 1$, as in Fig. 5.2. We examine systems with different ratios of numbers of momentum states $L_\uparrow/L_\downarrow \in \{1, 2, 3, 4\}$, with the lines in Fig. 5.4 coming from systems containing $(L_\uparrow, L_\downarrow) = (16, 16)$, $(L_\uparrow, L_\downarrow) = (16, 8)$, $(L_\uparrow, L_\downarrow) = (18, 6)$, and $(L_\uparrow, L_\downarrow) = (16, 4)$ momentum states respectively.

We observe that, as predicted by Eq. (5.9), the optimal binding energy per critical species particle for each ratio of number of momentum states is obtained with a ratio of number of particles of $N_\uparrow/N_\downarrow = L_\uparrow/L_\downarrow$. This is the principal result of our exact diagonalisation investigation: our numerical study reproduces the result
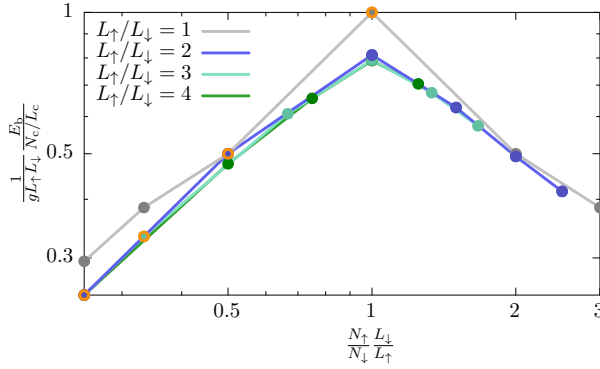
Figure 5.4: The normalised binding energy per critical species particle obtained using exact diagonalisation (lines), including the Cooper pair values (orange points).

of our approximate analytical method.

To highlight that Cooper pairs are suboptimal in spin-imbalanced systems, we indicate the Cooper pair instability for each system in Fig. 5.4 with orange circles, from left to right for the $L_\uparrow/L_\downarrow = 4$, $L_\uparrow/L_\downarrow = 3$, $L_\uparrow/L_\downarrow = 2$, and $L_\uparrow/L_\downarrow = 1$ systems. We note that for $L_\uparrow/L_\downarrow > 1$ these Cooper pair states have lower binding energy per critical species particle than the proposed multi-particle instability, whilst for $L_\uparrow = L_\downarrow$ the optimal multi-particle instability is simply a Cooper pair, as predicted by Cooper [172].

In Fig. 5.5 we confirm the convergence of our exact diagonalisation results with respect to system size for an example ratio $L_\uparrow/L_\downarrow = 2$. The different blue lines in Fig. 5.5 correspond to exact diagonalisation calculations of the binding energy using different numbers of up-spin particles, $N_\uparrow \in \{1, 2, 3, 4, 5\}$, and fixed $N_\downarrow = 1$. We observe a rapid convergence to the infinite size limit, with the $(L_\uparrow, L_\downarrow) = (16, 8)$ system shown in Fig. 5.3 giving results within 0.4% of the infinite size limit for the $N_\uparrow/N_\downarrow \in \{1, 2, 3\}$ ratios of numbers of particles. A slice through Fig. 5.5 at $L_\downarrow = 8$ gives the line for $L_\uparrow/L_\downarrow = 2$ in Fig. 5.4.

5.3.3   Fermi surface arcs

It is also illuminating to examine the wavefunctions of the energetically optimal instabilities. In Fig. 5.6 we show the basis states involved in the energetically optimal $(N_\uparrow, N_\downarrow) = (2, 1)$ instability of the $(L_\uparrow, L_\downarrow) = (14, 7)$ system. Each down-spin momentum state is part of a basis state with the two up-spin momentum states joined to it by lines of the same thickness and colour. Thicker lines indicate higher weighting (larger $\alpha(\mathbf{K}_\uparrow, \mathbf{K}_\downarrow)$) of the basis states, and colours represent the separation in

Figure 5.5: System size dependence of the binding energy per critical species particle, for ratio of number of momentum states $L_\uparrow/L_\downarrow = 2$. The different lines correspond to different ratios of numbers of particles in the instabilities.
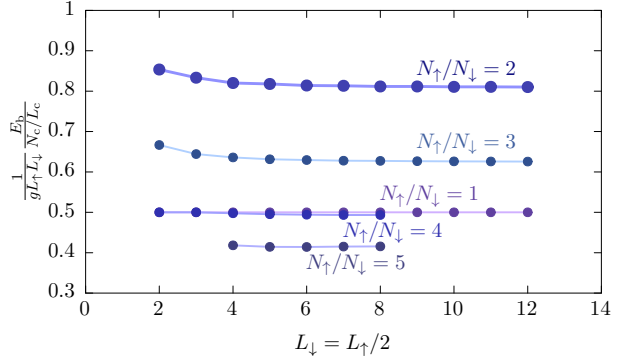
momentum between the up-spin species particles in the instability. The wavefunction comprises basis states that have spontaneously organised arcs of the up-spin Fermi surface: each plotted basis state has one up-spin particle in the left-hand half of the up-spin Fermi surface, and one particle in the right-hand half. This is in agreement with the use of arcs in the analytical wavefunction given by Eq. (5.2). In addition, the highest-weighted basis states are those at the angular centre of the arcs, which are the momenta labelled $\mathbf{q}_{\sigma i}$ in Section 5.2.

The separation of the wavefunction into Fermi surface arcs is also indicated by the integrated weights of the basis states at each momentum state, which are shown by the small points above the up-spin momentum states and below the down-spin momentum states in Fig. 5.6. The integrated weights for the up-spin particles show a bimodal distribution, indicating a separation into arcs. The black lines are symmetric fits to the data points, showing the arcs to contain identical distributions of integrated weights. As expected for an $N_\downarrow = 1$ system, the down-spin particle inhabits a single Fermi surface arc.

5.3.4 Instabilities with same ratio $N_\uparrow/N_\downarrow$

Exact diagonalisation may also be used to confirm the conclusion of Subsection 5.2.8 that instabilities with fewer total particles are marginally energetically favoured over instabilities with the same ratio $N_\uparrow/N_\downarrow$, but more particles. By examining the binding energy per particle of the simple $(N_\uparrow, N_\downarrow) = (1, 1)$ and $(N_\uparrow, N_\downarrow) = (2, 2)$ instabilities in balanced systems with $L_\uparrow = L_\downarrow = L$, we observe that the $(N_\uparrow, N_\downarrow) = (1, 1)$ instability does indeed have higher binding energy per particle at all finite interaction strengths. As predicted analytically [189], the difference scales as L^{-1} in
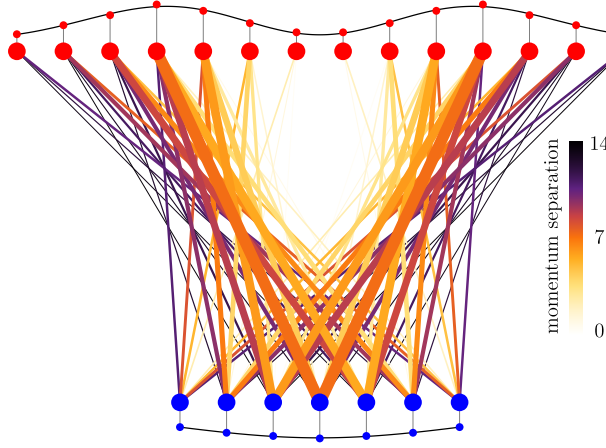
Figure 5.6: The weighting of basis states for the $(N_\uparrow, N_\downarrow) = (2, 1)$ instability of the $(L_\uparrow, L_\downarrow) = (14, 7)$ system. Coloured lines between the momentum states (represented by large red (up-spin) and blue (down-spin) points) indicate the basis states: each down-spin momentum state is part of a basis state with the two up-spin momentum states joined to it by lines of the same colour and thickness. Thicker lines indicate higher weighting (larger $\alpha(\mathbf{K}_\uparrow, \mathbf{K}_\downarrow)$) of the basis states; thinner lines indicate lower weighting. Color indicates the separation of the up-spin momentum states in each basis state, with yellow indicating small separation and purple large separation, with the colour key indicating the separation in number of momentum states. Only the 35 highest weighted basis states are shown for clarity. Above the up-spin momentum states and below the down-spin momentum states are the integrated weights of the basis states at each momentum state, indicating the separation of the momentum states into Fermi surface arcs.

the weakly-interacting limit, confirming the conclusion that instabilities with fewer total particles are energetically favourable in finite systems.

Our exact diagonalisation results on this simplified system have supported the main claims and conclusions of the analytical arguments in Section 5.2. The energetically optimal instability in a range of different spin-imbalanced systems has been shown to satisfy the relationship $N_\uparrow/N_\downarrow = L_\uparrow/L_\downarrow$ predicted in Eq. (5.9). The separation of the Fermi surface into arcs in the analytical wavefunction has also been justified by the emergence of such arcs in the numerical calculations, and we have provided evidence for which instabilities with the same ratio $N_\uparrow/N_\downarrow$ are most energetically favourable.

5.4   Discussion

We have shown that spin-imbalanced Fermi gases with attractive interactions support a multi-particle instability. The most energetically favourable instability contains up- and down-spin particles in the ratio $N_\uparrow/N_\downarrow = \nu_\uparrow/\nu_\downarrow$, set by the ratio of the densities of states in momentum at the Fermi surfaces.

The proposed trial wavefunction for the multi-particle instability interpolates between the well-known Cooper wavefunction [172] in the limit of balanced Fermi surfaces and theoretical predictions [192–194] of the FFLO phase in one dimension. This lends support to the contention that our trial wavefunction is also valid away from these limits.

We note that the physics presented here can be explored in few-body systems, as even single-digit numbers of particles can exhibit collective phenomena such as the Fermi surfaces examined in this Chapter [201]. Cold atoms in an harmonic trap [118, 202] are an ideal system to explore few-particle physics, as the exact energy and expectation values such as the wavefunction symmetry may be directly measured [78, 201]. Cold atom experiments may therefore be able to observe the scaling of the binding energy and spatial structure of the trial wavefunction proposed here, of which hints may previously have been seen numerically [201].

In real experiments the interaction between fermions will never be exactly the contact interaction from Eq. (5.1). In cold atom systems the interaction may be expanded as $g(1 + 8aR_{\text{eff}}k_{\text{F}}^2)$, where $a < 0$ is the scattering length and R_{eff} is the effective range [148]. Positive R_{eff} reduces the effective interaction strength, making

the multi-particle instability less energetically favourable, whilst negative R_{eff} makes it more energetically favourable; however, $|R_{\mathrm{eff}}|$ is typically small on the scale of $1/k_{\mathrm{F}}$, and so the effect of the finite range interaction is also small. The screened Coulomb interaction, $g/(1 + 2b^2 k_{\mathrm{F}}^2)$ where $b > 0$ is the Thomas-Fermi screening length, relevant for example to electron-hole systems [203, 204], has a similar effect, with the screening length taking on the same role as the effective range for cold-atom interactions, and so weakening the multi-particle instability relative to the purely-contact case. This weakening is also found in standard Cooper pairs, however, and so is unlikely to qualitatively change the conclusions of this Chapter. The next order term in the effective range expansion would go as $R_{\mathrm{eff}} k_{\mathrm{D}}$: this term will discriminate between multi-particle instabilities and Cooper pairs, being a function of how many fermions near the Fermi surfaces are involved in the instability, but is not expected to have a large effect, as in our formalism both k_{D} and R_{eff} are small.

In the same way that Cooper pairs form the conceptual basis of the Bardeen–Cooper–Schrieffer theory of superconductivity, it is expected that a many-body state may be constructed using the multi-particle instabilities presented here with even values of $N_\uparrow + N_\downarrow$. By analogy to the relationship between the traditional Cooper result and the BCS order parameter, we expect that the order parameter of the future many-body superconducting theory should have a form that is reminiscent of Eq. (5.8). The many-body theory should not be limited to including a single type of multi-particle instability, and similarly to predictions made for the FFLO phase [176] may be constructed from multiple superposed multi-particle instabilities, forming a crystalline structure.

A natural tool to use to search for this exotic superconducting state is a spin-imbalanced ultracold fermionic gas [205, 206]. This system allows fine control over the populations and interactions of the fermions, allowing experiments to focus on the potential of new physics. Previous spin-imbalanced ultracold fermionic gas experiments have used inhomogeneous optical trapping potentials, in which the region of space where multi-particle instability-based superconductivity is likely to be observable is very small. However, recent experimental developments have allowed the creation of homogeneous ultracold fermionic gases [207], where the delicate novel superconducting state is likely to exist over larger regions of space, and so be easier to observe and characterise.

Such a strongly correlated state would present novel superconducting proper-

ties, including unusual Andreev reflection [208], Josephson tunnelling [209], and SQUID [210] or other superconducting loop [211] properties, due to the underlying multi-particle structure. With the underlying instabilities involving $N_\uparrow + N_\downarrow$ fermions, magnetic flux is likely to be quantised in units of $h/(N_\uparrow + N_\downarrow)e$, rather than $h/2e$ for BCS superconductivity based on Cooper pairs. The superconducting order parameter would also exhibit unusual behaviour, being necessarily complex due to the presence of non-antipodal q-vectors, and oscillating with wavevectors $\mathbf{q}_{\uparrow i} + \mathbf{q}_{\downarrow j}$, with interference due to similar q-vectors giving rise to beats in the order parameter amplitude. The existence of a superconducting state constructed from multi-particle instabilities may also explain the lack of definitive observations of the conjectured FFLO state.

Data used for this Chapter are available online [212].

Chapter 6

Multi-particle theory of superconductivity

A spin-imbalanced Fermi gas with an attractive contact interaction forms a superconducting state whose underlying components are multi-particle instabilities, each involving more than two fermions. As this multi-particle superconducting state includes correlations between all available fermions it is energetically favourable to Fulde–Ferrell–Larkin–Ovchinnikov superconductivity, as we demonstrate using a Ginzburg–Landau method. The ratio of the number of up- and down-spin fermions in the instability is a function of the ratio of the up- and down-spin densities of states in momentum at the Fermi surfaces, to fully utilise the accessible fermions.

6.1   Introduction

For over a century, the phenomenon of superconductivity has captured the attention of theorists, who have provided fundamental revelations about its underlying principles. Bardeen, Cooper, and Schrieffer (BCS) [42,43] gave seminal insights into the mechanism of superconductivity in systems with spin-balanced Fermi surfaces, showing that superconductivity may be understood as the collective behaviour of coherent Cooper pairs of fermions, as discussed in Section 1.3.2. Fulde, Ferrell, Larkin, and Ovchinnikov (FFLO) [173,174] extended this result, demonstrating that even in systems with spin-imbalanced Fermi surfaces Cooper pairs may still form the basis of a superconducting state. However, in spin-imbalanced systems, the density of states in momentum at the Fermi surface of the majority-spin fermions is greater than that of the minority-spin fermions, so the number of Cooper pairs that can exist is limited by the number of minority-spin fermions at their Fermi surface. This leaves many of the majority-spin fermions unpaired and so uncorrelated, wasting their potential for contributing correlation energy to the system.

In a few-particle context, the multi-particle instabilities discussed in Chapter 5 and Ref. [213], generalisations of a Cooper pair containing more than two fermions, have been shown to maximise the correlation energy captured in spin-imbalanced systems by taking advantage of the correlations between all available momentum states. Such a multi-particle instability is shown in Fig. 6.1, showing three majority- (up-)spin fermions involved in an instability with one minority- (down-)spin fermion. The favourable binding energy of the multi-particle instability makes it the ideal building block for constructing a superconducting state. In this Chapter we show that this superconducting state is energetically favourable over Cooper pair-based FFLO superconductivity in spin-imbalanced systems.

Current experimental developments enable the study of exotic phases of matter with unprecedented levels of accuracy. Spin-imbalanced Fermi gases can be realised in solid-state materials [177–181], and spin-orbit coupling may also give rise to inhomogeneous superconductivity [29,30], but no single experiment has provided unambiguous evidence for the existence of FFLO superconductivity, leaving the true nature of the ground state an open question. The recent development of uniform trapping potentials for ultracold atomic gases [207] presents an ideal opportunity to revisit the structure of the superconducting ground state of spin-imbalanced Fermi

Figure 6.1: (Color online) Idealised representation of the spin-imbalanced system showing Fermi surfaces for the down- (light blue circle) and up-spin (fragment of light red circle) species, with occupiable momentum states extending over a momentum scale set by the Debye frequency, forming annuli. Areas with more intense colour in the annuli indicate the approximate occupation of momentum states. Also shown are the momenta of $(N_\uparrow, N_\downarrow) = (3,1)$ up- and down-spin fermions with corresponding q-vectors $\mathbf{q}_{\sigma i}$.
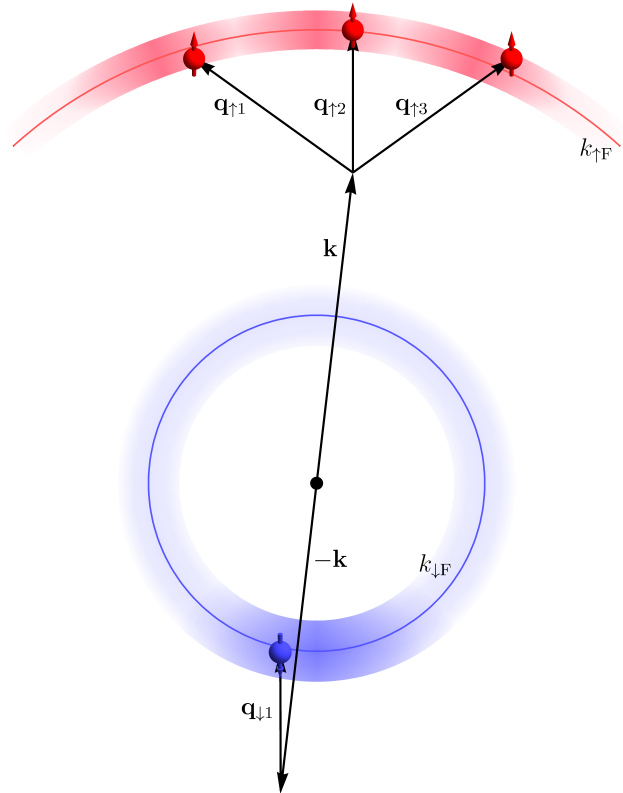
gases.

In this Chapter we examine the ratio of number of majority- to minority-spin fermions in the instability underlying the superconducting state in a spin-imbalanced Fermi gas, and compare the energetics of multi-particle superconductivity favourably to those of FFLO superconductivity. We also discuss the unique experimental consequences of the proposed multi-particle superconductor.

6.2   Theory

To explore the possibility of multi-particle superconductivity we examine a two-spin fermionic system with an attractive contact interaction. The quantum partition function, $\mathcal{Z} = \int \mathcal{D}(\psi, \bar{\psi}) \mathrm{e}^{-S[\psi,\bar{\psi}]}$, depends upon the BCS action

$$S[\psi, \bar{\psi}] = \sum_{\omega, \mathbf{k}, \sigma} \bar{\psi}_{\mathbf{k},\sigma}(-i\omega + \xi_{\mathbf{k},\sigma})\psi_{\mathbf{k},\sigma} - g \sum_{\omega, \mathbf{k}, \mathbf{k}', \mathbf{q}} \bar{\psi}_{\mathbf{k},\uparrow}\bar{\psi}_{\mathbf{q}-\mathbf{k},\downarrow}\psi_{\mathbf{q}-\mathbf{k}',\downarrow}\psi_{\mathbf{k}',\uparrow},$$

where $\psi_{\mathbf{k},\sigma}$ and $\bar{\psi}_{\mathbf{k},\sigma}$ are a fermion field and its Grassmann conjugate, for momentum $\mathbf{k}$ and spin species $\sigma \in \{\uparrow, \downarrow\}$, $\xi_{\mathbf{k},\sigma}$ is the species-dependent dispersion, $g > 0$ is the strength of the attractive contact interaction, and ω is a fermionic Matsubara frequency. In this expression the momenta $\mathbf{q}$, referred to henceforth as q-vectors, give the net momentum of coupled fermions. We perform a Hubbard-Stratonovich decoupling in the Cooper channel, using a concise matrix formalism to express the action as

$$S[\psi, \bar{\psi}, \Delta, \Delta^*] = \sum_{\omega, \mathbf{k}} \begin{pmatrix} \bar{\psi}_\uparrow \\ \psi_\downarrow \end{pmatrix}^{\mathrm{T}} \begin{pmatrix} \boldsymbol{\mathcal{G}}_\uparrow^{-1} & -\boldsymbol{\Delta} \\ -\boldsymbol{\Delta}^\dagger & \boldsymbol{\mathcal{G}}_\downarrow^{-1} \end{pmatrix} \begin{pmatrix} \psi_\uparrow \\ \bar{\psi}_\downarrow \end{pmatrix} + \sum_\omega \frac{\mathrm{Tr}\left(\boldsymbol{\Delta}^\dagger \boldsymbol{\Delta}\right)}{g}, \qquad (6.1)$$

where the vectors $\boldsymbol{\psi}_\sigma = (\psi_{(\mathbf{q}_{\sigma 1} + \varsigma_\sigma \mathbf{k}),\sigma}, \psi_{(\mathbf{q}_{\sigma 2} + \varsigma_\sigma \mathbf{k}),\sigma}, \ldots)^{\mathrm{T}}$, with $\varsigma_\uparrow = +1$ and $\varsigma_\downarrow = -1$, the Grassmann conjugates $\bar{\boldsymbol{\psi}}_\sigma$ are similar, the matrices $\boldsymbol{\mathcal{G}}_\sigma^{-1} = \mathrm{diag}(\mathcal{G}_{(\mathbf{q}_{\sigma 1} + \varsigma_\sigma \mathbf{k}),\sigma}^{-1}, \mathcal{G}_{(\mathbf{q}_{\sigma 2} + \varsigma_\sigma \mathbf{k}),\sigma}^{-1}, \ldots)$, for $\mathcal{G}_{\mathbf{p},\sigma}^{-1} = -i\omega + \varsigma_\sigma \xi_{\mathbf{p},\sigma}$, and

$$\boldsymbol{\Delta} = \begin{pmatrix} \Delta_{\mathbf{q}_{\uparrow 1} + \mathbf{q}_{\downarrow 1}} & \Delta_{\mathbf{q}_{\uparrow 1} + \mathbf{q}_{\downarrow 2}} & \cdots \\ \Delta_{\mathbf{q}_{\uparrow 2} + \mathbf{q}_{\downarrow 1}} & \Delta_{\mathbf{q}_{\uparrow 2} + \mathbf{q}_{\downarrow 2}} & \cdots \\ \vdots & \vdots & \ddots \end{pmatrix},$$

where the $\mathbf{q}_{\sigma i}$ run over all the q-vectors of species σ. We label the number of fermions, and hence the number of q-vectors, per species by N_σ: therefore the $\boldsymbol{\mathcal{G}}_\sigma^{-1}$ are $N_\sigma \times N_\sigma$ matrices and $\boldsymbol{\Delta}$ is an $N_\downarrow \times N_\uparrow$ matrix. We shall find that in spin-imbalanced systems $N_\uparrow \neq N_\downarrow$, indicating that $\boldsymbol{\Delta}$ is rectangular rather than square, so that different numbers of fermions from each species are involved in the underlying instability. However, in common with the few-particle analysis in Chapter 5, the quadratic form of Eq. (6.1) in fermion fields ensures that fermions only couple pairwise. In the system represented by Fig. 6.1, where there are three up-spin and one down-spin fermions involved in the underlying instability, $\boldsymbol{\Delta}$ would be a 1×3 matrix.

The elements of the $\boldsymbol{\Delta}$ matrix gap the dispersion. For single-plane-wave FFLO superconductivity [173] $\boldsymbol{\Delta}$ has only a single entry, and for crystalline FFLO superconductivity [175, 176] it is diagonal. The non-diagonal form here allows multi-particle superconductivity, as the fermion pairing is not exclusive, with the underlying instability consisting of $N_\uparrow N_\downarrow$ pairs that share fermions. We focus on superconductivity built from a single multi-particle instability, where $\boldsymbol{\Delta}$ is not block-diagonalisable, and which is comparable to single-plane-wave FFLO superconductivity. For simplicity of analysis we assume that none of the $\mathbf{q}_{\uparrow i} + \mathbf{q}_{\downarrow j}$ pairs of q-vectors in $\boldsymbol{\Delta}$ are degenerate. Following Chapter 5 the $\mathbf{q}_{\sigma i}$ vectors are taken to be sufficiently different from each other that each $\psi_{\mathbf{p},\sigma}$ appears at most once in Eq. (6.1).

With this expression for the action, working in the mean-field approximation we can carry out a Ginzburg-Landau expansion of the regularised thermodynamic potential $\Omega = -T \ln \mathcal{Z}$, where T is the temperature, to obtain

$$\Omega = T \sum_{\omega,\mathbf{k}} \sum_{n=1}^{\infty} \frac{1}{n} \mathrm{Tr}\left(\boldsymbol{\mathcal{G}}_\uparrow \boldsymbol{\Delta} \boldsymbol{\mathcal{G}}_\downarrow \boldsymbol{\Delta}^\dagger\right)^n + \frac{\mathrm{Tr}\left(\boldsymbol{\Delta}^\dagger \boldsymbol{\Delta}\right)}{g}.$$

To make progress with this expression, we symmetrise the coupling amplitudes, $\Delta_\mathbf{q} = \Delta$. Near to the second-order transition to the normal state we may neglect the effect of high-order terms in Δ, allowing us to truncate the expression for the thermodynamic potential to

$$\Omega = \alpha \Delta^2 + \frac{1}{2}\beta \Delta^4 + \dots, \tag{6.2}$$

where

$$\alpha = \sum_{\mathbf{q}_\uparrow, \mathbf{q}_\downarrow} \left(\frac{1}{g} + T \sum_{\omega, \mathbf{k}} \mathcal{G}_{\mathbf{q}_\uparrow + \mathbf{k}, \uparrow} \mathcal{G}_{\mathbf{q}_\downarrow - \mathbf{k}, \downarrow} \right),$$

$$\beta = T \sum_{\substack{\mathbf{q}_{\uparrow 1}, \mathbf{q}_{\downarrow 1}, \\ \mathbf{q}_{\uparrow 2} \, \mathbf{q}_{\downarrow 2}}} \sum_{\omega, \mathbf{k}} \mathcal{G}_{\mathbf{q}_{\uparrow 1} + \mathbf{k}, \uparrow} \mathcal{G}_{\mathbf{q}_{\downarrow 1} - \mathbf{k}, \downarrow} \mathcal{G}_{\mathbf{q}_{\uparrow 2} + \mathbf{k}, \uparrow} \mathcal{G}_{\mathbf{q}_{\downarrow 2} - \mathbf{k}, \downarrow}.$$

To evaluate these expressions, we focus on a two-dimensional system where we expect multi-particle superconductivity to be most energetically favourable over FFLO superconductivity. We also specialise to the case of small Debye frequency, found for many conventional superconductors [183–185], where the vectors $\mathbf{q}_{\sigma i}$ are all expected to be approximately parallel. This enables us to factorise out combinatorial factors, giving

$$\alpha = N_\uparrow N_\downarrow \left(\frac{1}{g} + T \sum_{\omega, \mathbf{k}} \mathcal{G}_{\mathbf{q} + \mathbf{k}, \uparrow} \mathcal{G}_{\mathbf{q} - \mathbf{k}, \downarrow} \right),$$

$$\beta = N_\uparrow N_\downarrow \big[J_0 + (N_\uparrow - 1) J_\uparrow + (N_\downarrow - 1) J_\downarrow + (N_\uparrow - 1)(N_\downarrow - 1) J_{\uparrow\downarrow} \big], \qquad (6.3)$$

where $\quad J_0 = J(\mathbf{q}, \mathbf{q}, \mathbf{q}, \mathbf{q}), \qquad\qquad J_\uparrow = J(\mathbf{q} + \delta\mathbf{q}_\uparrow, \mathbf{q}, \mathbf{q} - \delta\mathbf{q}_\uparrow, \mathbf{q}),$
$J_\downarrow = J(\mathbf{q}, \mathbf{q} + \delta\mathbf{q}_\downarrow, \mathbf{q}, \mathbf{q} - \delta\mathbf{q}_\downarrow), \quad$ and $\quad J_{\uparrow\downarrow} = J(\mathbf{q} + \delta\mathbf{q}_\uparrow, \mathbf{q} + \delta\mathbf{q}_\downarrow, \mathbf{q} - \delta\mathbf{q}_\uparrow, \mathbf{q} - \delta\mathbf{q}_\downarrow),$
with

$$J(\mathbf{q}_1, \mathbf{q}_2, \mathbf{q}_3, \mathbf{q}_4) = T \sum_{\omega, \mathbf{k}} \mathcal{G}_{\mathbf{q}_1 + \mathbf{k}, \uparrow} \mathcal{G}_{\mathbf{q}_2 - \mathbf{k}, \downarrow} \mathcal{G}_{\mathbf{q}_3 + \mathbf{k}, \uparrow} \mathcal{G}_{\mathbf{q}_4 - \mathbf{k}, \downarrow}. \qquad (6.4)$$

In the expressions J_x, $\mathbf{q}$ is taken to represent the average q-vector for the fermions, symmetrised between species, and $\delta\mathbf{q}_\sigma$ is half the average separation between q-vectors for species σ, which in the small Debye frequency limit is orthogonal to the vector $\mathbf{q}$. Following the method of Ref. [176], for a free dispersion the function $J(\mathbf{q}_1, \mathbf{q}_2, \mathbf{q}_3, \mathbf{q}_4)$ may be evaluated at zero temperature as detailed in Appendix D, to give

$$J(\mathbf{q}_1, \mathbf{q}_2, \mathbf{q}_3, \mathbf{q}_4) = \frac{\mathcal{N}}{4\delta\mu^2} \mathrm{Re} \int_0^1 \frac{\mathrm{d}x\mathrm{d}y}{\left[1 - \left(\frac{|\mathbf{q}_1(x-1) + \mathbf{q}_2(y-x) - \mathbf{q}_3 y| k_\mathrm{F}}{\delta\mu} \right)^2 \right]^{3/2}}, \qquad (6.5)$$

where $\mathcal{N}$ is the density of states in energy, $\delta\mu = (k_{\uparrow\mathrm{F}}^2 - k_{\downarrow\mathrm{F}}^2)/4$ is the chemical potential difference between the species, $k_{\mathrm{F}} = (k_{\uparrow\mathrm{F}} + k_{\downarrow\mathrm{F}})/2$ is the average Fermi momentum, and $k_{\sigma\mathrm{F}}$ is the Fermi momentum of species σ. Eq. (6.5) confirms that for a single instability $\beta \geq 0$, justifying the truncation in Eq. (6.2).

We wish to identify the optimal ratio of number of fermions involved in the multi-particle superconductor, which for FFLO superconductivity would be unity. To demonstrate that the optimal ratio of number of fermions involved in the multi-particle superconductor differs from unity, we express Eq. (6.2) as a function of $N_\uparrow/N_\downarrow$ and $N_\uparrow N_\downarrow$, and then optimise Ω with respect to $N_\uparrow/N_\downarrow$, $N_\uparrow N_\downarrow$, and Δ simultaneously. This gives the expected ratio of number of fermions involved in the underlying instability as

$$\frac{N_\uparrow}{N_\downarrow} = \frac{J_{\uparrow\downarrow} - J_\downarrow}{J_{\uparrow\downarrow} - J_\uparrow} = \left(\frac{|\delta\mathbf{q}_\uparrow|}{|\delta\mathbf{q}_\downarrow|}\right)^2, \tag{6.6}$$

where the last equality was obtained from Eq. (6.5) through substitution of the evaluated forms of the J_x expressions.

To put this expression in terms of physical parameters, we follow the prescription of Chapter 5 that the angular widths of the regions of Fermi surface involved in the multi-particle superconducting state are the same between species, and so $|\delta\mathbf{q}_\uparrow|/k_{\uparrow\mathrm{F}} = |\delta\mathbf{q}_\downarrow|/k_{\downarrow\mathrm{F}}$. Therefore $|\delta\mathbf{q}_\uparrow|/|\delta\mathbf{q}_\downarrow| = k_{\uparrow\mathrm{F}}/k_{\downarrow\mathrm{F}} = \nu_\uparrow/\nu_\downarrow$, where $\nu_\sigma = 2\pi k_{\sigma\mathrm{F}}$ is the density of states in momentum at the Fermi surface of species σ in two dimensions, and so

$$\frac{N_\uparrow}{N_\downarrow} = \left(\frac{\nu_\uparrow}{\nu_\downarrow}\right)^2. \tag{6.7}$$

This result confirms that the superconducting state is indeed formed from a multi-particle instability to take advantage of all available correlations in spin-imbalanced systems, as $\nu_\uparrow/\nu_\downarrow \neq 1$ in a spin-imbalanced Fermi gas. Eq. (6.7) also aligns with our heuristic expectation that the instability involves more fermions of the species with the larger density of states in momentum at its Fermi surface, as was also found in the few-particle case in Chapter 5. The particular value of 2 in the exponent comes from the dispersion used in this analysis, and other values for the exponent (always greater than 1) are obtained with different dispersions. For spin-balanced systems,

$\nu_\uparrow = \nu_\downarrow$ and so $N_\uparrow/N_\downarrow = 1$, recovering the BCS theory result, whilst in the polaron limit of a single minority-spin impurity in a full Fermi sea of majority-spin fermions, the single minority-spin fermion couples with all the majority-spin fermions at their Fermi surface, in agreement with results from the literature [214, 215].

The same optimisation procedure that gave Eq. (6.6) for the ratio $N_\uparrow/N_\downarrow$ also provides an expression for the product $N_\uparrow N_\downarrow$, as

$$N_\uparrow N_\downarrow = \frac{(J_0 - J_\uparrow - J_\downarrow + J_{\uparrow\downarrow})^2}{(J_{\uparrow\downarrow} - J_\uparrow)(J_{\uparrow\downarrow} - J_\downarrow)}. \tag{6.8}$$

For reasonable values of the $|\delta\mathbf{q}_\sigma|$ and $|\mathbf{q}|$ in spin-imbalanced systems this expression gives values of $N_\uparrow N_\downarrow > 1$, confirming that the multi-particle superconductor is indeed made up of multiple fermions of at least one spin species. Excessively high $N_\uparrow N_\downarrow$ is energetically penalised by the highest term in the expansion of the thermodynamic potential, which goes as $(N_\uparrow N_\downarrow \Delta^2)^n$, and so we expect multi-particle superconductivity to have both N_σ being reasonably small integers. In the spin-balanced limit Eq. (6.8) collapses to the BCS result $N_\uparrow N_\downarrow = 1$.

Now that we have shown that the multi-particle superconductor is energetically favourable over single-plane-wave FFLO superconductivity in a spin-imbalanced Fermi gas, we need to confirm that we have not compromised the stability of the superconducting state. We validate this by examining the phase boundaries between the multi-particle superconductor and three competitor phases.

With increasing spin-imbalance, BCS superconductivity becomes unstable against FFLO superconductivity at the Chandrasekhar-Clogston limit [216, 217]. Although multi-particle superconductivity is energetically favourable over FFLO superconductivity, BCS superconductivity still has a large density-of-states advantage over multi-particle superconductivity, and to a first approximation the phase boundary between BCS superconductivity and multi-particle superconductivity will remain at the same Chandrasekhar-Clogston value.

The phase boundary between multi-particle superconductivity and the normal state will also remain the same as between single-plane-wave FFLO superconductivity and the normal state. In both cases the second-order phase transition occurs when $\alpha = 0$, and this condition is identical between FFLO and multi-particle superconductivity, up to the irrelevant multiplicative factor of $N_\uparrow N_\downarrow$ in Eq. (6.3), and so the phase boundary is also identical.

Stability against phase separation can be expressed as the positive-definiteness of the total particle number susceptibility matrix [218, 219]. This condition includes the possibility of separation into two superconducting phases, with ratios of number of fermions differing from that predicted in Eq. (6.6), and may be expanded following Eq. (6.2), to leading order in Δ giving

$$\alpha \frac{\partial^2 \alpha}{\partial q^2} > 2 \left(\frac{\partial \alpha}{\partial q} \right)^2 .$$

This is the same as the equivalent expression for FFLO superconductivity, up to a factor of $(N_\uparrow N_\downarrow)^2$ that cancels between the two sides of the inequality. This indicates that the line of stability against phase separation is the same for multi-particle superconductivity as for FFLO superconductivity to leading order.

6.3 Discussion

Having seen that multi-particle superconductivity is energetically favourable over FFLO superconductivity, and fills the same region of the phase diagram of imbalanced Fermi gases, we now consider its possible experimental consequences. We focus on two effects where the multi-particle nature of the underlying instability should be directly observable.

Multiple phase transitions: With increasing spin-imbalance, Eq. (6.7) predicts that the ratio $N_\uparrow/N_\downarrow$ should increase. Starting from the BCS state with $N_\uparrow/N_\downarrow = 1$ the system should progress through multi-particle superconductors with increasing values of $N_\uparrow/N_\downarrow$, where both N_σ are reasonably small integers, giving a series of different superconducting states. Each transition is expected to be second order, and so the multi-particle superconducting phase would be characterised by a series of divergences in the heat capacity. This effect could be measured by changing the population imbalance between different realisations of an ultracold atomic gas experiment.

Superconducting order parameter: In real space the order parameter, the phase-weighted sum of the $\Delta_{\mathbf{q}}$, will exhibit a beat pattern due to the interference

between similar q-vectors, which could allow the identification of the particular q-vectors in the underlying multi-particle instability. The order parameter could be determined in an ultracold atomic gas experiment through density-density correlations measured from time-of-flight experiments [220].

Beyond these experimental signatures, multi-particle superconductivity also introduces the notion that the number of fermions in the building block of a superconductor is not fixed at two. In particular, there can be fluctuations in the number of fermions in the underlying instability, which could lead to the renormalisation of the properties of a spin-balanced superconductor. Although the discussion above focusses on single multi-particle instabilities as the basis of multi-particle superconductivity, comparable to single-plane-wave FFLO superconductivity, the analysis is generalisable to systems more akin to crystalline FFLO superconductivity [176]. We take crystalline FFLO superconductivity as a guide for the likely modifications when multi-particle superconductivity is built from several instabilities.

In this Chapter we have introduced the idea of a multi-particle superconductor, whose underlying instability is composed of more than two fermions to facilitate the use of all available inter-particle correlations. We have shown that multi-particle superconductivity is energetically favourable over FFLO superconductivity in spin-imbalanced Fermi gases, exists throughout a similar portion of the phase diagram, and that the multi-particle instability underlying this novel form of superconductivity should give clear experimental signatures.

Chapter 7

Conclusion

This Thesis has developed multiple facets of the field of interacting Fermi gases. In Part I, the focus was on developing new approaches to computational methods for studying interacting Fermi gases using quantum Monte Carlo methods. The development in Chapter 2 of a pseudopotential for the two-dimensional dipolar interaction has opened up the possibility of examining the phase diagram of the homogeneous dipolar gas in more detail than was previously attainable, potentially gaining more insight into the speculative stripe phase [48] that has been predicted analytically but never observed numerically or experimentally. The pseudopotential formalism itself is also open to more development; this Thesis has furthered the development of ultra-transferable pseudopotentials, which in Chapter 3 were shown to be much more accurate in capturing the pathological two-dimensional contact interaction than more well-established alternatives. Further develoments of the pseudopotential formalism are certainly possible, however: the true, physical, interaction between particles in an ultracold atomic gas is not the contact interaction, but the more complex Feshbach resonance interaction. It will be possible to construct pseudopotentials for the Feshbach resonance, including the effects of high-order scattering properties, and indeed the first steps have already been taken in this direction [221, 222].

Chapter 4 continued the theme of accelerating numerical simulations by proposing a new form of Jastrow correlation factor, which interpolates between the physical symmetry of a Coulomb interparticle interaction and the imposed symmetry of the simulation cell. Beyond being more conceptually elegant than existing alternatives, not having a need for hard cutoffs to account for finite simulation cell sizes, the pro-

posed Jastrow factor reduces the parameter space to be explored when optimising simulations and is quicker to evaluate than other similar expressions. These properties make it attractive for taking forwards into a whole range of quantum Monte Carlo simulations, where is will simplify the life of the simulation-runner, and it also lays the groundwork for a new way of thinking about parameters in simulation cells: all physical coordinates can be re-expressed in terms of variables that hold the symmetry of the simulation cell, to bind the simulation to its cell more tightly. This could be of particular use in modelling periodic effects with large amplitudes compared to the simulation cell size, as found for example in the modelling of large-amplitude phonons in density functional theory.

The focus in the second Part of this Thesis was slightly different, identifying a possible new phase of superconducting matter in a particular type of interacting Fermi gas, a spin-imbalanced gas with attractive contact interactions. In Chapter 5 an instability was identified in this system towards the formation of multi-particle instabilities, generalisations of the famous Cooper pair. Chapter 5 used both analytic and numerical methods to determine that these multi-particle instabilities are the energetically favourable instability in spin-imbalanced Fermi gases, opening up a new paradigm of superconductivity formed from multiple interacting fermions. The first development of this theory was expounded in Chapter 6, where an analysis of the energy of the superconducting state confirmed the suspicion that involving more degrees of freedom in the underlying instability should improve the energy of the macroscopic state. This Chapter also suggested some experimental signatures of the multi-particle superconducting phase, in particular those that should be easily observable in current-generation ultracold atomic gas experiments. Nevertheless, Chapter 6 was only the first stage of development of this theory, and future refinements are sure to come. As of the time of writing, numerical simulations are being carried out (using pseudopotentials akin to those from Chapter 3 and the ν Jastrow factor from Chapter 4) to try to distinguish the multi-particle superconducting phase, with first results that appear promising. Beyond the particular superconducting theory developed in Chapter 6, the underlying concept of phases built from multiple particles rather than the pairs that couple directly in the Hamiltonian should be widely applicable to other areas of physics, with analogous derivations.

These are the results of this Thesis; developments in the theoretical analysis

of interacting Fermi gases, some incremental and others hopefully more substantial, which are already forming the basis of new and exciting discoveries, with future opportunities abound. From avoiding numerical pathologies to suggesting new paradigms of superconductivity, this Thesis will hopefully provide some inspiration or support to the next generation of physicists, making up but one step on the ever-growing ladder of understanding that supports them.

Appendices

Appendix A

Construction of the Troullier–Martins pseudopotentials

The Troullier–Martins formalism is a method for developing pseudopotentials that were originally designed for use in electron-ion calculations [68]. Here, following Reference [61] we adapt it to the case of a 2D dipolar potential. The scattering Schrödinger Equation (2.1) may be written in 2D circular coordinates (r, ϕ) as

$$-\left(\frac{1}{r}\frac{\partial}{\partial r}\left(r\frac{\partial}{\partial r}\right) + \frac{1}{r^2}\frac{\partial^2}{\partial \phi^2}\right)\psi(r,\phi) + V(r)\psi(r,\phi) = E\psi(r,\phi),$$

where we wish to replace the dipolar potential $V(r) = d^2/r^3$ with a pseudopotential inside a cutoff radius $r_{\rm c}$. Expanding the wavefunction in angular momentum channels as

$$\psi(r,\phi) = \sum_{\ell=0}^{\infty} r^\ell \psi_\ell(r)\cos(\ell\phi)$$

we obtain a radial equation for the wavefunction ψ_ℓ in each channel

$$-\left(\frac{2\ell+1}{r}\psi'_\ell + \psi''_\ell\right) + V(r)\psi_\ell = E\psi_\ell,\qquad\text{(A.1)}$$

where the primes indicate differentiation with respect to r. We choose a calibration energy E_c at which the pseudopotential will exactly replicate the dipolar potential's scattering characteristics, whose optimal choice is found in Appendix B to be $E_F/4$. We then construct the pseudopotential by working from a pseudo-wavefunction that within a radius r_c takes the form

$$\psi_{\mathrm{pseudo},\ell}(r) = e^{p(r)},$$

where $p(r) = \sum_{i=0}^{6} c_i r^{2i}$. The form $e^{p(r)}$ is positive definite, which ensures that no spurious nodes are introduced into the wavefunction. Inserting the wavefunction into Eq. (A.1) we find that the pseudopotential in each angular momentum channel ℓ should take the form

$$V_{\mathrm{T-M}}(r) = \begin{cases} E_c + \frac{2\ell+1}{r}p' + p'^2 + p'', & r < r_c, \\ d^2/r^3, & r \geq r_c. \end{cases} \tag{A.2}$$

In order to calculate $p(r)$ explicitly we impose a series of constraints on it: firstly, that the pseudo-wavefunction's value and first four derivatives match those of the exact wavefunction at r_c, in order that the first two derivatives of the pseudopotential are continuous,

$$p(r_c) = \ln\left(\frac{R_\ell(r_c)}{r_c^{\ell+1}}\right),$$

$$p'(r_c) = \frac{R_\ell'(r_c)}{R_\ell(r_c)} - \frac{\ell+1}{r_c},$$

$$p''(r_c) = V(r_c) - E_c - (p'(r_c))^2 - \frac{2\ell+1}{r_c}p'(r_c),$$

$$p'''(r_c) = V'(r_c) - 2p'(r_c)p''(r_c) - \frac{2\ell+1}{r_c}p''(r_c) + \frac{2\ell+1}{r_c^2}p'(r_c),$$

$$p''''(r_c) = V''(r_c) - 2(p''(r_c))^2 - 2p'(r_c)p'''(r_c)$$
$$- \frac{2\ell+1}{r_c}p'''(r_c) + 2\frac{2\ell+1}{r_c^2}p''(r_c) - 2\frac{2\ell+1}{r_c^3}p'(r_c),$$

where $R_\ell(r) = r\psi_{\mathrm{dipole},\ell}(r)$. The polynomial form of $p(r)$ ensures that this is a set of linear equations in the coefficients c_i, and so has a straightforward solution. We

also require that the pseudo-wavefunction has zero curvature at the origin,

$$c_2^2 = -c_4(2\ell + 4),$$

and that the norm of the pseudo-wavefunction within the cutoff radius is the same as that from the exact potential, to conserve the physical particle weight

$$2c_0 + \ln\left(\int_0^{r_c} r^{2\ell+1} \exp\left(2p(r) - 2c_0\right) \mathrm{d}r\right) = \ln\left(\int_0^{r_c} |\psi_{\mathrm{dipole},\ell}(r,\phi)|^2 r \mathrm{d}r\right).$$

This fully specifies $p(r)$ and hence, via Equation (A.2), $V_{\mathrm{T-M}}$. We solve these equations simultaneously for the c_i, always taking the branch of the quadratic equation that gives the smaller value for c_0, which in turn gives a larger reduction in variance for simulations using the pseudopotential.

Appendix B

Choosing a calibration energy

The Troullier–Martins formalism for deriving pseudopotentials is designed to give exact scattering properties at the calibration energy. The norm-conservation condition may also be considered as requiring that the derivative of the phase shift with respect to energy evaluated at the calibration energy $\partial\Delta\delta/\partial E|_{E_c} = 0$ [61]. This means that to leading order the error in the scattering phase shift when using a Troullier–Martins pseudopotential $\Delta\delta \propto (E - E_c)^2$. Expressing this in terms of the relative momentum $\mathbf{k}_1 - \mathbf{k}_2$ of the two scattering particles with momenta $\mathbf{k}_1$, $\mathbf{k}_2$, the scattering phase shift error $\Delta\delta(|(\mathbf{k}_1 - \mathbf{k}_2)/2|^2) \propto (|(\mathbf{k}_1 - \mathbf{k}_2)/2|^2 - k_c^2)^2$ where $k_c = \sqrt{E_c}$ is the calibration wave vector. To find the optimum calibration wave vector we average this error over the Fermi sea for particles 1 and 2 and then minimise with respect to k_c. The average

$$\langle\Delta\delta\rangle = \frac{\int \Delta\delta\left(\left|\frac{\mathbf{k}_1 - \mathbf{k}_2}{2}\right|^2\right) n(k_1)n(k_2)\,\mathrm{d}\mathbf{k}_1\,\mathrm{d}\mathbf{k}_2}{\int n(k_1)n(k_2)\,\mathrm{d}\mathbf{k}_1\,\mathrm{d}\mathbf{k}_2}, \tag{B.1}$$

where $n(k)$ is the Fermi-Dirac distribution, can be re-written in terms of centre-of-momentum and relative coordinates $\mathbf{x} = (\mathbf{k}_1 - \mathbf{k}_2)/2k_F$, $\mathbf{y} = (\mathbf{k}_1 + \mathbf{k}_2)/2k_F$, which transforms Equation (B.1) into [75]

$$\langle\Delta\delta\rangle \propto \int_0^{2\pi} \int_0^1 \int_0^{y_0(x,\phi)} \Delta\delta(k_F^2 x^2)\, x\, y\,\mathrm{d}y\,\mathrm{d}x\,\mathrm{d}\phi\,,$$

137

where ϕ is the angle between $\mathbf{x}$ and $\mathbf{y}$ and the function $y_0(x, \phi) = -x|\cos\phi| + \sqrt{1 - x^2\sin^2\phi}$. This then simplifies to

$$\langle\Delta\delta\rangle \propto \int_0^1 x\Delta\delta(k_{\mathrm{F}}^2 x^2)\left(\pi - 2\left(x\sqrt{1 - x^2} + \arcsin x\right)\right)\,\mathrm{d}x\,,$$

and substituting the form of $\Delta\delta \propto (k_{\mathrm{F}}^2 x^2 - k_{\mathrm{c}}^2)^2$ from above the optimum value of k_{c} is found to be $k_{\mathrm{F}}/2$, and hence the optimum calibration energy $E_{\mathrm{c}} = E_{\mathrm{F}}/4$.

Appendix C

Symmetry-related vectors for the ν term

Here we enumerate the $\{\mathbf{A}\}$ and $\{\mathbf{B}\}$ vectors for use in the ν term for some common simulation-cell geometries.

C.1   Cubic cell

For a cubic cell with lattice vectors $\mathbf{a}_1 = a[100]$, $\mathbf{a}_2 = a[010]$, $\mathbf{a}_3 = a[001]$, the symmetry-related vectors take the form

$$\{\mathbf{A}\} = \frac{1}{2\pi}\{\mathbf{a}_1, \mathbf{a}_2, \mathbf{a}_3\}$$
$$\{\mathbf{B}\} = \{\mathbf{b}_1, \mathbf{b}_2, \mathbf{b}_3\}.$$

C.2   FCC cell

For a face-centred cubic cell with lattice vectors $\mathbf{a}_1 = \frac{a}{2}[011]$, $\mathbf{a}_2 = \frac{a}{2}[101]$, $\mathbf{a}_3 = \frac{a}{2}[110]$, the symmetry-related vectors take the form

$$\{\mathbf{A}\} = \frac{1}{8\pi}\{3\mathbf{a}_1 - \mathbf{a}_2 - \mathbf{a}_3, 3\mathbf{a}_2 - \mathbf{a}_3 - \mathbf{a}_1, 3\mathbf{a}_3 - \mathbf{a}_1 - \mathbf{a}_2, \mathbf{a}_1 + \mathbf{a}_2 + \mathbf{a}_3\}$$
$$\{\mathbf{B}\} = \{\mathbf{b}_1, \mathbf{b}_2, \mathbf{b}_3, \mathbf{b}_1 + \mathbf{b}_2 + \mathbf{b}_3\}.$$

C.3   BCC cell

For a body-centred cubic cell with lattice vectors $\mathbf{a}_1 = \frac{a}{2}[\bar{1}11]$, $\mathbf{a}_2 = \frac{a}{2}[1\bar{1}1]$, $\mathbf{a}_3 = \frac{a}{2}[11\bar{1}]$, the symmetry-related vectors take the form

$$\{\mathbf{A}\} = \frac{1}{8\pi}\{2\mathbf{a}_1 + \mathbf{a}_2 + \mathbf{a}_3, 2\mathbf{a}_2 + \mathbf{a}_3 + \mathbf{a}_1, 2\mathbf{a}_3 + \mathbf{a}_1 + \mathbf{a}_2, \mathbf{a}_1 - \mathbf{a}_2, \mathbf{a}_1 - \mathbf{a}_3, \mathbf{a}_2 - \mathbf{a}_3\}$$

$$\{\mathbf{B}\} = \{\mathbf{b}_1, \mathbf{b}_2, \mathbf{b}_3, \mathbf{b}_1 - \mathbf{b}_2, \mathbf{b}_1 - \mathbf{b}_3, \mathbf{b}_2 - \mathbf{b}_3\}.$$

C.4   Hexagonal cell

For a hexagonal cell with lattice vectors $\mathbf{a}_1 = a[100]$, $\mathbf{a}_2 = a[\frac{1}{2}\frac{\sqrt{3}}{2}0]$, $\mathbf{a}_3 = c[001]$, the symmetry-related vectors take the form

$$\{\mathbf{A}\} = \frac{1}{6\pi}\{2\mathbf{a}_1 - \mathbf{a}_2, 2\mathbf{a}_2 - \mathbf{a}_1, 3\mathbf{a}_3, \mathbf{a}_1 + \mathbf{a}_2\}$$

$$\{\mathbf{B}\} = \{\mathbf{b}_1, \mathbf{b}_2, \mathbf{b}_3, \mathbf{b}_1 + \mathbf{b}_2\}.$$

Appendix D

Calculation of the J integrals

The derivation of the value of $N_\uparrow/N_\downarrow$ depends on the form of the J_x expressions, in particular $J_\uparrow$, $J_\downarrow$, and $J_{\uparrow\downarrow}$. These are special cases of the general integral

$$J(\mathbf{q}_1, \mathbf{q}_2, \mathbf{q}_3, \mathbf{q}_4) = T \sum_{\omega, \mathbf{k}} \mathcal{G}_{\mathbf{q}_1+\mathbf{k},\uparrow} \mathcal{G}_{\mathbf{q}_2-\mathbf{k},\downarrow} \mathcal{G}_{\mathbf{q}_3+\mathbf{k},\uparrow} \mathcal{G}_{\mathbf{q}_4-\mathbf{k},\downarrow},$$

which we shall calculate here. This integral has been previously calculated in three dimensions, for example in Ref. [176]. We start from Eq. (A5) in Ref. [176], which holds for general dimensionality, and which in our notation reads

$$
\begin{aligned}
J =\, &\mathcal{N} \int_0^1 \mathrm{d}x_1 \mathrm{d}x_2 \mathrm{d}y_1 \mathrm{d}y_2 \delta(x_1 + x_2 - 1) \delta(y_1 + y_2 - 1) \\
&\times \int \frac{\mathrm{d}\omega}{2\pi} \frac{\mathrm{d}\hat{\mathbf{k}}}{2\pi} \mathrm{d}\xi (\xi - \delta\mu + i\omega + 2\mathbf{l} \cdot \hat{\mathbf{k}})^{-2} \\
&\times (\xi + \delta\mu - i\omega + 2\mathbf{p} \cdot \hat{\mathbf{k}})^{-2},
\end{aligned}
\tag{D.1}
$$

where $\mathcal{N}$ is the density of states, $\mathbf{l} = x_2(\mathbf{q}_1 - \mathbf{q}_2)$, $\mathbf{p} = y_1\mathbf{q}_1 + y_2(\mathbf{q}_1 - \mathbf{q}_2 + \mathbf{q}_3)$, the x_i and y_i are Feynman parameters, ω is the Matsubara frequency, $\hat{\mathbf{k}}$ is the angular component of momentum, ξ a measure of the kinetic energy, and $\delta\mu$ is the chemical potential imbalance.

We first carry out the ξ integral. As Eq. (D.1) is convergent we extend the limits

on the integral to $\pm\infty$, and use the method of residues to obtain

$$
\begin{aligned}
J =& \mathcal{N} \int_0^1 \mathrm{d}x_1 \mathrm{d}x_2 \mathrm{d}y_1 \mathrm{d}y_2 \delta(x_1 + x_2 - 1)\delta(y_1 + y_2 - 1) \\
& \times \int \frac{\mathrm{d}\omega}{2\pi} \frac{\mathrm{d}\hat{\mathbf{k}}}{2\pi} \mathrm{sgn}(\omega) \frac{2\pi i}{4\left((\mathbf{p} - \mathbf{l}) \cdot \hat{\mathbf{k}} + \delta\mu - i\omega\right)^3}.
\end{aligned}
\tag{D.2}
$$

We then use the method of residues again to carry out the $\hat{\mathbf{k}}$ integral, using $(\mathbf{p}-\mathbf{l})\cdot\hat{\mathbf{k}} = |\mathbf{p} - \mathbf{l}|k_\mathrm{F}\cos\theta$. This leaves us with

$$
\begin{aligned}
J =& \mathcal{N} \int_0^1 \mathrm{d}x_1 \mathrm{d}x_2 \mathrm{d}y_1 \mathrm{d}y_2 \delta(x_1 + x_2 - 1)\delta(y_1 + y_2 - 1) \\
& \times \int \frac{\mathrm{d}\omega}{2\pi} \mathrm{sgn}(\omega) \frac{\pi}{4} \frac{|\mathbf{p} - \mathbf{l}|^2 k_\mathrm{F}^2 + 2(\delta\mu - i\omega)^2}{\left(|\mathbf{p} - \mathbf{l}|^2 k_\mathrm{F}^2 - (\delta\mu - i\omega)^2\right)^{5/2}}.
\end{aligned}
\tag{D.3}
$$

As the integrand in Eq. (D.3) depends only on $i\omega$, we use

$$
\int_{-\infty}^{\infty} \mathrm{d}\omega\, \mathrm{sgn}(\omega)\Big(\cdots\Big) = 2\mathrm{Re} \int_0^\infty \mathrm{d}\omega \Big(\cdots\Big)
$$

to rewrite Eq. (D.3) as

$$
\begin{aligned}
J =& \frac{\mathcal{N}}{4} \int_0^1 \mathrm{d}x_1 \mathrm{d}x_2 \mathrm{d}y_1 \mathrm{d}y_2 \delta(x_1 + x_2 - 1)\delta(y_1 + y_2 - 1) \\
& \times \mathrm{Re} \int_0^\infty \mathrm{d}\omega \frac{|\mathbf{p} - \mathbf{l}|^2 k_\mathrm{F}^2 + 2(\delta\mu - i\omega)^2}{\left(|\mathbf{p} - \mathbf{l}|^2 k_\mathrm{F}^2 - (\delta\mu - i\omega)^2\right)^{5/2}}.
\end{aligned}
\tag{D.4}
$$

The remaining integral may be carried out using conventional methods to obtain

$$
J = \frac{\mathcal{N}}{4\delta\mu^2} \mathrm{Re} \int_0^1 \mathrm{d}x_1 \mathrm{d}x_2 \mathrm{d}y_1 \mathrm{d}y_2 \frac{\delta(x_1 + x_2 - 1)\delta(y_1 + y_2 - 1)}{\left(1 - \left(\frac{|\mathbf{p}-\mathbf{l}|k_\mathrm{F}}{\delta\mu}\right)^2\right)^{3/2}}.
$$

To recover the result in the main text we then substitute in $\mathbf{l}$ and $\mathbf{p}$, and carry out

the x_1 and y_1 integrals. This leaves us with

$$J = \frac{\mathcal{N}}{4\delta\mu^2}\mathrm{Re} \int_0^1 \frac{\mathrm{d}x\mathrm{d}y}{\left(1 - \left[\frac{|\mathbf{q}_1(x-1)+\mathbf{q}_2(y-x)-\mathbf{q}_3y|k_\mathrm{F}}{\delta\mu}\right]^2\right)^{3/2}}.$$

Bibliography

[1] J. Brodholt and L. Vočadlo, MRS Bulletin **31**(9), 675 (2006).

[2] M.E. Fisher, Rep. Prog. Phys. **30**, 615 (1967).

[3] J. Werner, A. Griesmaier, S. Hensler, J. Stuhler, T. Pfau, A. Simoni, and E. Tiesinga, Phys. Rev. Lett. **94**, 183201 (2005).

[4] T. Lahaye, T. Koch, B. Fröhlich, M. Fattori, J. Metz, A. Griesmaier, S. Giovanazzi, and T. Pfau, Nature **448**, 672 (2007).

[5] G. Bismut, B. Laburthe-Tolra, E. Maréchal, P. Pedri, O. Gorceix, and L. Vernac, Phys. Rev. Lett. **109**, 155302 (2012).

[6] K.-K. Ni, S. Ospelkaus, M.H.G. de Miranda, A. Pe'er, B. Neyenhuis, J.J. Zirbel, S. Kotochigova, P.S. Julienne, D.S. Jin, and J. Ye, Science **322**, 231 (2008).

[7] K.-K. Ni, S. Ospelkaus, D. Wang, G. Quéméner, B. Neyenhuis, M.H.G. de Miranda, J.L. Bohn, J. Ye, and D.S. Jin, Nature **464**, 1324 (2010).

[8] D. Wang, B. Neyenhuis, M.H.G. de Miranda, K.-K. Ni, S. Ospelkaus, D.S. Jin, and J. Ye, Phys. Rev. A **81**, 061404 (2010).

[9] C.-H. Wu, J.W. Park, P. Ahmadi, S. Will, and M.W. Zwierlein, Phys. Rev. Lett. **109**, 085301 (2012).

[10] B. Neyenhuis, B. Yan, S.A. Moses, J.P. Covey, A. Chotia, A. Petrov, S. Kotochigova, J. Ye, and D.S. Jin, Phys. Rev. Lett. **109**, 230403 (2012).

[11] T. Takekoshi, L. Reichsöllner, A. Schindewolf, J.M. Hutson, C.R. Le Sueur, O. Dulieu, F. Ferlaino, R. Grimm, and H.C. Nägerl, Phys. Rev. Lett. **113**, 205301 (2014).

[12] J.W. Park, S.A. Will, and M.W. Zwierlein, Phys. Rev. Lett. **114**, 205302 (2015).

[13] M.H.G. de Miranda, A. Chotia, B. Neyenhuis, D. Wang, G. Quéméner, S. Ospelkaus, J.L. Bohn, J. Ye, D.S. Jin, Nature Physics **7**, 502 (2011).

[14] D. DeMille, Phys. Rev. Lett. **88**, 067901 (2002).

[15] A. André, D. DeMille, J.M. Doyle, M.D. Lukin, S.E. Maxwell, P. Rabl, R.J. Schoelkopf, and P. Zoller, Nature Physics **2**, 636 (2006).

[16] S.F. Yelin, K. Kirby, and R. Côté, Phys. Rev. A **74**, 050301(R) (2006).

[17] R.V. Krems, Phys. Chem. Chem. Phys. **10**, 4079 (2008).

[18] R. Feynman, Int. J. Theor. Phys. **21**, 467 (1982).

[19] C. Chin, R. Grimm, P. Julienne, and E. Tiesinga, Rev. Mod. Phys. **82**, 1225 (2010).

[20] L. Xing, Phys. Rev. B **42**, 8426 (1990).

[21] G.E. Astrakharchik, J. Boronat, J. Casulleras, and S. Giorgini, Phys. Rev. Lett. **93**, 200404 (2004).

[22] M. Casula, D.M. Ceperley, and E.J. Mueller, Phys. Rev. A **78**, 033607 (2008).

[23] S. Nascimbène, N. Navon, K.J. Jiang, F. Chevy, and C. Salomon, Nature **463**, 1057 (2010).

[24] X. Li, J. Kolorenč, and L. Mitas, Phys. Rev. A **84**, 023615 (2011).

[25] S.Q. Zhou, D.M. Ceperley, and S. Zhang, Phys. Rev. A **84**, 013625 (2011).

[26] G. Bertaina and S. Giorgini, Phys. Rev. Lett. **106**, 110403 (2011).

[27] G. Bertaina, Eur. Phys. J. Spec. Top. **217**, 153 (2013).

[28] G. Bertaina, E. Fratini, S. Giorgini, and P. Pieri, Phys. Rev. Lett. **110**, 115303 (2013).

[29] W. Zhang and W. Yi, Nature Communications **4**, 2711 (2013).

[30] S.-T. Lo, S.-W. Lin, Y.-T. Wang, S.-D. Lin, and C.-T. Liang, Sci. Rep. **4**, 5438 (2014).

[31] T.W. Hänsch and A.L. Schawlow, Opt. Commun. **13**, 68 (1975).

[32] B. DeMarco and D.S. Jin, Science **285**, 1703 (1999).

[33] I. Bloch, M. Greiner, O. Mandel, T.W. Hänsch, and T. Esslinger, Phys. Rev. A **64**, 021402 (2001).

[34] I. Bloch, J. Dalibard, and W. Zwerger, Rev. Mod. Phys. **80**, 885 (2008).

[35] F. Gerbier, A. Widera, S. Föllig, O. Mandel, T. Gericke, and I. Bloch, Phys. Rev. A **72**, 053606 (2005).

[36] A. Shashi, F. Grusdt, D.A. Abanin, and E. Demier, Phys. Rev. A **89**, 053617 (2014).

[37] W.M.C. Foulkes, L. Mitas, R.J. Needs, and G. Rajagopal, Rev. Mod. Phys. **73**, 33 (2001).

[38] N. Metropolis, A.W. Rosenbluth, M.N. Rosenbluth, A.H. Teller, and E. Teller, J. Chem. Phys. **21**, 1087 (1953).

[39] R.J. Jastrow, Phys. Rev. B **98**, 1479 (1955).

[40] P.J. Reynolds, D.M. Ceperley, B.J. Alder, and W.A.J. Lester, J. Chem. Phys. **77**, 5593 (1982).

[41] R.J. Needs, M.D. Towler, N.D. Drummond, and P. López Ríos, J. Phys. Condens. Matter **22**, 023201 (2009).

[42] J. Bardeen, L.N. Cooper, and J.R. Schrieffer, Phys. Rev. **106**, 162 (1957).

[43] J. Bardeen, L.N. Cooper, and J.R. Schrieffer, Phys. Rev. **108**, 1175 (1957).

[44] R.L. Stratonovich, Sov. Phys. Dokl. **2**, 416 (1958).

[45] J. Hubbard, Phys. Rev. Lett.**3**, 77 (1959).

[46] K. Aikawa, A. Frisch, M. Mark, S. Baier, R. Grimm, J.L. Bohn, D.S. Jin, G.M. Bruun, and F. Ferlaino, Phys. Rev. Lett. **113**, 263201 (2014).

[47] F. Cinti, P. Jain, M. Boninsegni, A. Micheli, P. Zoller, and G. Pupillo, Phys. Rev. Lett. **105**, 135301 (2010).

[48] M.M. Parish and F.M. Marchetti, Phys. Rev. Lett. **108**, 145304 (2012).

[49] G.E. Astrakharchik, J. Boronat, J. Casulleras, I.L. Kurbakov, and Yu.E. Lozovik, Phys. Rev. A **75**, 063630 (2007).

[50] F. Mazzanti, R.E. Zillich, G.E. Astrakharchik, and J. Boronat, Phys. Rev. Lett. **102**, 110405 (2009).

[51] A. Macia, F. Mazzanti, J. Boronat, and R.E. Zillich, Phys. Rev. A **84**, 033625 (2011).

[52] A. Macia, D. Hufnagl, F. Mazzanti, J. Boronat, and R.E. Zillich, Phys. Rev. Lett. **109**, 235307 (2012).

[53] A. Macia, G.E. Astrakharchik, F. Mazzanti, S. Giorgini, and J. Boronat, Phys. Rev. A **90**, 043623 (2014).

[54] A. Macia, J. Boronat, and F. Mazzanti, Phys. Rev. A **90**, 061601(R) (2014).

[55] N. Matveeva and S. Giorgini, Phys. Rev. Lett. **111**, 220405 (2013).

[56] N. Matveeva and S. Giorgini, Phys. Rev. A **90**, 053620 (2014).

[57] K.R.A. Hazzard, B. Gadway, M. Foss-Feig, B. Yan, S.A. Moses, J.P. Covey, N.Y. Yao, M.D. Lukin, J. Ye, D.S. Jin, and A.M. Rey, Phys. Rev. Lett. **113**, 195302 (2014).

[58] Y. Yamaguchi, T. Sogo, T. Ito, and T. Miyakawa, Phys. Rev. A **82**, 013643 (2010).

[59] K. Sun, C. Wu, and S. Das Sarma, Phys. Rev. B **82**, 075105 (2010).

[60] N. Matveeva and S. Giorgini, Phys. Rev. Lett. **109**, 200401 (2012).

[61] P.O. Bugnion, P. López Ríos, R.J. Needs, and G.J. Conduit, Phys. Rev. A **90**, 033626 (2014).

[62] J.H. Lloyd-Williams, R.J. Needs and G.J. Conduit, Phys. Rev. B **92**, 075106 (2015).

[63] C.D. Sherrill and H.F. Schaefer III, Adv. Quant. Chem. bf 34, 143 (1999).

[64] R.J. Bartlett and M. Musiał, Rev. Mod. Phys. **79**, 291 (2007).

[65] R.J. Needs, M.D. Towler, N.D. Drummond, and P. López Ríos, J. Phys.:Condens. Matter **22**, 023201 (2010).

[66] T. Kato, Commun. Pure and Appl. Math. **10** (2), 151 (1957).

[67] R.T. Pack and W.B. Brown, J. Chem. Phys. **45**, 556 (1966).

[68] N. Troullier and J.L. Martins, Phys. Rev. B **43**, 1993 (1991).

[69] J.R. Trail and R.J. Needs, J. Chem. Phys. **122**, 174109 (2005).

[70] J.R. Trail and R.J. Needs, J. Chem. Phys. **122**, 014112 (2005).

[71] V. Heine, Solid State Physics **24**, 1 (1970).

[72] D.R. Hamann, M. Schlüter, and C. Chiang, Phys. Rev. Lett. **43**, 1494 (1979).

[73] A. Zunger and M.L. Cohen, Phys. Rev. B **20**, 4082 (1979).

[74] G.B. Bachelet, D.R. Hamann, and M. Schlüter, Phys. Rev. B **26**, 4199 (1982).

[75] Z.K. Lu and G.V. Shlyapnikov, Phys. Rev. A **85**, 023614 (2012).

[76] S. Murmann, A. Bergschneider, V.M. Klinkhamer, G. Zürn, T. Lompe, S. Jochim, Phys. Rev. Lett. **114**, 080402 (2015).

[77] S.A. Moses, J.P. Covey, M.T. Miecnikowski, B. Yan, B. Gadway, J. Ye, and D.S. Jin, Science **350**, 659 (2015).

[78] P.O. Bugnion and G.J. Conduit, Phys. Rev. A **87**, 060502(R) (2013).

[79] G.J. Conduit, A.G. Green, and B.D. Simons, Phys. Rev. Lett. **103**, 207201 (2009).

[80] P. López Ríos, P. Seth, N.D. Drummond, and R.J. Needs, Phys. Rev. E **86**, 036703 (2012).

[81] S. Pilati, G. Bertaina, S. Giorgini, and M. Troyer, Phys. Rev. Lett. **105**, 030405 (2010).

[82] N.D. Drummond, N.R. Cooper, R.J. Needs, and G.V. Shlyapnikov, Phys. Rev. B **83**, 195429 (2011).

[83] R.M. Lee, G.J. Conduit, N. Nemec, P. López Ríos, and N.D. Drummond, Phys. Rev. E **83**, 066706 (2011).

[84] S.M. Rothstein and J. Vrbik, Journal of Computational Physics, **74**, 127 (1988).

[85] J.R. Trail, Phys. Rev. E **77**, 016703 (2008).

[86] M. Mella, G. Morosi, and D. Bressanini, Phys. Rev. E **61**, 2050 (2000).

[87] A. Sarsa, J. Boronat, and J. Casulleras, J. Chem. Phys. **116**, 5956 (2002).

[88] S. Chiesa, M. Mella, G. Morosi, and D. Bressanini, J. Chem. Phys. **119**, 5601 (2003).

[89] C.K. Chan, C. Wu, W.C. Lee, and S. Das Sarma, Phys. Rev. A **81**, 023602 (2010).

[90] G.M. Bruun and E. Taylor, Phys. Rev. Lett. **101**, 245301 (2008).

[91] N.R. Cooper and G.V. Shlyapnikov, Phys. Rev. Lett. **103**, 155302 (2009).

[92] J. Levinsen, N.R. Cooper, and G.V. Shlyapnikov, Phys. Rev. A **84**, 013603 (2011).

[93] T.W. Whitehead and G.J. Conduit, Cambridge University DSpace repository, `https://www.repository.cam.ac.uk/handle/1810/253550`.

[94] Y.J. Lin, R.L. Compton, K. Jiménez-García1, J.V. Porto, and I.B. Spielman, Nature **462**, 628 (2009).

[95] P.A. Lee, N. Nagaosa, and X.G. Wen, Reviews of Modern Physics **78**, 17 (2006).

[96] S. Sachdev, Nature Physics **4**, 173 (2008).

[97] M.Z. Hasan and C.L. Kane, Reviews of Modern Physics **82**, 3045 (2010).

[98] G.J. Conduit, Phys. Rev. A **82**, 043604 (2010).

[99] V. Ngampruetikorn, J. Levinsen, and M.M. Parish, Phys. Rev. Lett. **111**, 265301 (2013).

[100] K. Martiyanov, V. Makhalov, and A. Turlapov, Phys. Rev. Lett. **105**, 030404 (2010).

[101] A.T. Sommer, L.W. Cheuk, M.J.H. Ku, W.S. Bakr, and M.W. Zwierlein, Phys. Rev. Lett. **108**, 045302 (2012).

[102] K. Günter, T. Stöferle, H. Moritz, M. Köhl, and T. Esslinger, Phys. Rev. Lett. **95**, 230401 (2005).

[103] H. Shi, S. Chiesa, and S. Zhang, Phys. Rev. A **92**, 033603 (2015).

[104] J.A. Bert, B.Kalisky, C. Bell, M. Kim, Y. Hikita, H.Y. Hwang, and K.A. Moler, Nature Physics **7**, 767 (2011).

[105] A. Görlitz, J.M. Vogels, A.E. Leanhardt, C. Raman, T.L. Gustavson, J.R. Abo-Shaeer, A.P. Chikkatur, S. Gupta, S. Inouye, T. Rosenband, and W. Ketterle, Phys. Rev. Lett. **87**, 130402 (2001).

[106] K. Fenech, P. Dyke, T. Peppler, M.G. Lingham, S. Hoinka, H. Hu, and C.J. Vale, Phys. Rev. Lett. **116**, 045302 (2016).

[107] I. Boettcher, L. Bayha, D. Kedar, P.A. Murthy, M. Neidig, M.G. Ries, A.N. Wenz, G. Zürn, S. Jochim, and T. Enss, Phys. Rev. Lett. **116**, 045303 (2016).

[108] R.A. Hart, P.D. Duarte, T.-L. Yang, X. Liu, T. Paiva, E. Khatami, R.T. Scalettar, N. Trivedi, D.A. Huse, and R.G. Hulet, Nature **519**, 211 (2015).

[109] M.H. Anderson, J.R. Ensher, M.R. Matthews, C.E. Wieman, and E.A. Cornell, Science **269**, 198 (1995).

[110] C.A. Regal, M. Greiner, and D.S. Jin, Phys. Rev. Lett **92**, 040403 (2004).

[111] M.W. Zwierlein, C.A. Stan, C.H. Schunck, S.M.F. Raupach, A.J. Kerman, and W. Ketterle, Phys. Rev. Lett **92**, 120403 (2004).

[112] T.M. Whitehead and G.J. Conduit, Phys. Rev. A **93**, 022706 (2016).

[113] X.J. Liu, H. Hu, and P.D. Drummond, Phys. Rev. B **82**, 054524 (2010).

[114] A. Farrell and P.B. van Zyl, Can. J. Phys. **88**, 817 (2010).

[115] N. Troullier and J.L. Martins, Phys. Rev. B **43**, 1993 (1991).

[116] We provide a Mathematica notebook to generate the hard and soft disk potentials, square well potential, Troullier–Martins pseudopotentials for both attractive and bound states, and UTP at `www.repository.cam.ac.uk/handle/1810/253582`.

[117] G.J. Conduit, Phys. Rev. B **87**, 184414 (2013).

[118] G. Zürn, F. Serwane, T. Lompe, A.N. Wenz, M.G. Ries, J.E. Bohn, and S. Jochim, Phys. Rev. Lett. **108**, 075303 (2012).

[119] T. Busch, B.G. Englert, K. Rzazewski and M. Wilkens, Foundations of Physics **28**, 549 (1998).

[120] M.G. Ries, A.N. Wenz, G. Zürn, L. Bayha, I. Boettcher, D. Kedar, P.A. Murthy, M. Neidig, T. Lompe, and S. Jochim, Phys. Rev. Lett **114**, 230401 (2015).

[121] B. Fröhlich, M. Feld, E. Vogt, M. Koschorreck, W. Zwerger, and M. Köhl, Phys. Rev. Lett. **106**, 105301 (2011).

[122] W. Ong, C. Cheng, I. Arakelyan, and J.E. Thomas, Phys. Rev. Lett. **114**, 110403 (2015).

[123] J.R. Engelbrecht and M. Randeria, Phys. Rev. B **45**, 12419 (1992).

[124] J.R. Engelbrecht, M. Randeria, and L. Zhang, Phys. Rev. B **45**, 10135 (1992).

[125] L. He, Phys. Rev. A **90**, 053633 (2014).

[126] D.M. Ceperley, and B.J. Alder, Phys. Rev. Lett. **45**, 566 (1980).

[127] C. Umrigar, The Journal of Chemical Physics **99**, 2865 (1993).

[128] A. Ma, N.D. Drummond, M.D. Towler, and R.J. Needs, Phys. Rev. E **71**, 066704 (2005).

[129] M.M. Forbes, E. Gubankova, W.V. Liu, and F. Wilczek, Phys. Rev. Lett **94**, 017001 (2005).

[130] W.V. Liu and F. Wilczek, Phys. Rev. Lett. **90**, 047002 (2003).

[131] V.A. Babenko and N.M. Petrov, Physics of Atomic Nuclei **76**, 684 (2013).

[132] T.M. Whitehead, L.M. Schonenberg, N. Kongsuwan, R.J. Needs, and G.J. Conduit, Cambridge University DSpace Repository, `www.repository.cam.ac.uk/handle/1810/254305`.

[133] A.J. Williamson, S.D. Kenny, G. Rajagopal, A.J. James, R.J. Needs, L.M. Fraser, W.M.C. Foulkes, and P. Maccallum, Phys. Rev. B **53**, 9640 (1996).

[134] N.D. Drummond, M.D. Towler, and R.J. Needs, Phys. Rev. B **70**, 235119 (2004).

[135] G. Ortiz and P. Ballone, Phys. Rev. B **50**, 1391 (1994).

[136] W.L. McMillan, Phys. Rev. **138**, A442 (1965).

[137] D.M. Ceperley, Phys. Rev. B **18**, 3126 (1978).

[138] A.D. Güçlü, Gun Sang Jeon, C.J. Umrigar, and J.K. Jain, Phys. Rev. B, **72**, 205327 (2005).

[139] G.E. Astrakharchik, J. Boronat, I.L. Kurbakov, and Yu.E. Lozovik, Phys. Rev. Lett. **98**, 060405 (2007).

[140] J.B. Anderson, J. Chem. Phys. **65**, 4121 (1976).

[141] C.J. Umrigar, K.G. Wilson, and J.W. Wilkins, Phys. Rev. Lett. **60**, 1719 (1988).

[142] Y.S. Al-Hamdani, D. Alfè, O.A. von Lilienfeld, and A. Michaelides, J. Chem. Phys. **141** 18C530 (2014).

[143] J. Chen, X. Ren, X.-Z. Li, D. Alfè, and E. Wang, J. Chem. Phys. **141**, 024501 (2014).

[144] M.J. Gillan, D. Alfè, and F.R. Manby, J. Chem. Phys. **143**, 102812 (2015).

[145] N.D. Drummond and R.J. Needs, Phys. Rev. B **87**, 045131 (2013).

[146] S. Chiesa, D.M. Ceperley, R.M. Martin, and M. Holzmann, Phys. Rev. Lett. **97**, 076404 (2006).

[147] G.G. Spink, R.J. Needs, and N.D. Drummond, Phys. Rev. B **88**, 085121 (2013).

[148] C.W. von Keyserlingk and G.J. Conduit, Phys. Rev. B **87**, 184424 (2013).

[149] R. Maezono, N.D. Drummond, A. Ma, and R.J. Needs, Phys. Rev. B **82**, 184108 (2010).

[150] E. Mostaani, N.D. Drummond, and V.I. Fal'ko, Phys. Rev. Lett. **115**, 115501 (2015).

[151] N.D. Drummond and R.J. Needs, Phys. Rev. B **72**, 085124 (2005).

[152] F.H. Zong, C. Lin, and D.M. Ceperley, Phys. Rev. E **66**, 036703 (2002).

[153] N.D. Drummond, Z. Radnai, J.R. Trail, M.D. Towler, and R.J. Needs, Phys. Rev. B **69**, 085116 (2004).

[154] P.R.C. Kent, R.J. Needs, and G. Rajagopal, Phys. Rev. B **59**, 12344 (1999).

[155] C.J. Umrigar, J. Toulouse, C. Filippi, S. Sorella, and R.G. Hennig, Phys. Rev. Lett. **98**, 110201 (2007).

[156] N.D. Drummond, R.J. Needs, A. Sorouri, and W.M.C. Foulkes, Phys. Rev. B **78**, 125106 (2008).

[157] W.E. Pickett, Computer Physics Reports, **9**, 115 (1989).

[158] P. Hohenberg and W. Kohn, Phys. Rev. **136**, B864 (1964).

[159] W. Kohn and L.J. Sham, Phys. Rev. **140**, A1133 (1965).

[160] M.C. Payne, M.P. Teter, D.C. Allan, T.A. Arias, and J.D. Joannopoulos, Rev. Mod. Phys. **64**, 1045 (1992).

[161] S.J. Clark, M.D. Segall, C.J. Pickard, P.J. Hasnip, M.J. Probert, K. Refson, and M.C. Payne, Z. Kristall **220**, 567 (2005).

[162] E. Hernández, M.J. Gillan, and C.M. Goringe, Phys. Rev. B **55**, 13485 (1997).

[163] D. Alfè and M.J. Gillan, Phys. Rev. B **70**, 161101(R) (2004).

[164] C.-J. Huang, C.J. Umrigar, M.P. Nightingale, J. Chem. Phys. **107**, 3007 (1997).

[165] T.M. Whitehead, L.M. Schonenberg, N. Kongsuwan, R.J. Needs, and G.J. Conduit, Phys. Rev. A **93**, 042702 (2016).

[166] B. Ganchev, N.D. Drummond, I. Aleiner, and V. Fal'ko, Phys. Rev. Lett. **114**, 107401 (2015).

[167] J.P. Bouchaud, A. Georges, and C. Lhuillier, J. Physique **49**, 553 (1988).

[168] S. Baroni, S. de Gironcoli, A. Dal Corso, and P. Giannozzi, Rev. Mod. Phys. **73**, 515 (2001).

[169] A.D. Mackerell, J. Comput. Chem. **25**, 1584 (2004).

[170] Available from `https://vallico.net/casinoqmc/`.

[171] T.M. Whitehead, M.H. Michael, and G.J. Conduit, Cambridge University DSpace repository, `http://dx.doi.org/10.17863/CAM.694`.

[172] L.N. Cooper, Phys. Rev. **104**, 1189 (1956).

[173] P. Fulde and R.A. Ferrell, Phys. Rev. **135**, A550 (1964).

[174] A.I. Larkin, Y.N. Ovchinnikov, Sov. Phys. JETP **20**, 762 (1965).

[175] R. Casalbuoni and G. Nardulli, Rev. Mod. Phys. **76**, 263 (2004).

[176] J.A. Bowers and K. Rajagopal, Phys. Rev. D **66**, 065002 (2002).

[177] A. Bianchi, R. Movshovich, C. Capan, P.G. Pagliuso, and J.L. Sarrao, Phys. Rev. Lett. **91**, 187004 (2003).

[178] H. Mayaffre, S. Krämer, M. Horvatić, C. Berthier, K. Miyagawa, K. Kanoda, and V.F. Mitrović, Nature Physics **10**, 928 (2014).

[179] R. Prozorov, M.D. Vannette, S.A. Law, S.L. Bud'ko, and P.C. Canfield, Phys. Rev. B **77**, 100503(R) (2008).

[180] P.C. Canfield, S.L. Bud'ko, and B.K. Cho, Physica C **262**, 249 (1996).

[181] M.H. Hamidian, S.D. Edkins, S.H. Joo, A. Kostin, H. Eisaki, S. Uchida, M.J. Lawler, E.-A. Kim, A.P. Mackenzie, K. Fujita, J. Lee, and J.C.S. Davis, Nature **532**, 343 (2016).

[182] Y. Liao, A.S.C. Rittner, T. Paprotta, W. Li, G.B. Partridge, R.G. Hulet, S.K. Baur, and E.J. Mueller, Nature **467**, 567 (2010).

[183] J.A. Kok and W.H. Keesom, Physica **4**, 835 (1937).

[184] C.A. Reynolds, B. Serin, and L.B. Nesbitt, Phys. Rev. **84**, 691 (1951).

[185] M. Horowitz, A.A. Silvidi, S.F. Malaker, and J.G. Daunt, Phys. Rev. **88**, 1182 (1952).

[186] P. Aebi, J. Osterwalder, P. Schwaller, L. Schlapbach, M. Shimoda, T. Mochiku, and K. Kadowaki, Phys. Rev. Lett. **72**, 2757 (1994).

[187] H. Shishido, T. Ueda, S. Hashimoto, T. Kubo, R. Settai, H. Harima, and Y. Ōnuki, J. Phys.: Condens. Matter **15**, L499 (2003).

[188] R. Lortz, Y. Wang, A. Demuer, P.H.M. Böttger, B. Bergk, G. Zwicknagl, Y. Nakazawa, and J. Wosnitza, Phys. Rev. Lett. **99**, 187002 (2007).

[189] W.V. Pogosov, M. Combescot, and M. Crouzeix, Phys. Rev. B **81**, 174514 (2010).

[190] W.V. Pogosov and M. Combescot, Physica C **471**, 566 (2011).

[191] J.D. Fan and Y.M. Malozovsky, J. Supercond. Nov. Magn. **23**, 655 (2010).

[192] K. Yang, Phys. Rev. B **63**, 140511(R), (2001).

[193] H. Hu, X.-J. Liu, and P.D. Drummond, Phys. Rev. Lett. **98**, 070403 (2007).

[194] M.M. Parish, S.K. Baur, E.J. Mueller, and D.A. Huse, Phys. Rev. Lett. **99**, 250403 (2007).

[195] A.E. Feiguin and F. Heidrich-Meisner, Phys. Rev. B **76**, 220508(R) (2007).

[196] G.G. Batrouni, M.H. Huntley, V.G. Rousseau, and R.T. Scalettar, Phys. Rev. Lett. **100**, 116405 (2008).

[197] E. Gubankova, W.V. Liu, and F. Wilczek, Phys. Rev. Lett. **91**, 032001 (2003).

[198] M.M. Parish, F.M. Marchetti, A. Lamacraft, and B.D. Simons, Phys. Rev. Lett. **98**, 160402 (2007).

[199] P. Massignan, M. Zaccanti, and G.M. Bruun, Rep. Prog. Phys. **77**, 034401 (2014).

[200] P. Nozières and S. Schmitt-Rink, J. Low Temp. Phys. **59**, 195 (1985).

[201] P.O. Bugnion, J.A. Lofthouse, and G.J. Conduit, Phys. Rev. Lett. **111**, 045301 (2013).

[202] F. Serwane, G. Zürn, T. Lompe, T.B. Ottenstein, A.N. Wenz, and S. Jochim, Science **332**, 336 (2011).

[203] Yu.E. Lozovik and V.I. Yudson, JETP Lett. **22**, 274 (1975).

[204] A. Perali, D. Neilson, and A.R. Hamilton, Phys. Rev. Lett. **110**, 146803 (2013).

[205] M.W. Zwierlein, A. Schirotzek, C.H. Schunck, and W. Ketterle, Science **311**, 492 (2006).

[206] G.B. Partridge, W. Li, R.I. Kamar, Y. Liao, and R.G. Hulet, Science **311**, 503 (2006).

[207] B. Mukherjee, Z. Yan, P.B. Patel, Z. Hadzibabic, T. Yefsah, J. Struck, and M.W. Zwierlein, Phys. Rev. Lett. **118**, 123401 (2017).

[208] A.F. Andreev, Sov. Phys. JETP **19**, 1228 (1964).

[209] B.D. Josephson, Phys. Lett. **1**, 251 (1962).

[210] R.C. Jaklevic, J. Lambe, A.H. Silver, and J.E. Mercereau, Phys. Rev. Lett. **12**, 159 (1964).

[211] G. Kiršanskas, M. Goldstein, K. Flensberg, L.I. Glazman, and J. Paaske, Phys. Rev. B **92**, 235422 (2015).

[212] T.M. Whitehead and G.J. Conduit, Cambridge University DSpace repository, `https://doi.org/10.17863/CAM.15832`.

[213] T.M. Whitehead and G.J. Conduit, Phys. Rev. B **97**, 014502 (2018).

[214] F. Chevy, Phys. Rev. A **74**, 063628 (2006).

[215] R. Combescot and S. Giraud, Phys. Rev. Lett. **101**, 050404 (2008).

[216] B.S. Chandrasekhar, Appl. Phys. Lett. **1**, 7 (1962).

[217] A.M. Clogston, Phys. Rev. Lett. **9**, 266 (1962).

[218] Q. Chen, Y. He, C.-C. Chien, and K. Levin, Phys. Rev. A **74**, 063603 (2006).

[219] J. Wang, Y. Che, L. Zhang, and Q. Chen, Sci. Rep. **7**, 39783 (2017).

[220] E. Altman, E. Demler, and M.D. Lukin, Phys. Rev. A **70**, 013603 (2004).

[221] L.M. Schonenberg and G.J. Conduit, Phys. Rev. a **95**, 013633 (2017).

[222] L.M. Schonenberg, P.C. Verpoort, and G.J. Conduit, Phys. Rev. A **96**, 023619 (2017).